Modeling of sheet metal fracture for shell finite elements with component level validation

by

Keunhwan Pack

B.S. Mechanical Engineering,
Korea Advanced Institute of Science and Technology, Republic of Korea (2009)
M.S. Mechanical Engineering,
Korea Advanced Institute of Science and Technology, Republic of Korea (2012)

Submitted to the Department of Mechanical Engineering
in Partial Fulfillment of the Requirements for the Degree of

Doctor of Philosophy in Mechanical Engineering

at the

MASSACHUSETTS INSTITUTE OF TECHNOLOGY

June 2017

Author: Signature redacted
Department of Mechanical Engineering
April 07, 2017

Certified by: Signature redacted
Tomasz Wierzbicki
Professor of Applied Mechanics
Thesis Supervisor

Certified by: Signature redacted
Dirk Mohr
Assistant Professor of Mechanical and Process Engineering at ETH Zurich
Thesis Supervisor

Accepted by: Signature redacted
Rohan Abeyaratne
Chairman, Committee on Graduate Students
Department of Mechanical Engineering

Modeling of sheet metal fracture for shell finite elements with component level validation

by

Keunhwan Pack

Submitted to the Department of Mechanical Engineering
on April 07, 2017, in Partial Fulfillment of the Requirements for the Degree of
Doctor of Philosophy in Mechanical Engineering

Abstract

Ductile fracture causing premature failure of parts during forming and crash has become an important factor limiting design of car bodies. The increasing usage of advanced high strength steels and other lightweight materials to meet ever-stringent standards on passenger safety and gas emissions makes related advances in experimental and computational mechanics a pressing issue. The industry has been using shell finite elements in design practice due to many practical advantages over solid elements.

A constitutive assumption of the plane stress condition in shell elements, violated after the onset of localized necking, is responsible for an inaccurate numerical prediction of mechanical response with mesh-size sensitivity. This thesis proposes a new approach to predict ductile failure with shell elements. It is based on the concept of a Domain of Shell-to-Solid Equivalence (DSSE) in conjunction with the Hosford-Coulomb (HC) fracture initiation model. The latter is a micro-mechanically motivated phenomenological model for solid elements. DSSE is the domain in which shell element solutions are valid and comparable to solid elements. Consequently, it is appropriate to apply the HC model within DSSE. On the other hand, a shell element loses its reliability when exiting DSSE, thus being removed from the rest of a finite element model. A general shape of a localization locus that demarcates DSSE for proportional membrane loading is identified through a Marciniak-Kuczynski type localization analysis. The locus is successfully fitted by a mathematical form of the HC model, and a model parameter is simply determined by the Considère criterion. DSSE is then extended towards non-proportional and combined membrane and bending loading.

The DSSE-HC model for shell elements covers three types of ductile failure observed in sheet metals: (1) in-plane shear localization, (2) biaxial fracture *not* preceded by localized necking, aka surface cracking, and (3) biaxial fracture in consequence of localized necking. Validation is made in two steps. First, the model accuracy is evaluated purely numerically, compared to solid elements. Secondly, a comprehensive experimental validation is performed at both specimen and structural levels. The former covers membrane stretching, stretch bending, pure bending, and in-plane shear. The latter is concerned with triangular cup-drawing.

Thesis Supervisor: Tomasz Wierzbicki
Title: Professor of Applied Mechanics

Thesis Supervisor: Dirk Mohr
Title: Assistant Professor of Mechanical and Process Engineering at ETH Zurich

Acknowledgments

Above all, my foremost gratitude goes to Professor Tomasz Wierzbicki and Professor Dirk Mohr who provided me with a great opportunity to embark my journey in the Impact and Crashworthiness Lab. Their astonishing academic insights with continuous guidance, support, and trust throughout four and a half years of my stay at MIT were crucial for me to achieve a small success.

In addition, I am heavily indebted to Professor Lallit Anand, Professor Tal Cohen, and Professor Raul Radovitzky, who afforded numerous constructive comments by serving on my thesis committee. Their graduate-level classes made a substantial contribution to strengthening my fundamental understanding of solid mechanics.

I also would like to acknowledge Dr. Thomas B. Stoughton at GM and Dr. Juan Hurtado at Dassault Systèmes for their keen interest and knowledgeable advice.

Every minute in the Impact and Crashworthiness Lab has been an unforgettably joyful moment thanks to all the past and current colleagues: Prof. Yuanli Bai, Prof. Yong Xia, Prof. Elham Sahraei, Prof. Emanuela Bosco, Dr. Meng Luo, Dr. Matthieu Dunand, Dr. Kirki Kofiani, Dr. Marcelo Paredes, Dr. Andy Gish, Dr. Andrea Gilioli, Dr. Borja Erice, Dr. Christian Roth, Dr. Kai Wang, Dr. Stephane Marcadet, Dr. Maysam Gorji, Dr. Xiaowei Zhang, Mr. Colin Bonatti, Mr. Rami Abi Akl, Mr. Thomas Tancogne-Dejean, Mr. Juner Zhu, Mr. Yannik Sparrer, Mr. Charles Boubert, Mr. Hailing Luo, Mr. Joseph Meier, Mr. Kyle Miller, Ms. Brandy Dixon Mr. Sagy Hakoon, Mrs. Amber Mason, and Ms. Aswini Prasad. Special thanks go to Barbara Smith for her indispensable assistance.

Also are greatly appreciated the partial financial support from the MIT Industrial Fracture Consortium and the incredibly wonderful machining by engineers at MIT Central Machine Shop.

I am also grateful to Korean Graduate Student Association at Mechanical Engineering and all my dear friends for being a true spiritual support.

Lastly, I want to express my deepest thanks and respects to my lovely family for their unconditional love and unlimited support.

Table of Contents

List of Figures

model only are shown in the first row (a, b), while the second row (c, d) shows the improved predictions obtained with the combined DSSE-HC model.

Figure 6-12. Contour plots of fracture and necking indicators at the instant of first element deletion: (a) 1 mm shell element model for NT80, (b) 2 mm shell model for NT27, (c) 2 mm shell model for SB80, and (d) 4 mm shell model for SB27.

Figure 6-13. Comparison of the draw-in of a blank and the distribution of major principal strain between experiments and finite element simulations at punch displacements of (a) 35 mm and (b) 40 mm.

Figure 6-14. Contour plots of fracture and necking indicators on inner and outer surfaces of a deep-drawn triangular cup right before a crack appears.

List of Tables

Chapter 1

Introduction

For the past decades, a great improvement has been made in the experimental and computational mechanics. Numerical simulation became an indispensable step of design practice in a variety of industry such as automotive, aerospace, electronics, and defense to name a few. Engineers use a computational tool to design and optimize manufacturing processes and final products. Finite element analysis (e.g. Bathe, 2006), as one of the most popular numerical tools, requires to solve a set of mathematical equations that govern the behavior of a material for a continuum discretized into a finite number of isoparametric domains.

In particular, deformation of a solid material in the mechanics point of view can largely be decomposed into two parts: elasticity and plasticity. Especially for ductile metal that has only a limited range of elastic deformation, plasticity is of a major concern. Numerous publications in the literature deal with how to mathematically formulate the boundary of an elastic set, its evolution with continuing loading, and the resulting plastic flow.

1.1 Motivation and ductile fracture

Limiting our attention to the automotive industry, the government has been setting ever-stringent regulations on the passenger safety and gas emissions (e.g. the Corporate Average Fuel Economy standards of the US). To meet those requirements, the industry is increasingly applying advanced high strength steels or other lightweight materials that have a high strength-to-weight ratio such as aluminum and magnesium alloys to Body-in-White. However, an increased strength of materials is offset by a reduced ductility (see Fig. 1-1). Consequently, premature fracture occurs under the scenarios with large plastic deformation such as sheet metal forming or car crash. A few examples are shown in Figs. 1-2 and 1-3. Ductile fracture has thus become a worldwide

challenging issue, so the development of an accurate numerical tool to predict ductile fracture of sheet metal is essential. At the same time, such a tool should not be complicated and must be practical enough to be applicable to a fast-moving industry environment.

Figure 1-4 shows the typical morphology of the fracture surface of a ductile material taken by a scanning electron microscope. The magnified view presents the characteristic dimple patterns resulting from a series of microscopic events: void nucleation, growth, and coalescence. A more

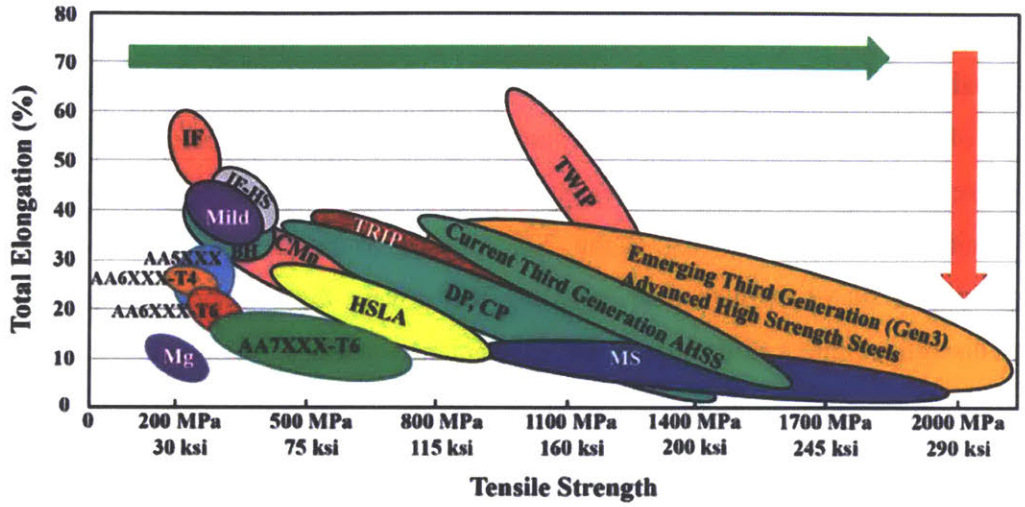

Figure 1-1. Total elongation and tensile strength for different sheet steel, aluminum and magnesium alloys at room temperatures (Schaeffler, 2016)

(a) (b)

Figure 1-2. Ductile fracture during sheet metal forming: (a) square and circular cup drawings of TRIP690 steel (Li et al., 2010) and (b) B-pillar stamping of DP600 and DP980 steels (Sung, 2010).

Figure 1-3. Small overlap crash test of 2016 Hyundai Tucson (courtesy of the Insurance Institute for Highway Safety)

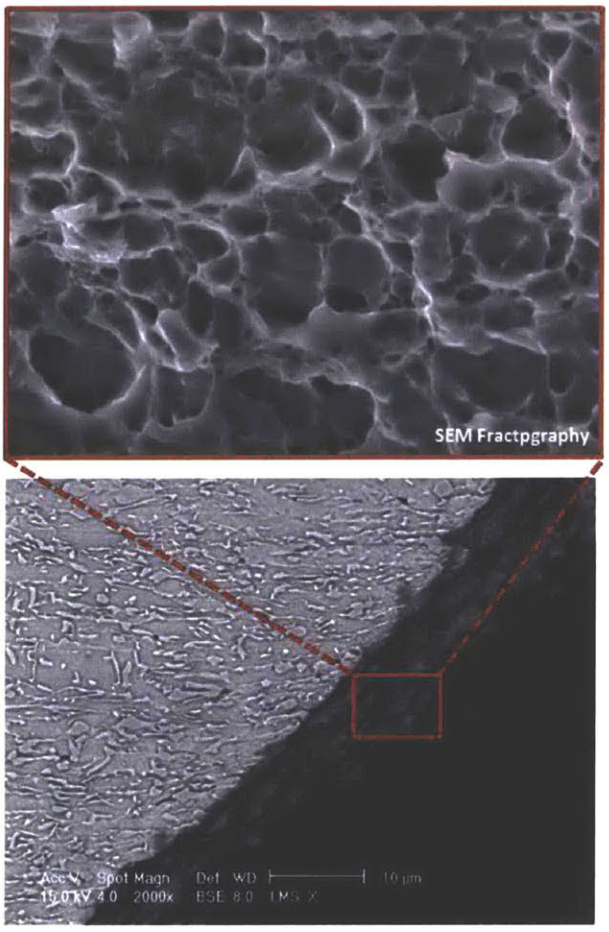

Figure 1-4. SEM fractography of a ductile material, which presents dimple structures

detailed process may be described as follows (see Fig. 1-5). A material in the virgin state may contain a certain level of porosity depending on its manufacturing process. Upon loading, porosity increases by the growth of existing voids and the nucleation of new voids. At the same time, the macroscopic hardening capacity of a material decreases. As a result, the condition for discontinuity in the macroscopic strain fields along a planar interface may be satisfied, and a primary band of localization appears at the mesoscale. Material inside the primary band experiences accelerated void nucleation and growth, and the mechanical fields around individual voids start to interact with one another. A secondary band of localization can appear in this stage at a microscale, which leads to void coalescence and the formation of a macroscopic crack through either inter-void necking or void sheet fracture. Note that some ductile metal may skip a few steps. In the engineering perspective at a macroscopic scale, the onset of ductile fracture may be defined as that of formation of the primary band of localization. Indeed, the steps from ③ to ⑦ in Fig. 1-5 occur in no time, especially in high strength alloy sheets.

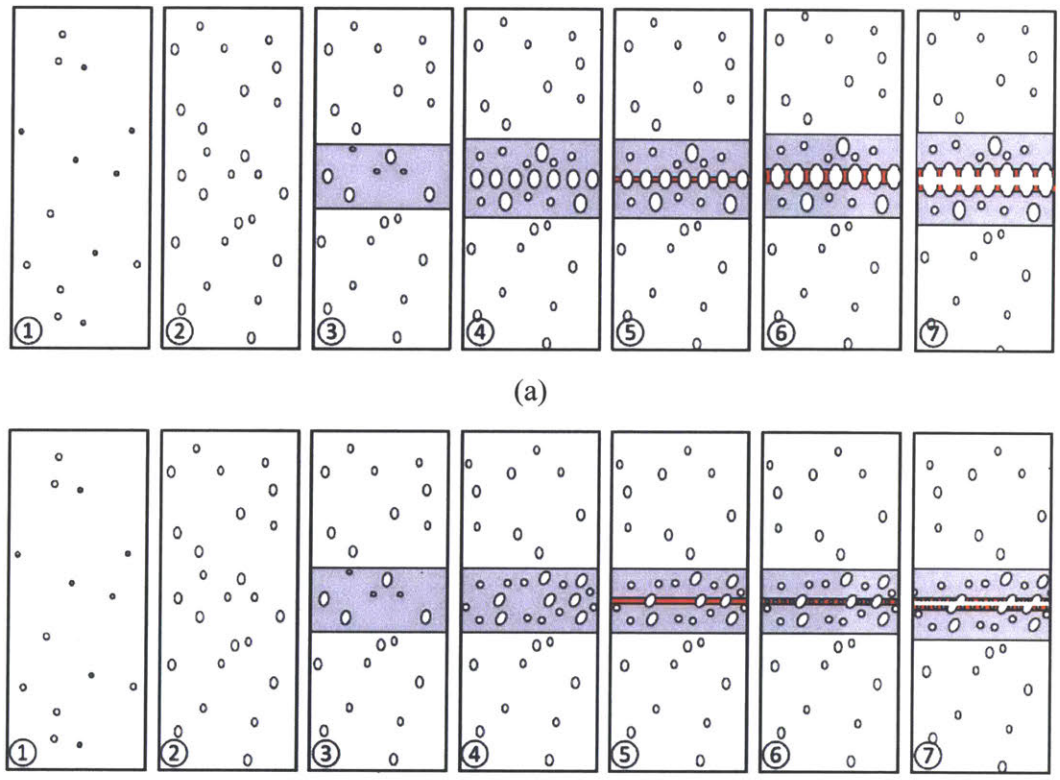

Figure 1-5. Eulerian illustration of ductile fracture process through (a) inter-void necking and (b) void sheet fracture (Mohr and Marcadet, 2015).

1.2 Ductile fracture models

The pioneering research on ductile fracture such as McClintock (1968) and Rice and Tracey (1969) traces a few decades back. They made an effort to describe the effect of hydrostatic pressure on the growth of a cylindrical and a spherical hole in a ductile matrix. A fundamental foundation in the form of porous plasticity was set by Gurson (1977) who analyzed a thick spherical shell subjected to hydrostatic pressure, thereby focusing on the growth of voids. The model is formulated in terms of macroscopic stresses such that the radius of a yield function decreases with an increasing macroscopic mean stress. The effect of void nucleation and coalescence were later incorporated by Chu and Needleman (1980) and Tvergaard and Needleman (1984), respectively. In the latter, the macroscopic yield function shrinks into a point when a void volume fraction reaches the ultimate value. Porous plasticity was further enriched by considering additional aspects, including void shape dependencies (Gologanu et al., 1993;Pardoen and Hutchinson, 2000), enhanced strain hardening model (Leblond et al., 1995), and plastic anisotropy (Benzerga and Besson, 2001;Benzerga et al., 2004). In the meantime, Bao and Wierzbicki (2004) experimentally discovered the cusp between shear and tensile branches on the fracture locus of Al2024-T351 in the space of the equivalent plastic strain and a normalized mean stress. It was successfully captured by a modification to the evolution law of the void volume fraction under shear-dominated stress states introduced by Xue (2008) and Nahshon and Hutchinson (2008). Readers interested in a more comprehensive review about porous plasticity models are referred to Benzerga et al. (2016).

Lemaitre (1985), Chaboche (1988), and Chaboche (1988b) took an alternative approach so-called continuum damage mechanics. An internal damage variable at a macroscopic continuum level is coupled with elastic and plastic moduli in order to represent reduction in the effective load carrying capacity due to material degradation while the variable is incorporated into thermodynamic principles to derive the constitutive equations. Chow and Wang (1987) further accounted for anisotropy.

The third group features a scalar damage indicator in conjunction with non-porous elasticity and plasticity models. Fracture is assumed to occur when the indicator reaches a critical

value. The damage indicator accumulates with a plastic strain increment multiplied by a stress state dependent weighting function. Therefore, the accuracy of the weighting function is of great importance. Early work by Rice and Tracey (1969), McClintock (1968), Cockcroft and Latham (1968), Brozzo et al. (1972), Le Roy et al. (1981), and Clift et al. (1990) belongs to this category. Bao and Wierzbicki (2004b) performed a comparative study on the above damage indicator models using the results of upsetting tests and tensile tests on smooth and round bars. The aforementioned cusp on the fracture locus experimentally measured by Bao and Wierzbicki (2004) triggered the discovery of the Lode angle by Xue (2007) as an additional independent variable that controls material ductility besides the stress triaxiality. This led to the development of more advanced fracture initiation models such as Bai and Wierzbicki (2008a), Bai and Wierzbicki (2010), Lou et al. (2012), and Mohr and Marcadet (2015). Constructing a fracture envelope in a three-dimensional space of the stress triaxiality, Lode angle, and equivalent plastic strain eliminates a cusp and produces a smooth surface. The effect of temperature and strain-rate is of great interest as well because the most of real applications do not occur under the ideal quasi-static loading condition at room temperature. Roth and Mohr (2014) extended the Hosford-Coulomb fracture model by Mohr and Marcadet (2015) towards dynamic loading by adding a Johnson and Cook (1983) type strain-rate dependency. Moreover, Marcadet and Mohr (2015) considered a non-linear damage accumulation to capture the effect of strain reversal on ductility enhancement.

Localized necking is a through-thickness thinning phenomenon that often precedes ductile fracture. It tends to alter the initial plane stress loading into a fully three-dimensional local stress state inside a neck even for thin metal sheets. Therefore, a very fine solid elements are required to capture detailed stress and strain fields in the post-necking regime. A lack of resources in a fast-paced industry dealing with thin-walled structures, however, requires modeling a given part with relatively large shell finite elements for practical reasons: ease of meshing, computational efficiency, and robustness under complicated contact conditions. Luo and Wierzbicki (2010) used the same plasticity and fracture models for both solid and shell discretization to simulate stretch bending of a steel strip over small die radii. Li et al. (2010) did not introduce any special treatment either for shell element models in simulating square and circular cup drawings. In general, fracture was predicted with accuracy when a stress state lies in the shear dominated region or significant bending was superposed onto stretching. This implies that a new ductile fracture model exclusive for shell finite elements need to be developed for situations where localized necking takes place.

Nonetheless, only a few authors dealt with the problem mainly due to an unrealistic constitutive assumption of the plane stress condition from the beginning to the end of plastic deformation. Kõrgesaar et al. (2014) made use of a concept of an averaging unit and obtained a volume-averaged behavior of a fine solid element model subjected to three typical membrane tensile actions over a large surface area of sheet metal to define an equivalent behavior of large shell elements. It reached a conclusion that a mesh size dependence of strain to fracture is stress state dependent and strongest for uniaxial tension. Furthermore, Kõrgesaar and Romanoff (2013) proposed a softening law to simulate crack propagation using large shell elements. Walters (2014) independently pointed out that a scale function to eliminate mesh size sensitivity should be a function of both mesh size and stress states. A partial removal of the mesh size effect was achieved earlier by Lee (2005) through a damage indicator averaged over the characteristic volume element. Andrade et al. (2016) contrived a function that scales up and down a fracture locus and coupled the damage indicator with a material hardening law. Thereby, a global response of force-displacement curves could be successfully regularized and matched with experimental results. A second-order theory, gradient plasticity (e.g. Anand et al., 2012), is another way to address a mesh size sensitivity, but requiring a certain level of fine meshing to capture an essential strain gradient with accuracy.

The commonly missing consideration in all the above remedies for shell elements is the distinction between membrane and bending loading. Although the latter is a predominant deformation mode of thin-walled structures, and yet those remedies were proposed solely based on the behavior of shell elements subjected to membrane loading. Pure bending does not produce localized necking (e.g. Stoughton and Yoon, 2011). Localized necking is not a local phenomenon at an individual material point, but a non-local one through-thickness. Then, shell elements may provide a valid solution up to the onset of fracture initiation with no need for artificial regularization. Therefore, the validity of the currently available regularization techniques for combined bending and tension remains questionable. Moreover, the post-necking response of sheet metal that the existing literature focuses on is observed only at a negligible length scale (order of sheet thickness) in large-scale problems for which shell element discretization is necessary. The complexity of model calibration is another key point to be addressed. The aim of this thesis is to address all the above missing issues in computational modeling of ductile failure with shell elements.

1.3 Thesis outline and objectives

This thesis presents a novel approach towards predicting the initiation of ductile failure of thin metal sheets using shell finite elements. Instead of developing a new shell element type, an effort is made to solve the problem at a material model level for a first-order general-purpose shell element with a reduced integration (type S4R of Abaqus/Explicit element library). This shell element uses either the Kirchhoff-Love or the Reisser-Mindlin plate theory, depending on thickness of a shell. The latter accounts for through-thickness shear flexibility. The new model for shell elements is intended to maintain the existing modeling framework and corresponding material parameters for solid finite elements. An emphasis is put on fracture under pure bending and stretch bending, ubiquitous in thin-walled structures, not limited to in-plane membrane loading. Simplicity is also a key point considered to facilitate a wide use of the model in the industry.

The thesis begins with a review of plasticity models for shell and solid elements. The isotropic von Mises yield function is employed to model high strength steel sheets. The non-quadratic anisotropic plasticity by Barlat et al. (2003) is considered to model aluminum sheets. The micromechanically motivated Hosford-Coulomb (HC) fracture initiation model proposed by Mohr and Marcadet (2015) is presented as a fracture model. This particular choice was made due to its simplicity and accuracy that was proved by several structural validations.

In Chapter 3, the performance of shell elements is evaluated in comparison to solid elements by applying the same plasticity and fracture models and their parameters to both element types. Two simple structural examples are considered. One is a large notched tension experiment where ductile fracture is preceded by localized necking, and the other is a hemispherical punch experiment in which localized necking is delayed until fracture initiation. This section is of critical importance in visualizing a mesh size sensitivity of shell elements and diagnosing its fundamental origin, localized necking.

Chapter 4 introduces a new concept of a Domain of Shell-to-Solid Equivalence (DSSE) as a localized necking criterion under arbitrary non-proportional combined membrane and bending loading. The DSSE, as its name suggests, intends to define the domain of trustworthiness for shell elements, in which their numerical solutions can be trusted and the exiting HC fracture model can

be simply applied with confidence. The MK (Marciniak and Kuczyński, 1967) type localization analysis is first performed to investigate a general shape of a localization locus that demarcates DSSE under proportional membrane loading. A mathematical equation is proposed to fit the locus, and the Considère criterion for plane strain tension is suggested to determine a single model parameter. Non-proportional loading is tackled by a forming severity concept (Bai and Wierzbicki, 2008), and the effect of bending is incorporated by integrating the experimental results by Tharrett and Stoughton (2003). The chapter is closed by proposing a new shell element failure model that combines the DSSE and the HC fracture model. This is named the DSSE-HC model.

In Chapter 5, the accuracy of the DSSE-HC model is evaluated purely numerically in comparison to a very fine solid element model for a variety of loading scenarios: notched tension, hemispherical punch loading on a circular disk, bending followed by tension on a notched strip, and V-bending of a rectangular plate. The main objective of this chapter is to exclude any possible uncertainties and inaccuracies that a specific constitutive theory may possess and evaluate the performance of the proposed model in a virtually perfect environment with the assumption that solid element solutions are exact.

Chapter 6 is concerned with the experimental validation of the DSSE-HC model at a specimen level for 0.82 *mm* thick dual phase steel sheets with the minimum ultimate tensile strength of 980 MPa (DP980). The chapter begins with the characterization of a DP980 steel sheet. Uniaxial tensile tests in three different sheet orientations and a small notched-tension experiment are carried out to determine plasticity parameters. Three ductile fracture experiments proposed by Roth and Mohr (2016) that enable the direct measurement of fracture strain using digital image correlation (Sutton et al., 2009) are additionally conducted to identify the HC model parameters. The localization locus for proportional membrane loading is identified by applying the Considère criterion and validated against a forming limit curve experimentally obtained from Nakazima experiments. Four additional ductile fracture experiments are considered to validate the DSSE-HC model together with the three experiments used for the fracture model calibration. Furthermore, a structural level validation is performed using 1.02 *mm* thick aluminum 6016-T4 sheets. The example of triangular cup-drawing is chosen from Gorji et al. (2016b). The fracture model parameters are calibrated based on the reported Nakazima and circular cup-drawing experiments (Gorji et al., 2016a and b).

Chapter 2

Plasticity and fracture models for steel and aluminum alloy sheets

This chapter is devoted to summarizing the plasticity models for steel and aluminum alloy sheets and the Hosford-Coulomb (HC) ductile fracture initiation model. The latter was originally developed for solid finite elements. Both three-dimensional and two-dimensional expressions are presented for solid and shell finite elements, respectively. The damage indicator framework of the HC model in conjunction with non-porous plasticity is chosen as a basic constitutive law for the current research due to its simplicity, straightforward calibration, and accuracy.

2.1 Plasticity models

In this thesis, two basic phenomenological plasticity models are employed for steel and aluminum alloy. The steel is modeled using the von Mises yield function, while aluminum is modeled using the Yld2000 yield function. All other components of the plasticity model formulation are the same, i.e. both models assume associated flow and isotropic Swift-Voce strain hardening.

Formally, the yield function is written in terms of an equivalent stress $\bar{\sigma}$ and a deformation resistance k,

$$f = \bar{\sigma} - k = 0 \tag{2-1}$$

The isotropic deformation resistance k evolves (irreversibly) as a function of the work-conjugate equivalent plastic strain $\bar{\varepsilon}_p = \int d\bar{\varepsilon}_p$. After integrating the evolution equations, it may be

expressed as the weighted average of a power law (Swift, 1952) and an exponential law (Voce, 1948).

$$k[\bar{\varepsilon}_p] = \alpha A\left(\varepsilon_0 + \bar{\varepsilon}_p\right)^n + \left(1-\alpha\right)\left[k_0 + Q\left(1-\exp\left(-\beta\bar{\varepsilon}_p\right)\right)\right] \tag{2-2}$$

with the Swift parameters $\{A, \varepsilon_0, n\}$, the Voce parameters $\{k_0, Q, \beta\}$, and the weighting factor α.

The equivalent stress of the quadratic isotropic von Mises yield function may be written as

$$\bar{\sigma}_{Mises} = \sqrt{3J_2} \tag{2-3}$$

with J_2 denoting the second invariant of the Cauchy stress deviator.

In the non-quadratic Yld2000-2d yield function (Barlat et al., 2003) for plane stress conditions, the equivalent stress is defined as

$$\bar{\sigma}_{Yld2000-2d} = \frac{1}{2^{1/\alpha_0}}\left(\left|S'_I - S'_{II}\right|^{\alpha_0} + \left|S''_I + 2S''_{II}\right|^{\alpha_0} + \left|2S''_I + S''_{II}\right|^{\alpha_0}\right)^{\frac{1}{\alpha_0}} \tag{2-4}$$

It is written in terms of the principal values $\left(S'_I, S'_{II}\right)$ and $\left(S''_I, S''_{II}\right)$ of two linearly-transformed deviatoric stress vectors

$$\mathbf{s}' = \mathbf{L}'\boldsymbol{\sigma} \text{ and } \mathbf{s}'' = \mathbf{L}''\boldsymbol{\sigma} \tag{2-5}$$

with two transformation matrices

$$\mathbf{L}' = \frac{1}{3}\begin{bmatrix} 2\alpha_1 & -\alpha_1 & 0 \\ -\alpha_2 & 2\alpha_2 & 0 \\ 0 & 0 & 3\alpha_7 \end{bmatrix} \tag{2-6}$$

and

$$\mathbf{L}'' = \frac{1}{9}\begin{bmatrix} -2\alpha_3 + 2\alpha_4 + 8\alpha_5 - 2\alpha_6 & \alpha_3 - 4\alpha_4 - 4\alpha_5 + 4\alpha_6 & 0 \\ 4\alpha_3 - 4\alpha_4 - 4\alpha_5 + \alpha_6 & -2\alpha_3 + 8\alpha_4 + 2\alpha_5 - 2\alpha_6 & 0 \\ 0 & 0 & 9\alpha_8 \end{bmatrix}. \tag{2-7}$$

and a Cauchy stress vector, $\boldsymbol{\sigma} = [\sigma_{11} \quad \sigma_{22} \quad \sigma_{12}]^T$ (with the sheet rolling direction being aligned with the 1-axis). Note that the isotropic Hosford (Hosford, 1972) yield function is recovered when $\alpha_1 = \alpha_2 = \alpha_3 = \alpha_4 = \alpha_5 = \alpha_6 = \alpha_7 = \alpha_8 = 1$. It can be further reduced to the von Mises yield function when setting the exponent to $\alpha_0 = 2$.

Dunand et al. (2012) extended the original model in Eq. 2-4 to general three-dimensional stress states for its application to solid finite elements (e.g. Luo et al., 2012). The model is written as

$$\bar{\sigma}_{Yld2000\text{-}3d} = \frac{1}{2^{1/\alpha_0}} \left(\phi'(\mathbf{s}') + \phi''(\mathbf{s}'') \right)^{\frac{1}{\alpha_0}} \tag{2-8}$$

with

$$\phi'(\mathbf{s}') = \left[\left(s'_{11} - s'_{22} \right)^2 + 4 \left(s'^2_{12} + s'^2_{23} + s'^2_{13} \right) \right]^{\frac{\alpha_0}{2}} \tag{2-9}$$

and

$$\begin{aligned} \phi''(\mathbf{s}'') = & \left[\frac{3}{2} \left(s''_{11} - s''_{22} \right) + \frac{1}{2} \sqrt{\left(s''_{11} - s''_{22} \right)^2 + 4 \left(s''^2_{12} + s''^2_{23} + s''^2_{13} \right)} \right]^{\alpha_0} \\ & + \left[\frac{3}{2} \left(s''_{11} - s''_{22} \right) - \frac{1}{2} \sqrt{\left(s''_{11} - s''_{22} \right)^2 + 4 \left(s''^2_{12} + s''^2_{23} + s''^2_{13} \right)} \right]^{\alpha_0} \end{aligned} \tag{2-10}$$

The stress deviators $\mathbf{s}' = \left[s'_{11} \quad s'_{22} \quad s'_{12} \quad s'_{23} \quad s'_{13} \right]^T$ and $\mathbf{s}'' = \left[s''_{11} \quad s''_{22} \quad s''_{12} \quad s''_{23} \quad s''_{13} \right]^T$ are calculated through two modified transformation matrices, $\mathbf{L}'$ and $\mathbf{L}''$, which are defined as

$$\mathbf{L}' = \frac{1}{3} \begin{bmatrix} 2\alpha_1 & -\alpha_1 & -\alpha_1 & 0 & 0 & 0 \\ -\alpha_2 & 2\alpha_2 & -\alpha_2 & 0 & 0 & 0 \\ 0 & 0 & 0 & 3\alpha_7 & 0 & 0 \\ 0 & 0 & 0 & 0 & 3\alpha_9 & 0 \\ 0 & 0 & 0 & 0 & 0 & 3\alpha_{10} \end{bmatrix} \tag{2-11}$$

and

$$\mathbf{L}''=\frac{1}{9}\begin{bmatrix} -2\alpha_1+2\alpha_4+8\alpha_5-2\alpha_6 & -4\alpha_4+4\alpha_6+\alpha_3-4\alpha_5 & \alpha_3+2\alpha_4-4\alpha_5-2\alpha_6 & 0 & 0 & 0 \\ 4\alpha_3-4\alpha_4-4\alpha_5+\alpha_6 & -2\alpha_3+8\alpha_4+2\alpha_5-2\alpha_6 & -2\alpha_3-4\alpha_4+2\alpha_5+\alpha_6 & 0 & 0 & 0 \\ 0 & 0 & 0 & 9\alpha_8 & 0 & 0 \\ 0 & 0 & 0 & 0 & 9\alpha_{11} & 0 \\ 0 & 0 & 0 & 0 & 0 & 9\alpha_{12} \end{bmatrix} \tag{2-12}$$

for a full three-dimensional Cauchy stress vector $\boldsymbol{\sigma}=[\sigma_{11}\ \ \sigma_{22}\ \ \sigma_{33}\ \ \sigma_{12}\ \ \sigma_{23}\ \ \sigma_{13}]^T$. Four additional parameters $\{\alpha_9\ \ \alpha_{10}\ \ \alpha_{11}\ \ \alpha_{12}\}$ account for the anisotropy under through-thickness shear stresses. It is noted that Eq. 2-8 with $\alpha_i=1$ for $\forall i\in\{1,2,\cdots,12\}$ does not reduce to an isotropic function, different from Eq. 2-4.

2.2 Hosford-Coulomb fracture initiation model

2.2.1 Stress state characterization

A stress is fully defined by six independent components of a Cauchy stress tenor $\boldsymbol{\sigma}$. A "stress state" is rather understood as its direction, and as a result, its degree of freedom is reduced by one (magnitude). For a principal stress vector $(\sigma_{p1},\ \sigma_{p2},\ \sigma_{p3})$ with $\sigma_{p1}\geq\sigma_{p2}\geq\sigma_{p3}$ as an isotropic measure, its direction can be conveniently expressed by two parameters. The most widely used parameters in the fracture mechanics community are the stress triaxiality η and the normalized Lode angle $\bar{\theta}$. The former is defined as the ratio of the mean stress σ_m to the von-Mises equivalent stress $\bar{\sigma}_{Mises}$.

$$\eta=\frac{\sigma_m}{\bar{\sigma}_{Mises}} \tag{2-13}$$

with

$$\sigma_m=\frac{1}{3}(\sigma_{11}+\sigma_{22}+\sigma_{33})=\frac{1}{3}(\sigma_{p1}+\sigma_{p2}+\sigma_{p3}) \tag{2-14}$$

The normalized Lode angle $\bar{\theta}$ ranging from -1 to 1 is expressed as a function of the third invariant (determinant) J_3 of the Cauchy stress deviator.

$$\bar{\theta} = 1 - \frac{2}{\pi} \arccos\left(\frac{27}{2} \frac{J_3}{\bar{\sigma}_{Mises}^3} \right). \tag{2-15}$$

A combination of the above two parameters $(\eta, \bar{\theta})$ specifies a three-dimensional stress state. For example, pure-shear, uniaxial tension, plane strain tension, and equi-biaxial tension are specified by $(0, 0)$ $(1/3, 1)$, $(1/\sqrt{3}, 0)$, and $(2/3, -1)$. According to Bai and Wierzbicki (2008a), there exists a unique relation between the two parameters for the plane stress condition.

$$\bar{\theta} = 1 - \frac{2}{\pi} \cos^{-1}\left(-\frac{27}{2} \eta \left(\eta^2 - \frac{1}{3} \right) \right) \text{ for } -\frac{2}{3} \le \eta \le \frac{2}{3} \tag{2-16}$$

Therefore, a single parameter, the stress triaxiality, can uniquely define a current stress state for plane stress conditions. A more detailed geometrical interpretation of the two parameters can be found in Bai and Wierzbicki (2010).

2.2.2 Formulation of Hosford-Coulomb model

The Hosford-Coulomb fracture model (HC) proposed by Mohr and Marcadet (2015) is micromechanically motivated and predicts the equivalent plastic strain at fracture for proportional loading as a function of the stress triaxiality and the Lode angle. It postulates that a macroscopic crack appears in an uncracked body when a linear combination of a Hosford equivalent stress (Hosford, 1972) and a normal stress on the maximum shear stress plane reaches a critical value.

$$\bar{\sigma}_{Hosford} + c(\sigma_I + \sigma_{III}) = b_0 \tag{2-17}$$

By coordinate transformation to the Haigh-Westergaard space $(\bar{\sigma}_{Mises}, \eta, \bar{\theta})$ and mapping from a stress space to a mixed stress-strain space using a simple power law approximation, the following concise analytical expression is obtained.

$$\bar{\varepsilon}_{HC}^{pr}[\eta, \bar{\theta}] = b(1+c)^{\frac{1}{n_f}} \left[\left\{ \frac{1}{2} \left((f_1 - f_2)^a + (f_2 - f_3)^a + (f_1 - f_3)^a \right) \right\}^{\frac{1}{a}} + c(2\eta + f_1 + f_3) \right]^{-\frac{1}{n_f}} \tag{2-18}$$

with three Lode angle dependent trigonometric functions

$$f_1[\bar{\theta}] = \frac{2}{3}\cos\left(\frac{\pi}{6}\left(1-\bar{\theta}\right)\right), f_2[\bar{\theta}] = \frac{2}{3}\cos\left(\frac{\pi}{6}\left(3+\bar{\theta}\right)\right), \text{ and } f_3[\bar{\theta}] = -\frac{2}{3}\cos\left(\frac{\pi}{6}\left(1+\bar{\theta}\right)\right). \quad (2\text{-}19)$$

The model parameter b is equal to the strain to fracture for uniaxial or equi-biaxial tension, being responsible for an overall height of a fracture envelope. Its dependency on η and $\bar{\theta}$ is controlled by c and a respectively. The exponent n_f adjusts the dependency on both η and $\bar{\theta}$ simultaneously. Roth and Mohr (2014) recommended to use $n_f = 0.1$ as a material-independent transformation coefficient.

However, there does not exist an ideally proportional loading condition in real applications. A material point undergoes changes in stress states. To tackle such non-proportional loading conditions, a scalar fracture indicator D_{HC} is integrated over each plastic strain increment

$$dD_{HC} = \frac{d\bar{\varepsilon}_p}{\bar{\varepsilon}_{HC}^{pr}[\eta,\bar{\theta}]} \quad (2\text{-}20)$$

while fracture is assumed to initiate when

$$D_{HC} = 1. \quad (2\text{-}21)$$

This gives $\bar{\varepsilon}_p = \bar{\varepsilon}_{HC}^{pr}[\eta,\bar{\theta}]$ for proportional loading conditions. Consequently, the corresponding finite element is removed from the rest of a finite element model by setting $\boldsymbol{\sigma} = \mathbf{0}$.

Roth and Mohr (2014), Marcadet and Mohr (2015), and Tancogne-Dejean et al. (2016) extended the above original HC model for quasi-static loading to dynamic loading, reverse loading, and probabilistic fracture, respectively. The accuracy of the model was confirmed at a structural level. Pack and Roth (2016) successfully applied the dynamic HC model to the second Sandia Fracture Challenge (Boyce et al., 2016) and predicted crack initiation and propagation of a titanium alloy with great accuracy. Pack and Marcadet (2015) applied the HC model for reverse loading to the three-point bending of a hot stamped rocker panel and demonstrated the importance of considering the enhanced ductility under strain reversal in order to accurately predict the location of the crack.

Chapter 3

Comparative study between solid and shell elements

In this chapter, to gain some insight into the challenges related to predicting ductile fracture with shell element models, two simple structural examples are analyzed using very fine solid and shell elements. They are a large notched tension and a hemispherical punch test on a circular disk. Herein, a purely computational study is pursued to exclude any uncertainty and inaccuracy that a specific constitutive law may possess. The mechanical behavior of a material is assumed to be completely known. To this end, the plasticity and fracture models presented in Chapter 2 and their parameters for a typical advanced high strength steel are applied to both solid and shell element models. The main objective is to investigate a so-called mesh size sensitivity and its origin.

3.1 Material properties

The material chosen for this purely computational study is a 1 *mm* thick dual phase steel sheet with the minimum ultimate tensile strength of 780 MPa (DP780). Roth and Mohr (2016) characterized a DP780 sheet with the non-associated quadratic anisotropic plasticity (Stoughton, 2002, Cvitanić et al., 2008, and Mohr et al., 2010) and the HC fracture model based on a comprehensive experimental program. However, for the current study, the yield function and the flow rule are simplified as the isotropic von Mises and associated flow to further eliminate constitutive complexity and uncertainty. Yet, a mixed Swift-Voce law in Eq. 2-2 is maintained to predict an accurate hardening behavior for small, moderate, and very large strain. The corresponding stress-strain curve is shown in Fig. 3-1a.

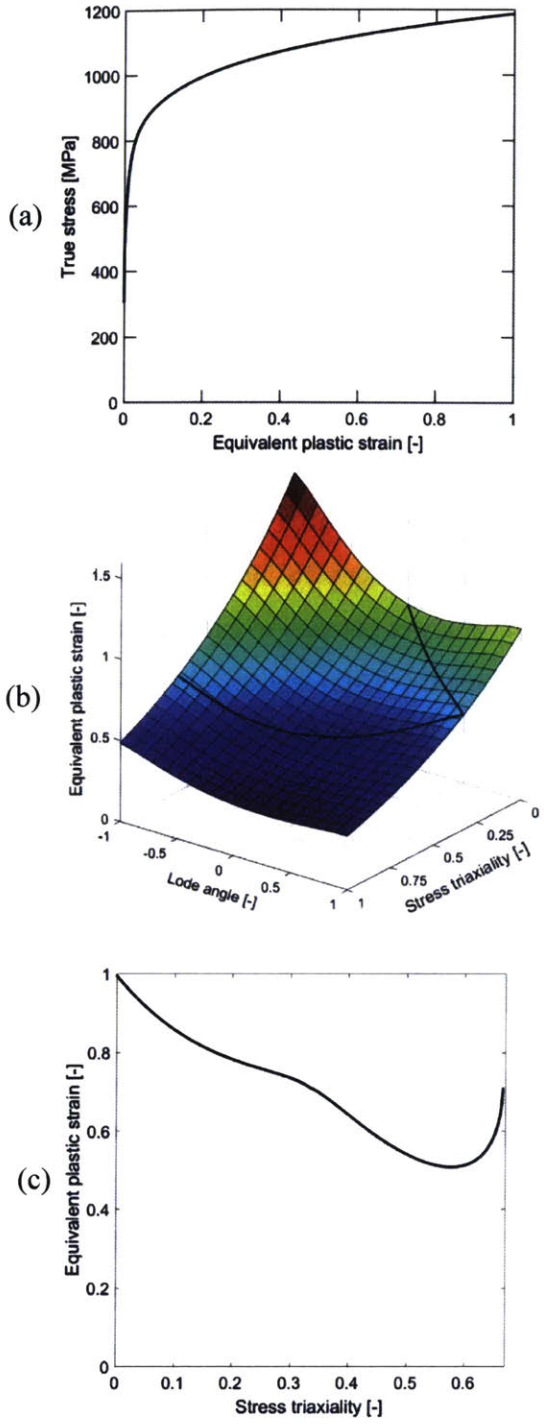

Figure 3-1. Properties of a DP780 steel sheet: (a) equivalent stress versus equivalent plastic strain curve (strain hardening); (b) Hosford-Coulomb failure surface showing the equivalent plastic strain to fracture as a function of the stress triaxiality and the Lode parameter for proportional loading; (c) representation of the same fracture model for plane stress conditions.

Figure 3-1b represents the HC fracture envelope for proportional loading conditions in a three-dimensional space of the stress triaxiality, Lode angle, and equivalent plastic strain to fracture. Note that it predicts an exponential decay of ductility with increasing triaxialities at a given Lode angle. Figure 3-1c depicts the same model, but only for plane stress conditions in a two-dimensional space of the stress triaxiality and equivalent strain to fracture. Please note that strain to fracture for plane strain and uniaxial tension are 0.51 and 0.71, respectively. Table 3-1 summarizes the plasticity and fracture model parameters for a DP780 steel sheet.

Plasticity parameters

A [MPa]	ε_0	n	k_0 [MPa]	Q [MPa]	β	α
1315.4	0.28E-4	0.146	349.5	536.4	93.1	0.7

Fracture parameters

a	b	c
1.61	0.71	6.2E-02

Table 3-1. Plasticity and fracture model parameters of a 1 *mm* thick DP780 steel.

3.2 Large notched tension experiment

A numerical comparative study begins with a tensile experiment on a $t = 1$ *mm* thick, $w = 80$ *mm* wide, and $l = 120$ *mm* long flat notched specimen (NT80) whose width is reduced to 40 *mm* at its center by symmetric circular cutouts of $R = 80\,mm$ radius.

3.2.1 Solid element solution

Due to the symmetry of the mechanical system, only one eighth of the specimen is modeled (see Fig, 3-2c). The specimen gage section is discretized with three different meshes of eight-node first-order solid elements with reduced integration (C3D8R of the Abaqus (2016) element library). The meshes featured 2, 4, and 8 elements along the thickness direction (i.e. an edge length of 0.25

mm, 0.125 *mm*, and 0.0625 *mm*, respectively). The corresponding in-plane element dimensions are 0.4 *mm*, 0.2 *mm*, and 0.1 *mm*. The specimen is uniaxially loaded with zero normal displacement boundary conditions on the three symmetry planes. All solid element simulations are carried out up to the same total axial displacement of 5.58 *mm*.

Figure 3-2a depicts the computed force-displacement curves and the evolution of the equivalent plastic strain at the integration point of the most-deformed (critical) element in the center on the mid-plane up to the displacement at which the first element fails according to the HC model for the finest mesh. Both the (global) force and (local) strains appear to converge as a function of the mesh density, which is in agreement with the findings of Dunand and Mohr (2010). Selected contour plots of the equivalent plastic strain distribution are shown in the top row of Fig. 3-2c for the finest mesh. Number labels indicate the corresponding instants on the force- and strain-displacement curves in Fig. 3-2a. Approximately uniform strain fields along the thickness direction are observed up to the maximum force (point ①). Beyond this point, the equivalent plastic strain rate increases substantially near the specimen center. However, up to point ②, the equivalent plastic strain on the specimen surface and mid-plane are still nearly identical (compare dotted and solid green curves in Fig. 3-2a). In other words, the strain gradient along the thickness direction is still small as compared to that along the specimen width and longitudinal directions. In the last stage before fracture initiation (from ② to ③), a diagonal localization band becomes apparent in the plane of the specimen, which is accompanied by the development of a pronounced through-thickness strain gradient.

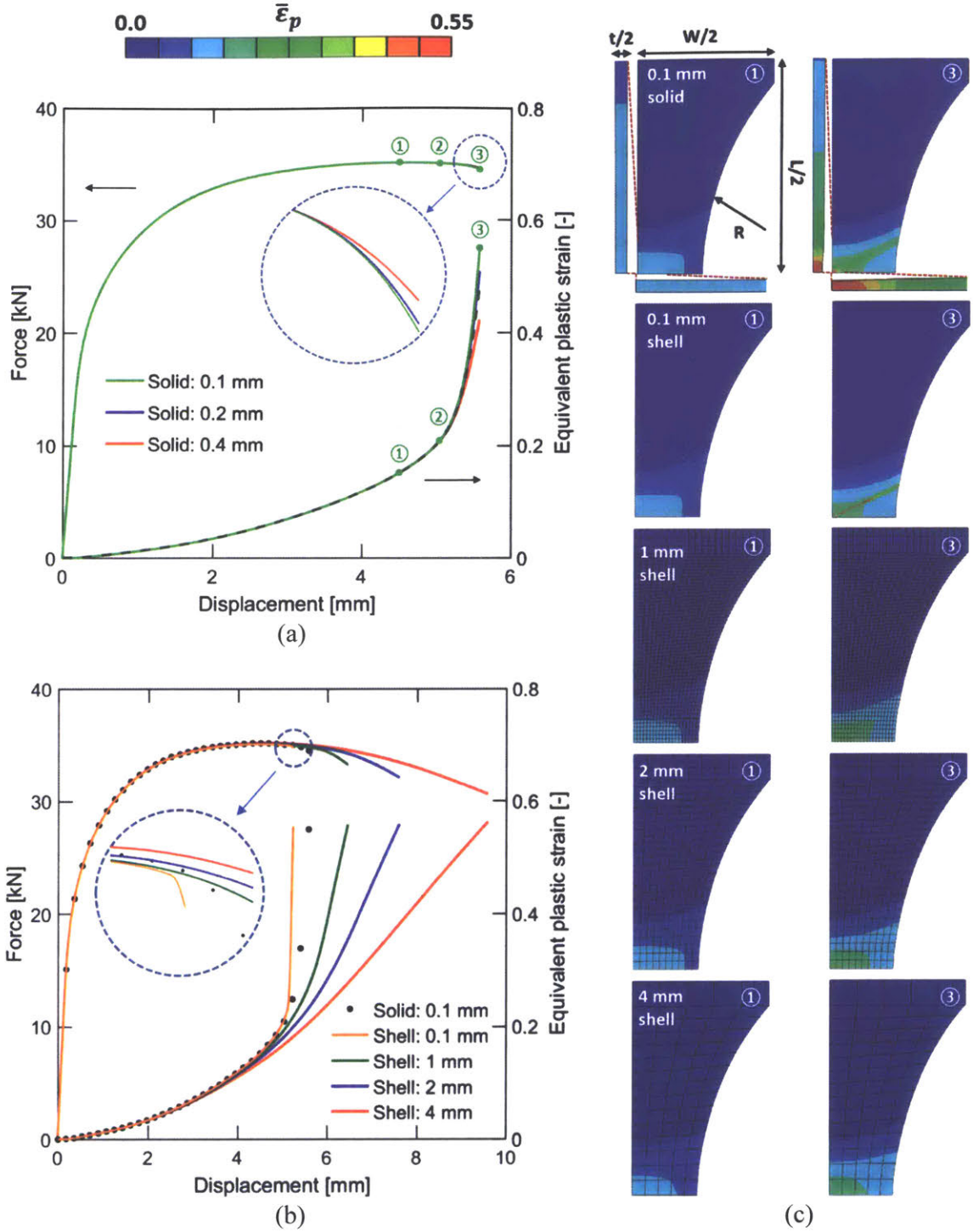

Figure 3-2. Simulation results for notched tension (NT80): force and equivalent plastic strain as a function of the applied displacement as obtained using (a) solid, and (b) shell element meshes. (c) Selected contour plots of the equivalent plastic strain distribution.

3.2.2 Shell element solution

The corresponding shell element simulations are performed using the four-node general purpose shell element with a reduced-integration (type S4R of the Abaqus (2016) library). The element makes use of bi-linear interpolation for three displacement and three rotational degrees of freedom and chooses either thin (Kirchhoff-Love) or thick shell (Reissner, 1945-Mindlin, 1951) formulation depending on thickness of a shell defined by a user. Note that the latter allows for transverse flexibility. The S4R shell considers finite membrane strains and thickness change. Integration to form the element stiffness, the mass matrix, and distributed loadings is performed at a single Gauss point on the reference plane of a shell. The first-order shell with a reduced integration and an hourglass control proved to be appropriate for large deformation with a steep strain gradient. Therefore, the S4R shell is well suited for a ductile fracture problem for thin-walled structures. The shortest element edge length is reported to describe the size of the elements used for meshing.

Four shell element models are built: 0.1 *mm*, 1 *mm*, 2 *mm*, and 4 *mm*. All simulations are terminated at the instant of first element failure as predicted by the HC fracture criterion (using the same material parameters as with the solid element simulations). The computed force and local equivalent plastic strain versus displacement curves for the shell meshes are shown in Fig. 3-2b along with the solution provided by the finest solid element mesh. At the structural level, we see that all shell models are able to predict the force-displacement curves up to the point of fracture in the solid model (u_f=5.58 *mm*) with reasonable accuracy. However, the fracture is predicted at very different instants when applying the HC model to the shell computations. The finest shell mesh underestimates the fracture displacement by 6%, while the fracture displacement is overestimated by 16%, 36% and 72% by the 1 *mm*, 2 *mm*, and 4 *mm* meshes, respectively. The main observation is that the shell solution follows the solid element solution up to the point where through thickness necking occurs. Beyond this point, the fine shell element solution seems to diverge, i.e. the force drops rather abruptly and the local strain increases in an uncontrolled manner.

It is interesting to observe that, despite this divergence, the finest shell element model provides a reasonable estimate of the displacement to fracture. It is sufficiently fine to allow for the formation of a through-thickness neck. From the kinematics perspective, the latter requires a

fine discretization in the plane of the specimen because of its diagonal orientation (Fig. 3-2c). However, unlike the solid element mesh, the fine shell element model cannot describe the development of specimen surface curvature during the formation of a through-thickness neck. Consequently, the out-of-plane tensile stress cannot build-up (i.e. the plane stress conditions prevail in shell models). This implies that the increase in in-plane tensile load carrying capacity due to the built-up of an out-of-plane tensile stress is not captured by the shell model. As a result, the plastic deformation localizes in a single row of shell elements after the onset of through-thickness necking, which explains the apparent divergence of the local strains. In the solid element mesh, the deformation also localizes in a narrow zone after the onset of through-thickness necking, but the width of the band is not set by the element size. Instead, it is defined by the hardening behavior of the material, the specimen thickness, and the in-plane geometry. In the fine shell model, fracture after through-thickness necking will occur at a stress state that is close to perfect transverse plane strain tension, i.e. at a stress triaxiality of η=0.58 and a Lode angle parameter of $\bar{\theta}$ =0.0. In the solid model, the stress triaxiality continues to increase during through-thickness necking, reaching stress triaxialities higher than η>0.58.

In practice, the width of a localized neck is usually expected to be comparable to the sheet thickness (Pearce, 1991, Stoughton and Zhu, 2004, and Koistinen, 2012). If the displacement is monitored at a length scale that is much larger than the sheet thickness (as in the present example), the difference between the displacement up to the onset of through-thickness necking, u_n, and the displacement to fracture, u_f, will be small,

$$u_f = (1+\delta)u_n \quad \text{with} \quad \delta << 1. \tag{3-1}$$

Moreover, according to the above considerations, the displacement to fracture predicted by the fine shell element mesh will be sandwiched between these two displacements,

$$u_n < u_f^{shell} < u_f. \tag{3-2}$$

Even though the shell model prediction is expected towards the necking displacement with decreasing element size h,

$$\lim_{h\to 0} u_f^{shell} = u_n, \tag{3-3}$$

the error in the predicted displacements to fracture will be small for fine shell element meshes.

The simulation results also show that the force-displacement curve and the local strain histories can be predicted with reasonable accuracy using coarse shell element meshes. However, the predictions of the displacements to fracture with coarse shell element meshes is far more troublesome. This is attributed to two effects:

1. First, when the edges of the shell element are much larger than the sheet thickness, the shell model overestimates the width of the through-thickness neck, which will then also result in a higher displacement to fracture.
2. Secondly, if the mesh is too coarse, the formation of a localization band is prohibited by the in-plane kinematics (e.g. in the present example, the diagonal localization band could not develop in the coarse meshes, see Fig. 3-2c). As a result, the deformation will not localize in a narrow band and the strains will not diverge. Consequently, coarse meshes will predict fracture well beyond the point at which through-thickness necking begins in computations with fine meshes.

With regards to the second effect, note that the in-plane mesh density required for capturing the deformation fields up to the point of through thickness necking is much lower than that required beyond this point. In other words, the required mesh quality changes throughout the course of deformation, which is considered as the main challenge in predicting fracture in situations where through-thickness necking takes place. It is worth noting that the same challenge applies to solid element meshes.

We also repeated the above analysis for a specimen with a much tighter notch (R=27 *mm*, NT27) whose results led to the same conclusions as with the NT80 specimen as demonstrated in Fig. 3-3.

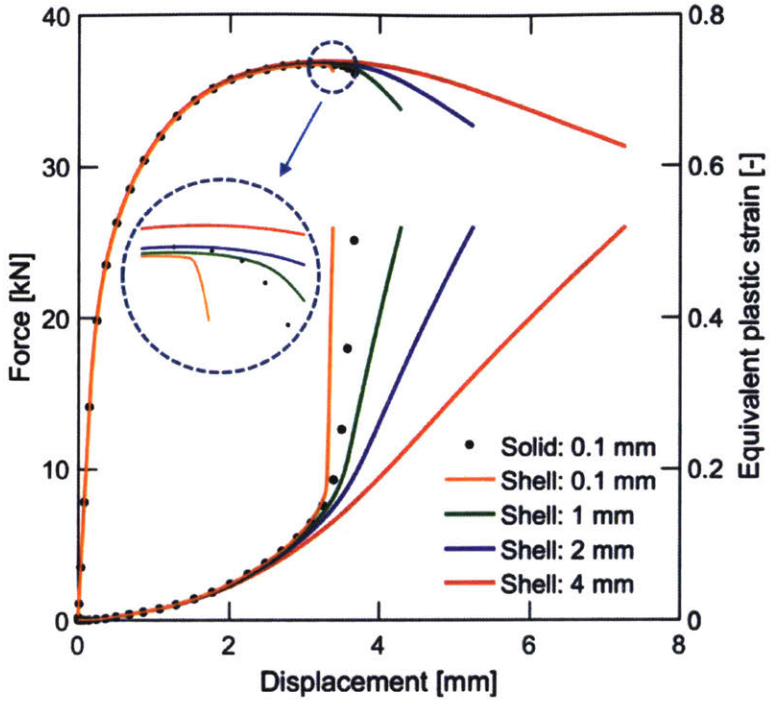

Figure 3-3. Simulation results for notched tension with a tighter notch (R=27 *mm*, NT27)

3.3 Hemispherical punch experiment

The second structural example is the out-of-plane loading of an 80 *mm* diameter disc specimen (fully-clamped) with a hemispherical punch of 30 *mm* radius. The punch is modeled as an analytical rigid body with the frictionless surface-to-surface penalty contact between the punch and the sheet.

3.3.1 Solid element solution

In close analogy with the analysis of the NT80 experiment, C3D8R solid element meshes of different density are used to discretize a quarter of the disc: in-plane edge length of 0.4 *mm*, 0.2 *mm*, and 0.1 *mm* with 4, 8, and 16 elements through the entire thickness. The same punch stroke of 22 *mm* is applied to the three meshes with the zero normal displacement boundary condition on two symmetry planes and the nodes on the lateral surface at R=40 *mm* fully constrained. It is the displacement at which the first element is eliminated by the HC fracture criterion for the finest mesh. The resulting force- and strain-displacement curves are shown in Fig. 3-4a. All three solid meshes predict the identical response, not just globally but also locally. As opposed to the notched tension experiments, the force increases monotonically, and the equivalent plastic strain rate increases gradually throughout the deformation. The strain level on the inner and the outer surface at the apex of the dome is also very similar (compare dotted and solid green curves in Fig. 3-4a). The distinct difference at the displacements less than 10 *mm* is mainly caused by the dominance of bending, which in the later stage turns into a stretching-dominated mode. Figure 3-4c depicts the distribution of equivalent plastic strain at four instants labeled on the curves of Fig. 3-4a. The through-thickness strain gradient at ① fades away towards ②. Note that the highly deformed red-colored area at the onset of fracture (④) is much wider than the NT80 specimen. All of these notable differences are related to the absence of localized necking in the punch-loaded specimens.

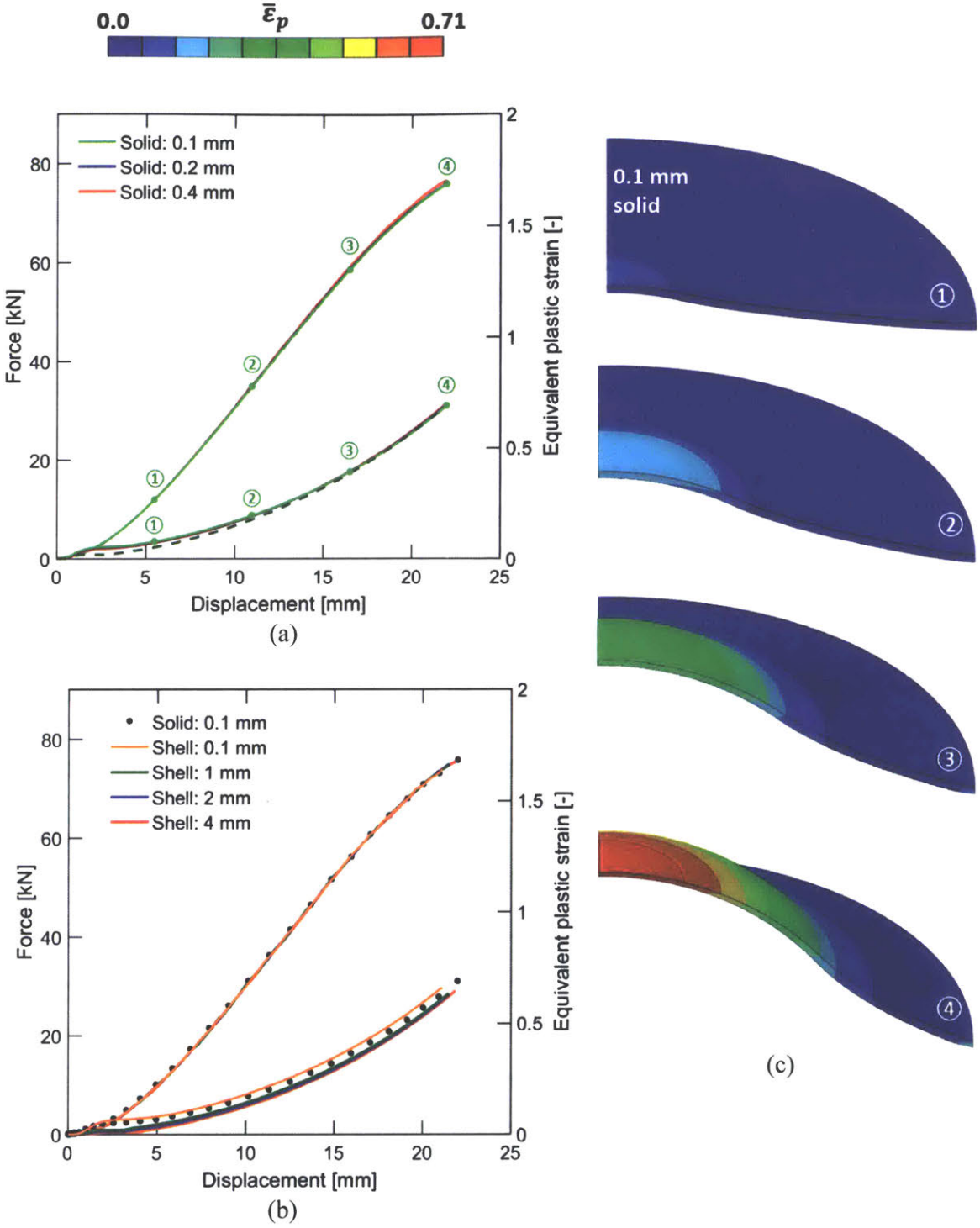

Figure 3-4. Simulation results for hemispherical punch loading: force and equivalent plastic strain as a function of the punch displacement for (a) solid, and (b) shell element meshes. (c) Selected contour plots of the equivalent plastic strain distribution.

3.3.2 Shell element solution

Four shell element simulations featuring the mesh size of 0.1 *mm*, 1 *mm*, 2 *mm*, and 4 *mm* and five integration points through thickness with Simpson's rule are also performed until the first element failure is predicted by the HC fracture model in each simulation. The corresponding results are plotted in Fig. 3-4b. It is remarkable to see that all four force-displacement curves lie exactly on top of the solid element solution. The displacement to fracture also agrees very well with a slight underestimation by 4% for the finest shell element model. A small bump at the displacement of 2 *mm* on the strain-displacement curve is due to the initial bending by a point load, which can only be captured by a very fine mesh. The good agreement of the shell and solid element solutions demonstrates the exceptional performance of shell elements regardless of a mesh size (within the range considered). This agreement is not only observed with regards to the elasto-plastic deformation response, but it also holds true for the predictions of the instants of fracture initiation.

3.4 Conclusions

It is inferred from the above two examples for thin-walled structures, that the predictions of shell element models are

1. reliable in situations where ductile fracture is *not* preceded by localized necking, while
2. unreliable in situations where localized necking precedes ductile fracture. Irrespective of the mesh density, shell element models cannot describe the three-dimensional mechanical fields within a localized neck.

Limiting our attention to applications where the fracture displacement for a given sheet structure is significantly greater than the sheet thickness (e.g. stamping or crashworthiness problems), it is reasonable to assume that the displacement to through-thickness necking is close to the displacement to fracture. The modeling of the through-thickness necking process is thus not necessary. Here, we propose to assume fracture initiation not only when the HC criterion is fulfilled, but also when through thickness necking initiates. When applying this assumption, the entire large deformation response of a thin-walled structure can be conveniently predicted using

shell element models. However, we need to supply a criterion that predicts the onset of through-thickness necking in addition to fracture.

We therefore introduce the so-called Domain of Shell-to-Solid Equivalence (DSSE) to predict the onset of through-thickness necking. In sheet metal forming, the Forming Limit Curve (FLC) (Keeler and Backhofen, 1964 and Goodwin, 1968) is usually used to predict through-thickness necking. Different from the FLC, the DSSE will also be able to distinguish between membrane and bending loading conditions. It will also account for the effect of complex loading histories on necking initiation. The combination of the DSSE and the HC fracture model is then recommended for predicting the failure with shell element models. This new shell element failure model is formulated in Chapter 4.

Chapter 4

Shell element failure model

The detailed analysis of two structural examples in Chapter 3 revealed that the challenges in predicting ductile fracture using shell finite elements are attributable to the inability of shell elements to predict and deal with the formation of a through-thickness neck. Therefore, a localized necking criterion that can account for complex loading scenarios should be additionally provided. To this end, a new concept of the Domain of Shell-to-Solid-Equivalence (DSSE) is proposed. Chapter 4 focuses on how to define DSSE and finally proposes a novel ductile fracture model for shell finite element simulation of large thin-walled structures.

4.1 Domain of Shell-to-Solid Equivalence (DSSE)

The DSSE is simply a localized necking criterion for sheet metals subjected to a non-radial (proportional) combined membrane and bending loading. This section begins with a numerical MK (Marciniak and Kuczyński, 1967) type localization analysis to compute a general shape of the DSSE under proportional membrane loading.

4.1.1 Marciniak-Kuczynski model

As an alternative to solving the bifurcation problem at the material level, the MK analysis will be performed using finite element simulation with the plane stress shell elements (type S4R of the Abaqus (2016) element library). The MK model is defined as follows:

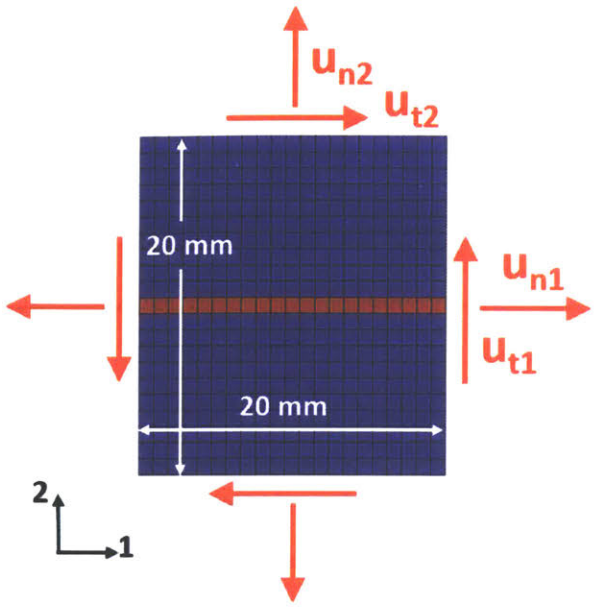

Figure 4-1. Finite element model with central zone of reduced thickness (red)

(i) A square 20×20 mm^2 unit cell is discretized using S4R shell elements of an edge length of 1 *mm* as shown in Fig. 4-1.

(ii) An initial through-thickness imperfection is introduced to the central row of elements,

$$f_0 = 1 - \frac{\vartheta_{red}}{\vartheta_{blue}} \tag{4-1}$$

with ϑ_{red} and ϑ_{blue} denoting the initial thicknesses of the sheet inside and outside the central groove, respectively. The analysis is repeated with $\vartheta_{blue} = 1$ *mm* for three different imperfection values of f_0 (0.5%, 1%, and 1.5%) to gain some insight into the imperfection sensitivity of the reported results.

(iii) Periodic boundary conditions are imposed to the nodes on opposite sides. The macroscopic deformation gradient $\mathbf{F}$ is then controlled by the average axial (u_{n1} and u_{n2}) and tangential displacements (u_{t1} and u_{t2}) applied to the unit cell boundaries (Fig. 4-1),

$$[\mathbf{F}]=\begin{bmatrix} u_{n1}/L+1 & u_{t2}/L & 0 \\ u_{t1}/L & u_{n2}/L+1 & 0 \\ 0 & 0 & \mathrm{F}_{33} \end{bmatrix}. \tag{4-2}$$

In a rotation-free deformation field, the deformation gradient is symmetric and may be written as

$$\mathbf{F}[t]=\sum_{i=1}^{3}\lambda_{pi}[t]\mathbf{e}_{pi}\otimes\mathbf{e}_{pi} \tag{4-3}$$

where λ_{pi} and $\mathbf{e}_{pi}$ denote the principal stretch and the unit vector in the i-th principal stretch direction, respectively. In the present problem, $\mathbf{e}_{p3}$ is assumed to be always normal to the 1-2 plane. For an isotropic material, the principal stress directions coincide with the principal stretch directions. Moreover, we can make use of the flow rule to relate the stress triaxiality η to the principal plastic strain increment ratio $\gamma=d\varepsilon_{p2}^{p}/d\varepsilon_{p1}^{p}$,

$$\eta=\frac{1}{\sqrt{3}}\frac{1+\gamma}{\sqrt{1+\gamma+\gamma^2}} \quad \text{for} \quad -0.5\le\gamma\le 1. \tag{4-4}$$

Using Hencky's strain measure and assuming proportional loading, the equivalent plastic strain may be expressed as

$$\bar{\varepsilon}_p\approx\ln\lambda_{p1}\frac{2}{\sqrt{3}}\sqrt{\left(1+\gamma+\gamma^2\right)}. \tag{4-5}$$

For a constant equivalent plastic strain rate $\dot{\bar{\varepsilon}}_p$, the stretch histories $\lambda_{p1}[t]$ and $\lambda_{p2}[t]$ then read

$$\begin{aligned}\lambda_{p1}[t]&=\exp\left(\frac{\sqrt{3}\cdot\dot{\bar{\varepsilon}}_p\cdot t}{2\sqrt{\left(1+\gamma+\gamma^2\right)}}\right)\\ \lambda_{p2}[t]&=\exp\left(\frac{\sqrt{3}\cdot\gamma\cdot\dot{\bar{\varepsilon}}_p\cdot t}{2\sqrt{\left(1+\gamma+\gamma^2\right)}}\right)\end{aligned}. \tag{4-6}$$

Furthermore, if ϕ defines the angle between the direction of the maximum principal stress (vector $\mathbf{e}_{p1}$) and the localization band (always the horizontal 1-direction of the unit cell), the macroscopic deformation gradient components must read

$$
\begin{aligned}
F_{11}[t] &= \lambda_{p1}[t]\cos^2\phi_0 + \lambda_{p2}[t]\sin^2\phi_0 \\
F_{22}[t] &= \lambda_{p1}[t]\sin^2\phi_0 + \lambda_{p2}[t]\cos^2\phi_0 \\
F_{12}[t] &= \left(\lambda_{p1}[t] - \lambda_{p2}[t]\right)\sin\phi_0\cos\phi_0 \\
F_{21}[t] &= \left(\lambda_{p1}[t] - \lambda_{p2}[t]\right)\sin\phi_0\cos\phi_0
\end{aligned}
\tag{4-7}
$$

with ϕ_0 denoting the initial angle. As discussed by Hill (1952) and Hosford (2010), a theoretical lower limit for the orientation ϕ_0 (for biaxial tension) is given by the angle ψ,

$$
\tan\psi = \sqrt{-\frac{d\varepsilon_{p1}^p}{d\varepsilon_{p2}^p}} = \sqrt{-\frac{1}{\gamma}} \tag{4-8}
$$

Therefore, for a given stress triaxiality η, the MK- analysis is performed for a range of orientations $\psi \le \phi_0 \le \psi + 10^\circ$ with $\Delta\phi_0 = 1^\circ$, before reporting the minimum equivalent plastic strain as strain to localization.

In a given computation, the onset of localization is defined by the criterion

$$
\left|\frac{d\eta}{d\bar{\varepsilon}_p}\right| >> 1 \tag{4-9}
$$

4.1.2 DSSE for proportional membrane loading

Figure 4-2 shows the loading histories of an element outside the groove for each MK unit cell analysis together with a fracture locus in a black solid line. The stress triaxiality is approximately constant all the way to the onset of localization at which Eq. 4-9 is fulfilled, which implies proportional loading. Figure 4-3 depicts the DSSEs for three imperfection values as determined from the MK analysis for biaxial tension ($1/3 \le \eta \le 2/3$). As expected from the literature on FLCs, through-thickness necking occurs particularly early under the plane strain tension condition, while necking strains increase monotonically as the stress state approaches the uniaxial or biaxial tension limits. As the value of initial through-thickness imperfection decreases, the DSSE moves upward, which is a well-known property of MK-analysis results.

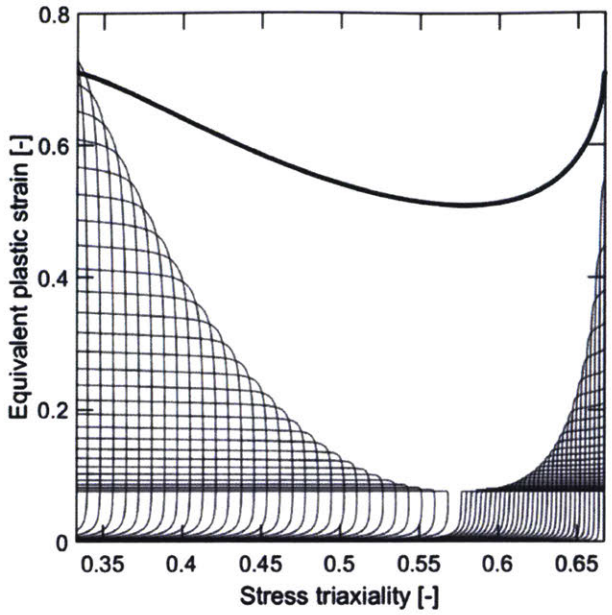

Figure 4-2. Loading paths for different starting stress triaxialities before and after localization

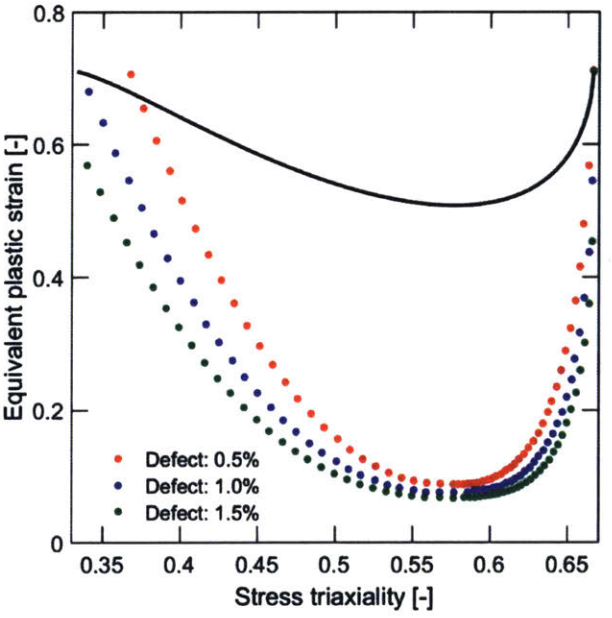

Figure 4-3. Effect of initial imperfection on localization envelope

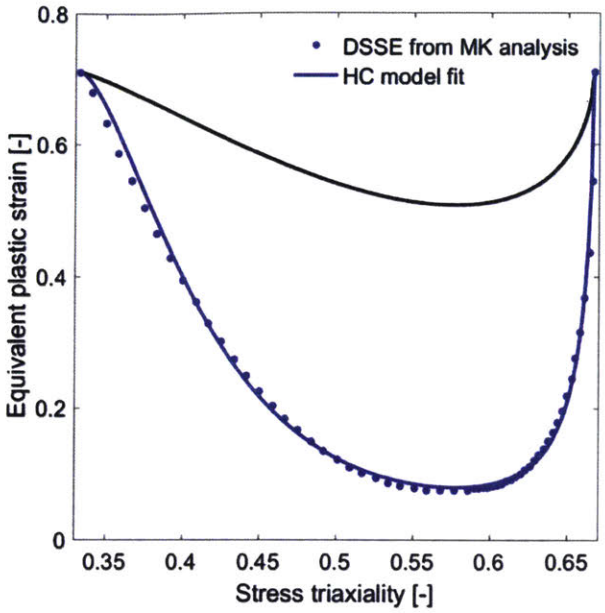

Figure 4-4. Model fit of assumed DSSE criterion (d=1.66 and p=0.01) for 1% imperfection

Given that the shape of the DSSE bears resemblance to the fracture locus, the same parametric form is used for the DSSE as with the HC model. For biaxial tension $(1/3 \le \eta \le 2/3)$ with the plane stress condition for which Eq. 2-16 holds, the HC criterion for proportional loading reads

$$\bar{\varepsilon}_{HC}^{pr}[\eta] = b(1+c)^{\frac{1}{n_f}}\left[\left\{\frac{1}{2}\left((g_1-g_2)^a + g_1^a + g_2^a\right)\right\}^{\frac{1}{a}} + cg_1\right]^{-\frac{1}{n_f}} \tag{4-10}$$

with the stress triaxiality dependent functions

$$g_1[\eta] = \frac{3}{2}\eta + \sqrt{\frac{1}{3} - \frac{3}{4}\eta^2} \quad \text{and} \quad g_2[\eta] = \frac{3}{2}\eta - \sqrt{\frac{1}{3} - \frac{3}{4}\eta^2} \tag{4-11}$$

and the fracture model parameters $\{a, b, c\}$. We then employ the function

$$\bar{\varepsilon}_{DSSE}^{pr}[\eta] = b\left[\left\{\frac{1}{2}\left((g_1-g_2)^d + g_1^d + g_2^d\right)\right\}^{\frac{1}{d}}\right]^{-\frac{1}{p}} \tag{4-12}$$

to approximate the DSSE for proportional membrane loading. For simplicity, we used $c = 0$ when reducing Eq. 4-10 to Eq. 4-12 since the friction coefficient c has only a weak effect under biaxial tension. Furthermore, it is assumed that the DSSE coincides with the HC fracture criterion at the limiting stress states of uniaxial and equi-biaxial tension. The parameter b in Eq. 4-12 is therefore the same as in Eq. 4-10. This corresponds to the MK analysis result with a thickness imperfection of about 1% (Fig. 4-3). The Hosford exponent d and the transformation exponent p are therefore the only parameters that need to be identified to fully determine the DSSE under proportional membrane loading. As demonstrated in Fig. (4-4), the DSSE for the imperfection of 1% is well approximated by Eq. 4-12 with d =1.66 and p =0.01.

Unless the DSSE is identified through the MK analysis or experiments, a transformation exponent of p =0.01 is recommended for other materials, and then the Hosford exponent d is the only DSSE model parameter that needs to be identified. It is recommended to identify d from in-plane experiments where a material undergoes plane strain tension (e.g. tension on a notched or a flat grooved specimen, see Beese et al., 2010 or Pack et al., 2012). Alternatively, it may be determined analytically through the Considère analysis (maximum force criterion) for plane strain tension when the isotropic hardening of a material $k[\bar{\varepsilon}_p]$ is already known. For a Levy-Mises material, the maximum axial engineering stress is reached when

$$k\left[\bar{\varepsilon}_{DSSE}^{PST}\right] = \frac{2}{\sqrt{3}} \frac{dk\left[\bar{\varepsilon}_{DSSE}^{PST}\right]}{d\bar{\varepsilon}_p}. \tag{4-13}$$

Plane strain tension is not accompanied by contraction in the transverse (width) direction. Therefore, there does not occur diffuse necking, and the instant of the maximum axial engineering stress (equivalently force) coincides with the onset of localized necking. The DSSE exponent d is then given by the solution to the implicit equation,

$$\left(1+2^{d-1}\right)^{\frac{1}{d}} = \sqrt{3}\left(\frac{\bar{\varepsilon}_{DSSE}^{PST}}{b}\right)^{-p}. \tag{4-14}$$

For the present DP steel, we obtain $\bar{\varepsilon}_{DSSE}^{PST}$ =0.12 after solving Eqs. 2-2 and 4-13, which is close to the MK result (Fig. 4-3).

4.1.3 DSSE for non-proportional loading

Under non-proportional loading (i,e. loading paths with varying stress triaxiality), the forming severity concept proposed by Bai and Wierzbicki (2008b) is employed to estimate the instant of onset of localized necking. For this, a necking indicator D_{DSSE} is defined with an initial value of $D_{DSSE} = 0$ in a similar fashion to the fracture indicator D_{HC},

$$dD_{DSSE} = \frac{d\bar{\varepsilon}_p}{\bar{\varepsilon}^{pr}_{DSSE}[\eta]} \quad \text{for} \quad \frac{1}{3} < \eta < \frac{2}{3}. \tag{4-15}$$

Localized necking is then assumed to occur under non-proportional membrane loading when D_{DSSE} reaches unity.

4.1.4 DSSE for combined bending and membrane loading

To be able to differentiate between necking initiation under membrane and bending loading, we integrate the experimental results of Tharrett and Stoughton (2003). Based on the results of stretch bending experiments on a steel strip with wedge-shaped punches of different radii, they postulated that a localized neck develops on the outer surface of sheets when the membrane necking criterion is fulfilled at all material points through thickness. With z denoting the thickness coordinate, the general DSSE criterion for proportional, non-proportional, membrane and bending loading is written as.

$$D_{DSSE}[z] \geq 1 \quad \forall z \in [-t/2, t/2] \tag{4-16}$$

4.2 DSSE-HC ductile failure model

4.2.1 Combined DSSE-HC ductile failure model for shell elements

The DSSE necking failure model is ultimately combined with the HC fracture model to predict failure of shell elements under arbitrary loading conditions. When failure conditions are met in first-order shell elements with a reduced integration (only one Gauss point in the plane of the shell), the stress may be either set to zero at individual thickness integration points, or the entire shell element may be deleted. In the combined DSSE-HC model, the stress at a *Single thickness Integration Point* (SIP) is set to zero if

$$D_{HC}[SIP] \geq 1 \tag{4-17}$$

while the entire element is deleted if the condition

$$D_{DSSE}[SIP] \geq 1 \tag{4-18}$$

is satisfied for *all through-thickness integration points.*

Note that to be rigorous, the latter predicts the onset of localized necking, not ductile fracture. However, recall that the size of a localized neck is at most of the order of sheet thickness. It is emphasized that for stamping or crashworthiness problems where the displacement at fracture is much larger than the sheet thickness, the displacement of fracture can be well approximated as that of localized necking. Indeed, only such large-scale problems require a shell element discretization for practical reasons such as computation time.

4.2.2 Illustration of DSSE-HC model

Figure 4-5a illustrates the combined DSSE-HC model in the space of stress triaxiality and equivalent plastic strain. The red and the green branch is descendent from the HC fracture model and the blue locus indicates a necking locus for proportional membrane loading. The red branch lies in the shear dominated loading condition ($\eta \leq 1/3$), thus predicting fracture by shear localization through Eq. 4-17 (Type I). The green line is positioned well above the necking

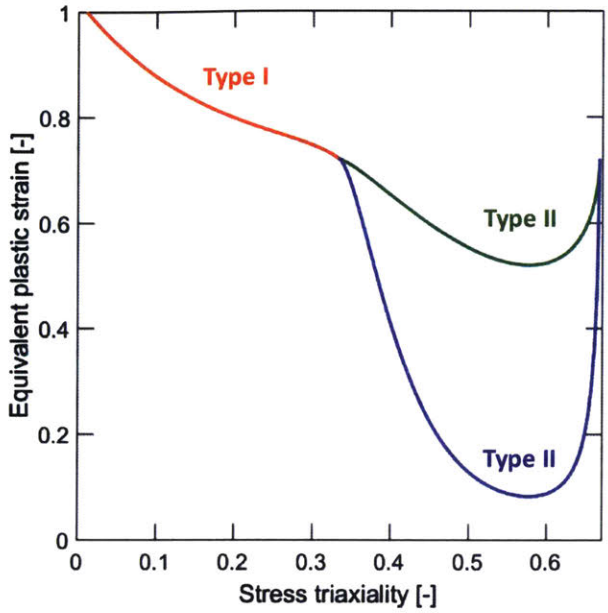

(a)

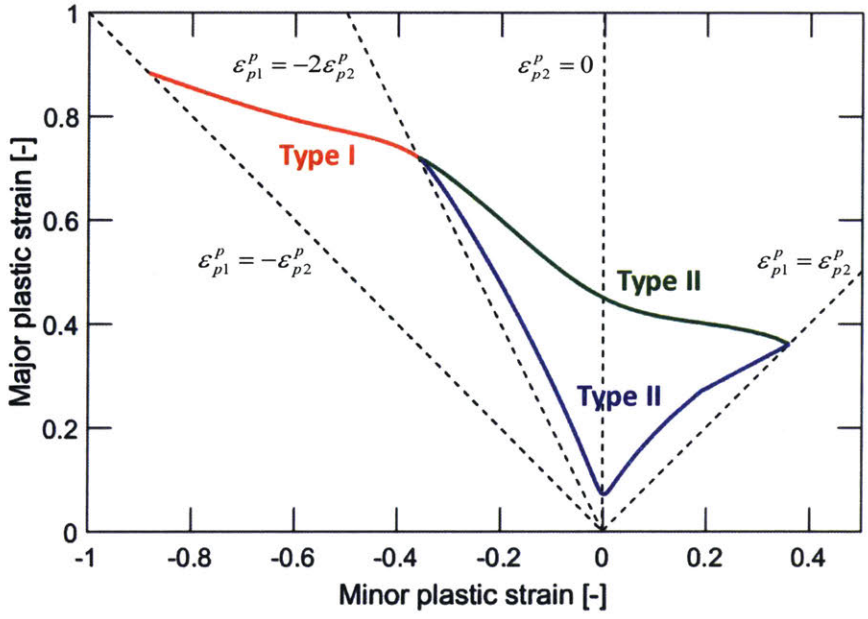

(b)

Figure 4-5. Illustration of DSSE-HC ductile failure model (a) in the space of stress triaxiality and equivalent plastic strain (b) in forming limit diagram (major versus minor plastic strain)

envelope. Thus, it is only useful when a shell element does not satisfy Eq. 4-18 for all of its integration points and is thus still alive. This is when localized necking does not take place. Therefore, the green locus takes care of biaxial fracture, *not* preceded by the formation of a localized neck (Type II). A typical example is surface cracking observed in a hemming process where a material is subjected to extremely sharp pure bending. In this case, Eq. 4-17 predicts a progressive deletion of integration points from outer to inner surfaces, which simulates through-thickness crack propagation. Lastly, the blue line together with Eq. 4-18 is used to assess biaxial fracture preceded by localized necking (Type III). Consequently, the DSSE-HC model covers all three important types of ductile fracture observed in processing sheet metal.

Using the plastic constitutive equations, we can transform the DSSE and HC criteria for proportional loading from the $(\eta, \bar{\varepsilon}_p)$ coordinate system to the forming limit diagram $(\varepsilon_{p1}^p, \varepsilon_{p2}^p)$ as depicted in Fig. 4-5b (e.g. Lee, 2005). In the principal coordinate system with $\sigma_{p3} = 0$, the stress triaxility may be written as

$$\eta = \frac{\omega + 1}{3\sqrt{\omega^2 + \omega + 1}} \tag{4-19}$$

with $\omega = \sigma_{p2} / \sigma_{p1}$ denoting the stress ratio. From the associated flow rule for the von Mises yield function, the stress ratio may be expressed in terms of the ratio of plastic strain increments $\gamma = d\varepsilon_{p2}^p / d\varepsilon_{p1}^p$.

$$\omega = \frac{2\gamma + 1}{\gamma + 2}. \tag{4-20}$$

The relation between the equivalent plastic strain and the major principal strain for proportional loading reads

$$\varepsilon_{p1}^p = \frac{\sqrt{3}\bar{\varepsilon}_p}{2\sqrt{\gamma^2 + \gamma + 1}}. \tag{4-21}$$

As expected, the DSSE envelope resembles a classical FLC, while the HC criterion defines the fracture forming limit curve (FFLC). In practice, the FFLC is particularly important under shear-dominated loading conditions where the FLC cannot predict any failure. We also computed the

failure criteria for simple bi-linear loading paths to illustrate the model response to non-proportional loading through Eqs. 2-20 and 4-15. Figures 4-6a and 4-6b show the DSSE and HC envelopes after uniaxial tension loading up to 0.3. The curves for an initial loading under plane strain tension up to 0.05 are shown in Figs. 4-7a and 4-7b.

4.3 Conclusions

The Domain of Shell-to-Solid Equivalence (DSSE) is proposed as a necking criterion for arbitrary loading conditions, including proportional, non-proportional, and combined bending and tension loading. The results from a Marciniak Kuczynski type localization analysis suggest that the necking envelope for proportional membrane loading is well approximated by a mathematical form that is a descendent of the Hosford-Coulomb (HC) fracture initiation model. It is then successfully extended towards non-proportional and bending dominated loadings by integrating the forming severity concept by Bai and Wierzbicki (2008b) and the experimental findings of Tharrett and Stoughton (2003), respectively.

The DSSE model is then combined with the HC fracture model and proposed as a failure model for shell elements. Shell element solutions are valid within the DSSE, and thus the HC model can be simply applied there. When localized necking occurs according to the DSSE, the validity of shell element solutions breaks down, and thus such an element is removed by setting all of its stress components to zero. The combined DSSE-HC model conveniently deals with three different types of ductile failure of thin metal sheets.

Type 1 – Failure by shear localization in the triaxiality range of $-1/3 \le \eta \le 1/3$, which is predicted by the HC criterion.

Type 2 – Failure by biaxial loading that is not accompanied by the formation of a localized neck in the triaxiality range of $1/3 \le \eta \le 2/3$. The HC fracture model governs the failure.

Type 3 – Failure by biaxial loading that is preceded by localized necking for $1/3 \le \eta \le 2/3$. The instant of the failure is predicted by the DSSE in a non-local manner (Eq. 4-18)

Note that the proposed model for shell elements is not based on any artificial mesh-size regularization function as suggested by Walters (2014) or Andrade et al. (2016). Also is emphasized that the DSSE-HC model for shell elements contains only one more material parameter than the original HC model for solid elements, which defines the DSSE. This additional parameter is readily identified from the hardening law of a material. Lastly, shell elements inherit all plasticity and fracture model parameters for solid elements. In other words, shell and solid elements share the material model parameters, and the entire constitutive law is not a function of a type of elements that is chosen for finite element simulation.

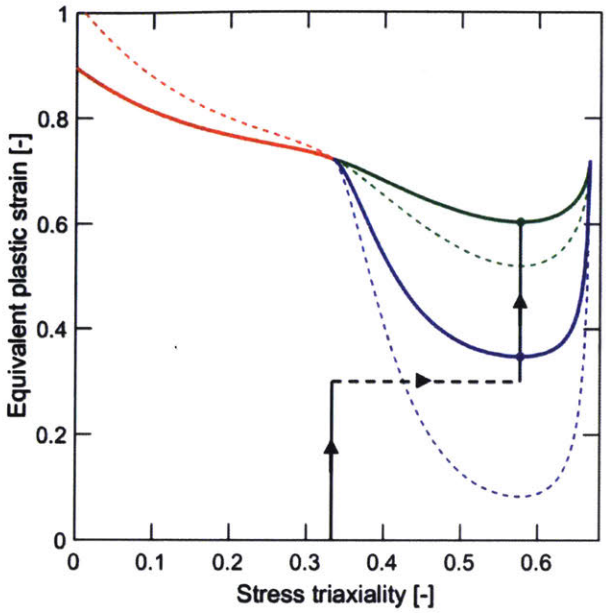

(a)

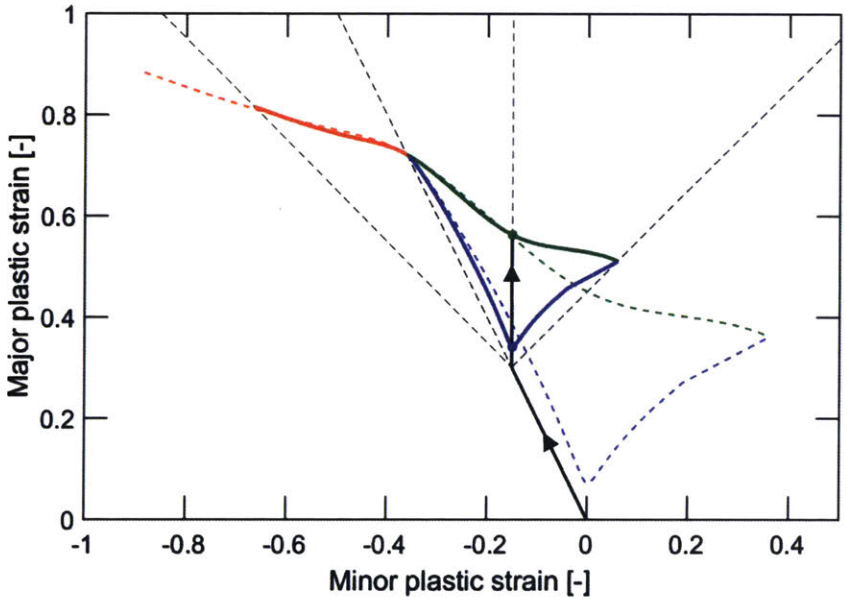

(b)

Figure 4-6. Illustration of DSSE-HC ductile failure model after uniaxial tension up to 0.3 (a) in the space of stress triaxiality and equivalent plastic strain (b) in forming limit diagram

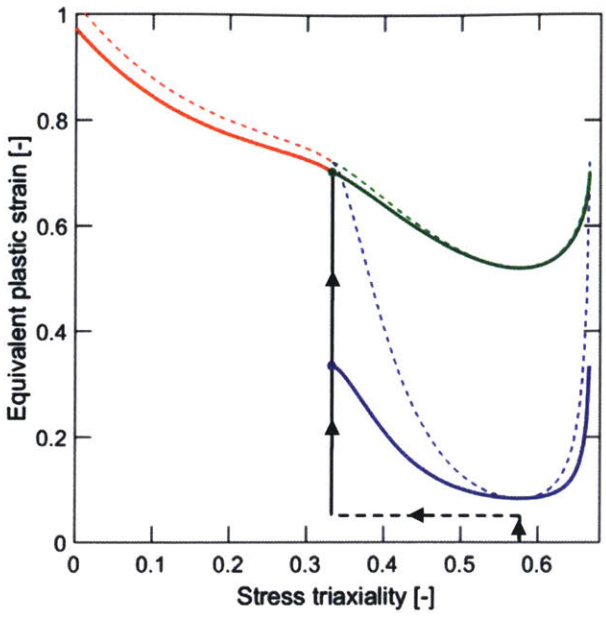

(a)

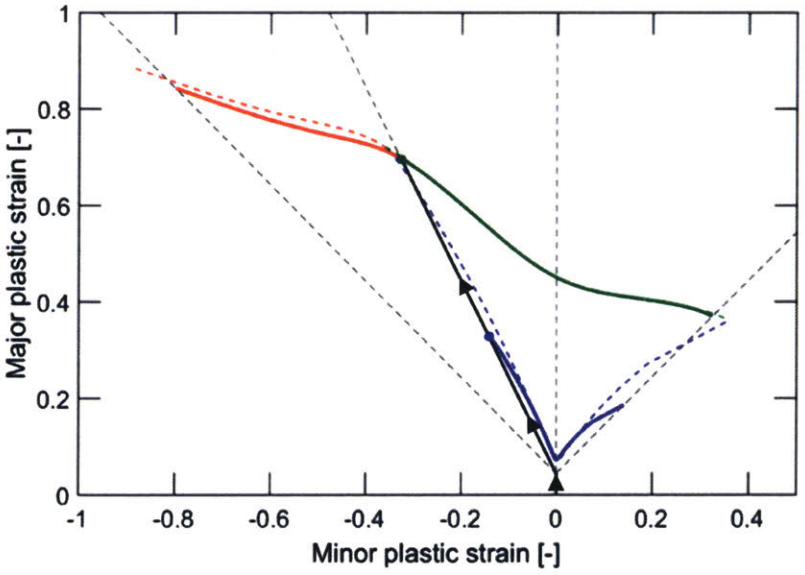

(b)

Figure 4-7. Illustration of DSSE-HC ductile failure model after plane strain tension up to 0.05 (a) in the space of stress triaxiality and equivalent plastic strain (b) in forming limit diagram

Chapter 5

Numerical performance evaluation of DSSE-HC model

In this chapter, the combined DSSE-HC model is validated on two notched tension experiments (NT80 and NT27) and three examples subjected to a different severity of bending: equi-biaxial punching (mild), pure bending followed by tension (moderate), and V-bending (severe). The DSSE-HC model is implemented to a commercial finite element code Abaqus/Explicit through a user material subroutine VUMAT. Shell element solutions are compared to very fine solid element solutions that are assumed to be exact. The material properties of 1 *mm* DP780 steel are used. The principal quantity of evaluation is the displacement at fracture.

5.1 Notched tension

The notched tension experiments on the NT80 and NT27 specimens analyzed in Chapter 3 are revisited to validate the combined DSSE-HC model for membrane-dominated loading. Figure 5-1 shows the force-displacement curve until the first element failure is predicted. In these examples, the DSSE governs the element deletion because localized necking clearly precedes fracture. For the NT80 specimen (Fig. 5-1a), the introduction of the DSSE reduced the errors in the estimated displacement to fracture from 16%, 36% and 72% (Fig. 3-2b) to 0.2%, 5%, and 14% for the 1 *mm*, 2 *mm*, and 4 *mm* shell meshes, respectively. Similar observations are made for the NT27 specimen (Fig. 5-1b), where the displacement error changed from 12%, 44% and 99% (without DSSE, Fig. 3-3) to 13%, 11%, and 8% for the 1 *mm*, 2 *mm*, and 4 *mm* meshes, respectively. Also note that the mesh size sensitivity (i.e. the spread in the results obtained for different meshes)

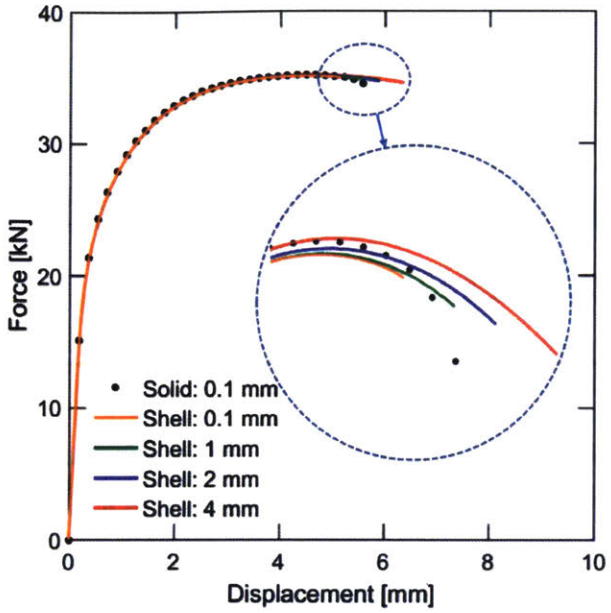

(a)

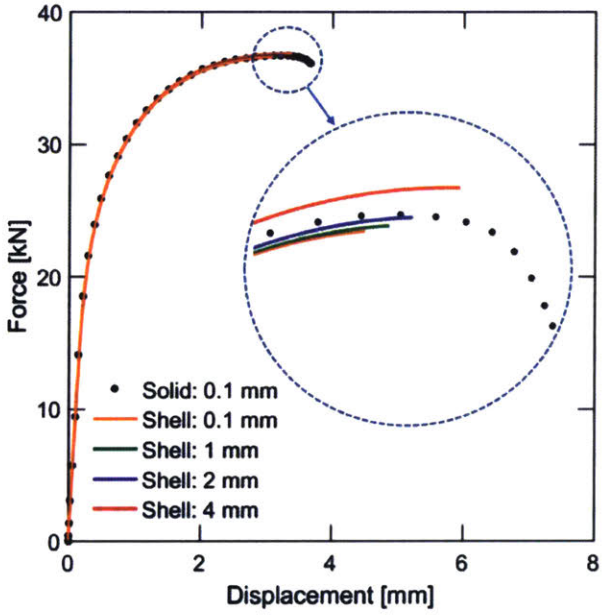

(b)

Figure 5-1. Model validation for notched tension. Force-displacement curves for (a) NT80 and (b) NT27 specimens

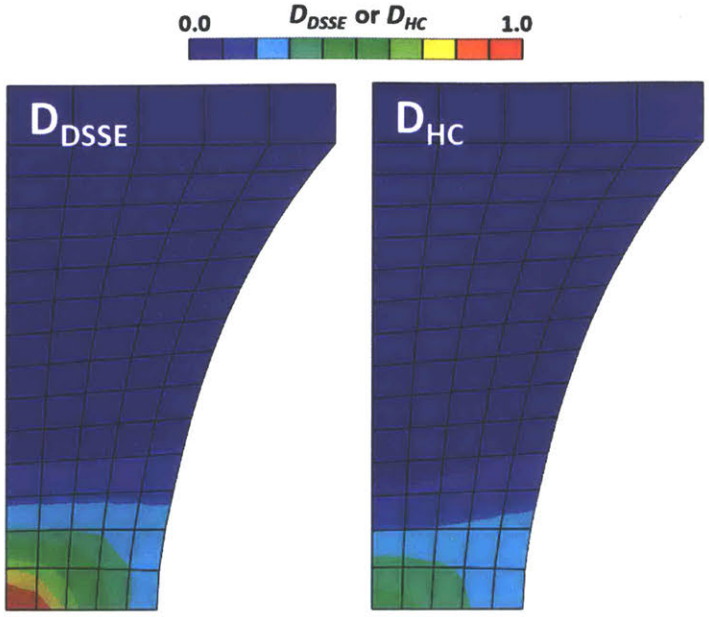

Figure 5-2. Contour plots of the necking (localization) and the fracture (damage) indicator for the 4 mm shell element model (NT80).

of the failure predictions is considerably reduced when using the DSSE. Figures 5-2 shows contour plots of the necking and fracture indicators at the instant of fracture initiation. The necking indicator D_{DSSE} first exceeds unity at the specimen center. Consequently, element deletion takes place there even though the value of the fracture indicator D_{HC} has not yet exceeded 0.5.

5.2 Hemispherical punch loading

The virtual punch experiment studied in Chapter 3 is also re-simulated with the combined DSSE-HC model. The resulting force- and strain-displacement curves are exactly the same as those shown in Fig. 3-4b. This is due to the fact that the punch specimen is free from through-thickness necking. As discussed in Hutchinson and Neale (1978), localization is impossible in absence of a geometrical defect for flow theory in Levy-Mises materials. Figure 5-3 illustrates the distribution of the necking and fracture indicators on the inner, mid, and outer shell surfaces. The mechanical fields in a punch test exhibit a small through-thickness strain gradient (in particular the stress state). It is only when $D_{DSSE} \geq 1$ for all thickness integration points that an

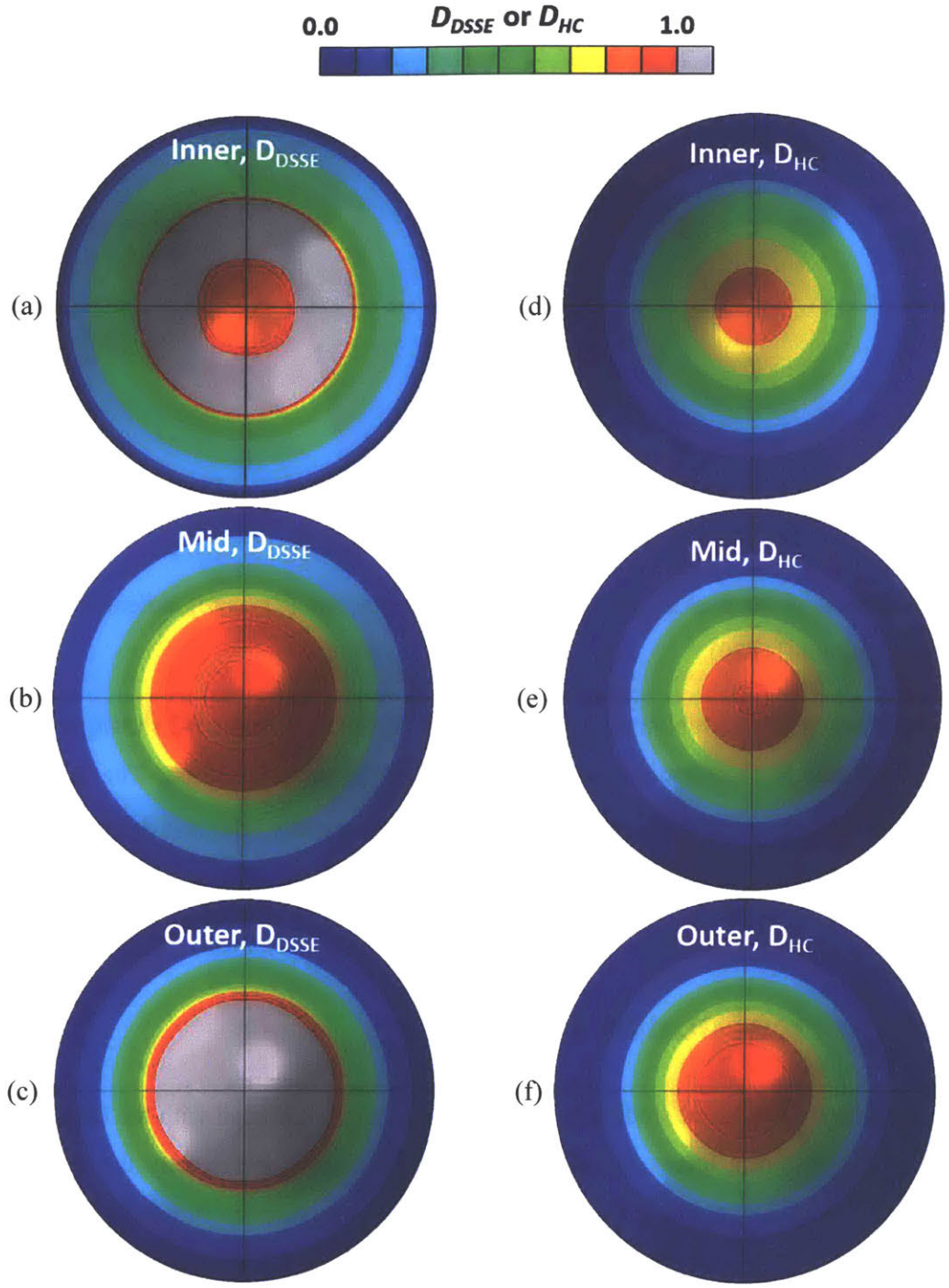

Figure 5-3. Contour plots of the necking (a, b, c) and fracture initiation indicators (d, e, f) on three different layers (inner, mid, and outer) at the onset of fracture for hemispherical punch loading.

element is deleted even though the condition $D_{DSSE} \geq 1$ is already met by integration points. However, the condition $D_{HC} \geq 1$ is met first at an integration point on the outer surface. Consequently, the full specimen failure in a virtual punch experiment is triggered by ductile fracture initiation.

5.3 Bending followed by tension on a notched strip

The next example is two-step loading on a notched strip involving moderate bending. To better demonstrate how the combined DSSE-HC model works, the industry-relevant stretch bending process (combined bending-tension) is decomposed into a two-step loading process, pure bending (Fig 5-4a) followed by tension (Fig. 5-4b). Symmetric circular notches in the stretch bending specimens (Fig. 5-5a) ensure that failure initiates from the specimen center. A quarter finite element model with 0.1 *mm* solid elements (C3D8R) is used as a baseline, and 1 *mm* shell elements (S4R) are used for the validation. Sixteen solid elements are used along the thickness direction, and five thickness integration points are considered for the shell model. The punch and the die are assumed to be rigid. The frictionless surface-to-surface penalty contact is utilized. The punch travels downwards by approximately 10 *mm*, and then tension is applied to the end of the strip with the final angle of bending kept constant.

The comparison of force-displacement curves during two loading steps between the solid and the shell mesh is provided in Figs. 5-4c and 5-4d. During the bending stage (Fig. 5-4c), the shell response agrees well with the solid element solution. Discrepancies are partially attributed to the fact that shell elements are unable to describe details of the three-dimensional deformation of the cross-section (see the inserted figure for the solid mesh in Fig. 5-4c). A few bumps on the reaction force in the latter half arise due to a discrete contact development between coarse shell element mesh (1 *mm* element size) and the 7 *mm* radius punch. After bending (and before stretching), the integration point on the outer surface indicates D_{DSSE} larger than unity (Fig. 5-5d), whereas the opposite and mid surfaces show no accumulation (Figs. 5-5b and 5-5c). Thereby, the condition for localized necking is not satisfied, and none of the shell elements fail during the bending step.

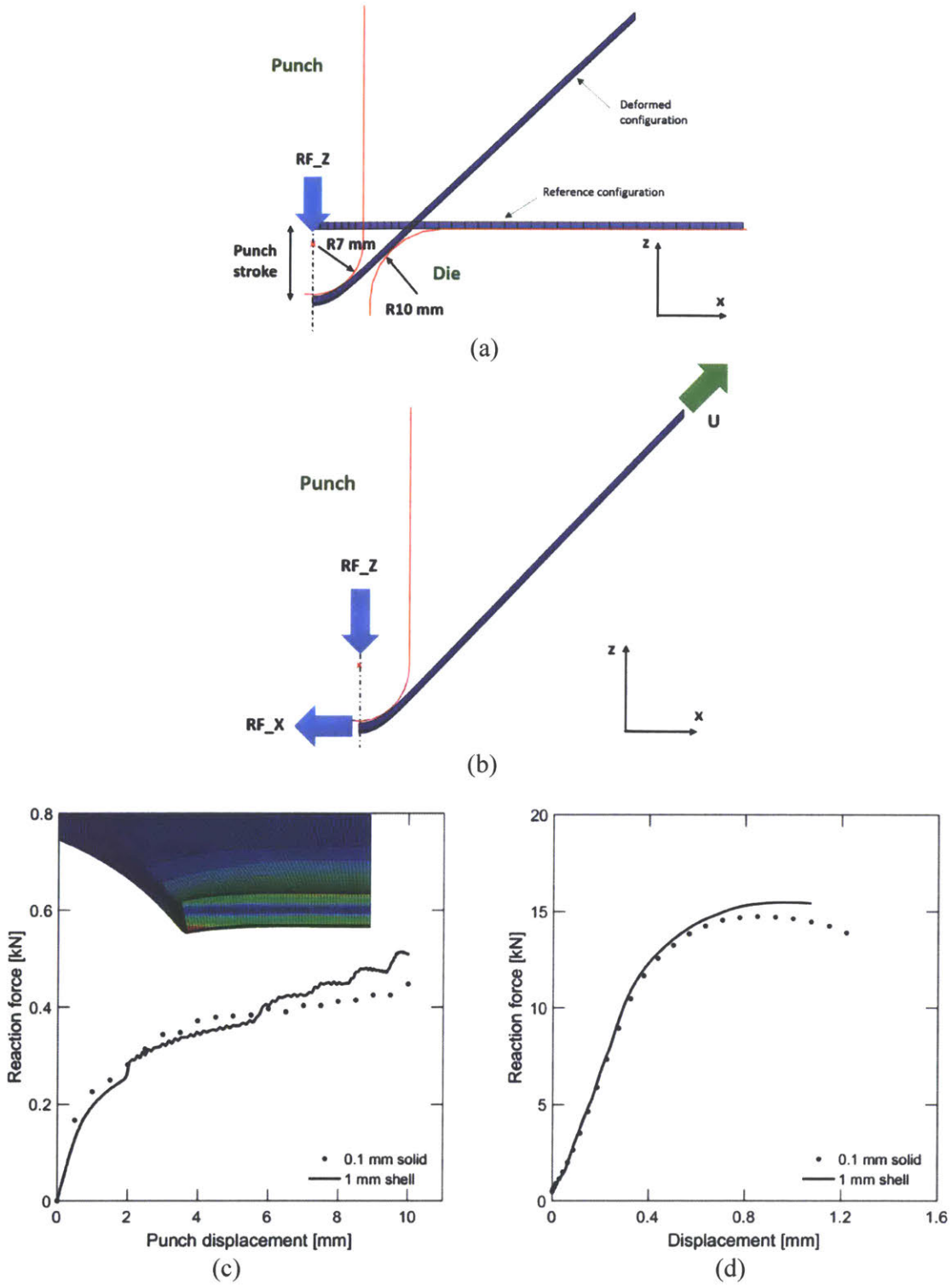

Figure 5-4. Schematics of two-step loading on a notched strip: (a) bending and (b) tension. Force (z-direction only)-displacement curves for (c) bending and for (d) tension.

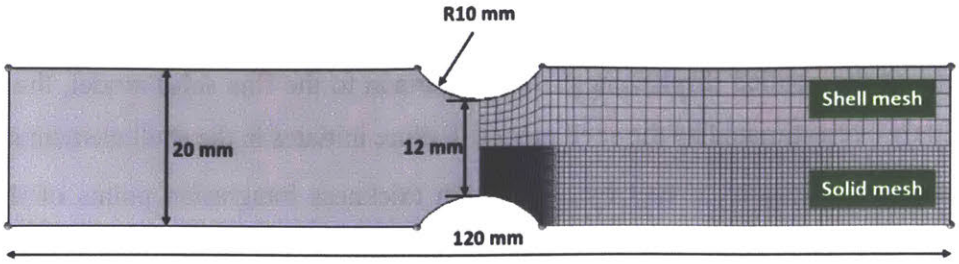

(a)

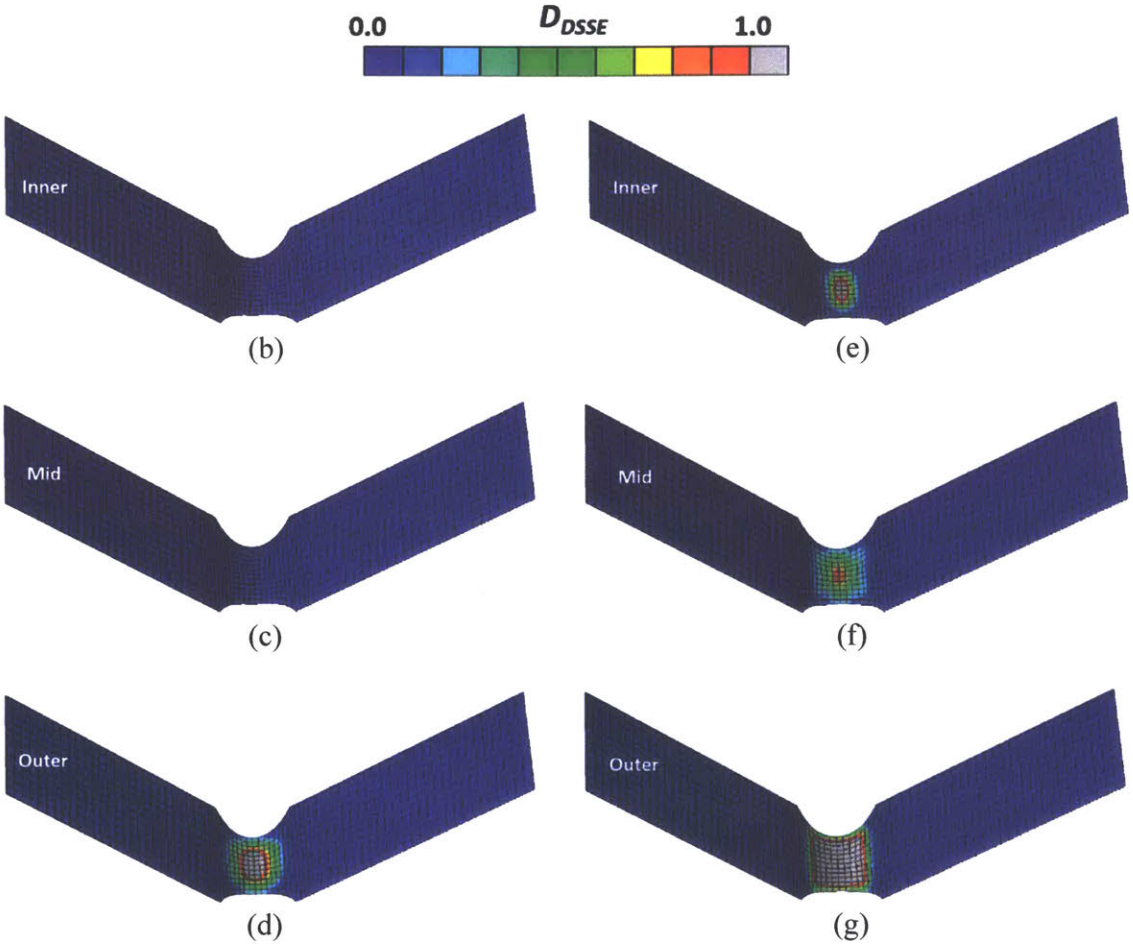

(b) (e)

(c) (f)

(d) (g)

Figure 5-5. (a) Geometry and finite element discretization of a notched strip. Contour plots of the necking indicator on three different layers (inner, mid, and outer) after bending (b, c, d) and at the end of tension (e, f, g).

Figure 5-4d shows the vertical force acting on the punch during subsequent tensile loading as a function of the applied displacement. In comparison to the fine solid model, the maximum force is slightly overestimated by the shell model. Failure initiates in the shell element simulations after the condition $D_{DSSE} \geq 1$ is met by all through thickness integration points of the element located at the specimen center. The shell model underestimates the failure displacement by about 12% which turned out to be a significant improvement as compared to using the HC model without any DSSE (where we observed an error of about 25%).

5.4 V-bending of rectangular plate

The last example is a rectangular strip subjected to plane strain bending with no membrane force by means of three-point bending with a knife edge and two big rollers. The corresponding quarter finite element model is depicted in Fig. 5-6a. A sharp semicircular punch of R0.5 *mm* is chosen to eventually generate a crack on the outer side. Deformation is expected to highly concentrate on a narrow region in the center. Accordingly, the size of elements is chosen to be 0.1 mm for both the solid (C3D8R) and the shell (S4R) mesh, which is small enough to wrap around the punch and capture a potential extreme gradient of a strain field. The entire thickness is made up by sixteen solid elements or five integration points for the shell model. The punch and the roller are modeled as an analytical rigid surface, and the frictionless contact is defined. The downward punch displacement is stopped when the failure of the first integration point is detected.

The force-displacement curves are depicted in Fig. 5-6b. In general, the shape of the curve and the level of force from the shell model show good agreement with the solid model. The displacement to fracture is underestimated by 20%, which is mostly attributed to the assumption of zero through-thickness stress components in the shell model. Figure 5-6c shows the distribution of the necking indicator D_{DSSE} on the outer and the inner surface at the onset of fracture for the shell mesh. Pure bending cumulates D_{DSSE} only on the tension side, and the compression side indicates zero value as with the bending phase of the previous example (Fig. 5-5). Hence, DSSE does not dictate the failure of shell elements in the case of V-bending. Instead,

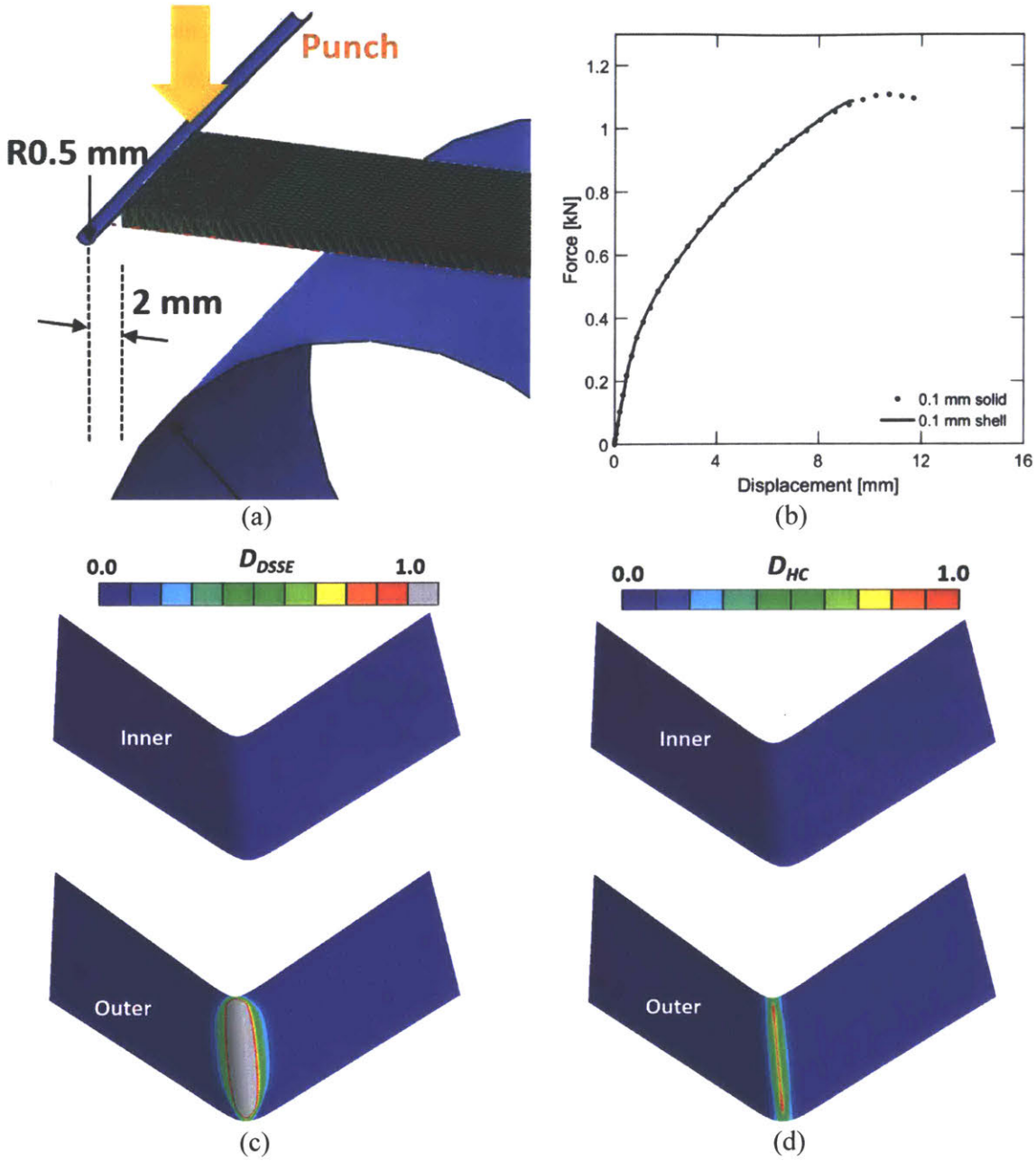

Figure 5-6. (a) Finite element model for V-bending. (b) Force-displacement curve for 0.1 *mm* solid and shell element models. Contour plots of (c) necking indicator and (d) fracture initiation indicator on the inner and outer surfaces.

the sharpness of the punch produces an extreme level of tensile strain on the outer surface, so the outermost integration point reaches the fracture limit as demonstrated in Fig. 5-6d. The corresponding integration point is removed as soon as it satisfies $D_{HC} = 1$.

5.5 Conclusions

The new failure model for shell elements that combines the Domain of Shell-to-Solid Equivalence (DSSE) and the Hosford-Coulomb (HC) fracture initiation model is calibrated for a 1 *mm* thick DP780 steel and applied to estimate the displacement to fracture in five different structural examples: notched tension with a small and large notch radius, hemispherical punch loading, bending followed by tension, and V-bending. The accuracy of shell element simulations is evaluated in terms of the displacement to fracture and the location of first element deletion, against very fine solid element models. The comprehensive numerical study demonstrates the model accuracy under a variety of loading conditions along with a noticeable reduction of mesh-size sensitivity without having to introduce a mesh-size dependent hardening law or fracture locus.

Chapter 6

Experimental validation of DSSE-HC model

In the previous chapter, the combined DSSE-HC failure model for shell finite elements was purely numerically validated by evaluating the predictability of displacement to fracture in five ductile fracture experiments, compared to very fine solid element models. The first-round validation in a virtually perfect environment was based on the assumption that solid element solutions presented by the non-porous plasticity and fracture indicator framework in Chapter 2 are exact. In addition, it was only restricted to biaxial tension conditions for which the stress triaxiality ranges from 1/3 to 2/3. It is the purpose of the current chapter to present a comprehensive experimental validation, including shear dominated loading. The experimental program includes shear, notched tension, pure bending, stretch bending, equi-biaxial punch loading, Nakazima, and deep-drawing experiments. The parameters of the constitutive models are identified with detailed procedures for numerical simulations.

6.1 Experimental procedures

6.1.1 Materials

Two important materials that are widely used in automotive engineering are considered in this experimental study.

1. The first is 0.82 *mm* thick DP980 dual phase steel. It begins to deform plastically at a stress of about 500 MPa and reaches an ultimate tensile true stress of about 1,100 MPa in

a uniaxial tension experiment. The stress-strain curves for three different material direction (rolling, diagonal, and transverse) lie approximately on top of each other (Fig. 6-1a). The corresponding Lankford ratios are $r_0 = 0.92$, $r_{45} = 0.83$, and $r_{90} = 1.04$.

2. The second material is 1.02 *mm* thick aluminum 6016-T4. Different from the above steel, the stress-strain response is direction-dependent (Fig. 6-2a). When loaded along the rolling direction, plastic yield sets in at a stress of about 120 MPa, while necking occurs at an ultimate stress of 300 MPa. The measured r-values are $r_0 = 0.69$, $r_{45} = 0.5$, and $r_{90} = 0.67$.

6.1.2 Hardening model identification experiments

Experiments are performed on small flat notched tension specimens (NT20, Fig. 6-3a) to identify the hardening law for strains in excess of the necking strain. The minimum specimen section is 10 *mm* wide, and the notch radius is R=20 *mm*. Closely following the recommendations of Dunand and Mohr (2010), the loading is applied at a constant crosshead speed of 0.5 *mm/min*. The relative displacement of the specimen shoulders is measured through digital image correlation (VIC2D, Correlated Solutions). For this, a speckle pattern is applied onto the specimen surface. The relative motion of two points positioned on the specimen axis at a distance of 15 *mm* above and below the minimum cross-section (see blue dots in Fig. 6-3a) is reported as an axial displacement. In addition, we also monitored the average strain over a distance of 2 *mm* at the specimen center. This average surface strain is referred to as "local engineering strain". It is reported as an experimental result next to the force-displacement curve in Fig. 6-1b.

6.1.3 Fracture model identification experiments

Three experiments are specifically performed to identify the stress-state dependent fracture response:

1. Simple shear experiments: A single gage section simple-shear specimen (Figs. 6-3b and 6-4a) is extracted from the sheets using wire EDM machining to characterize the

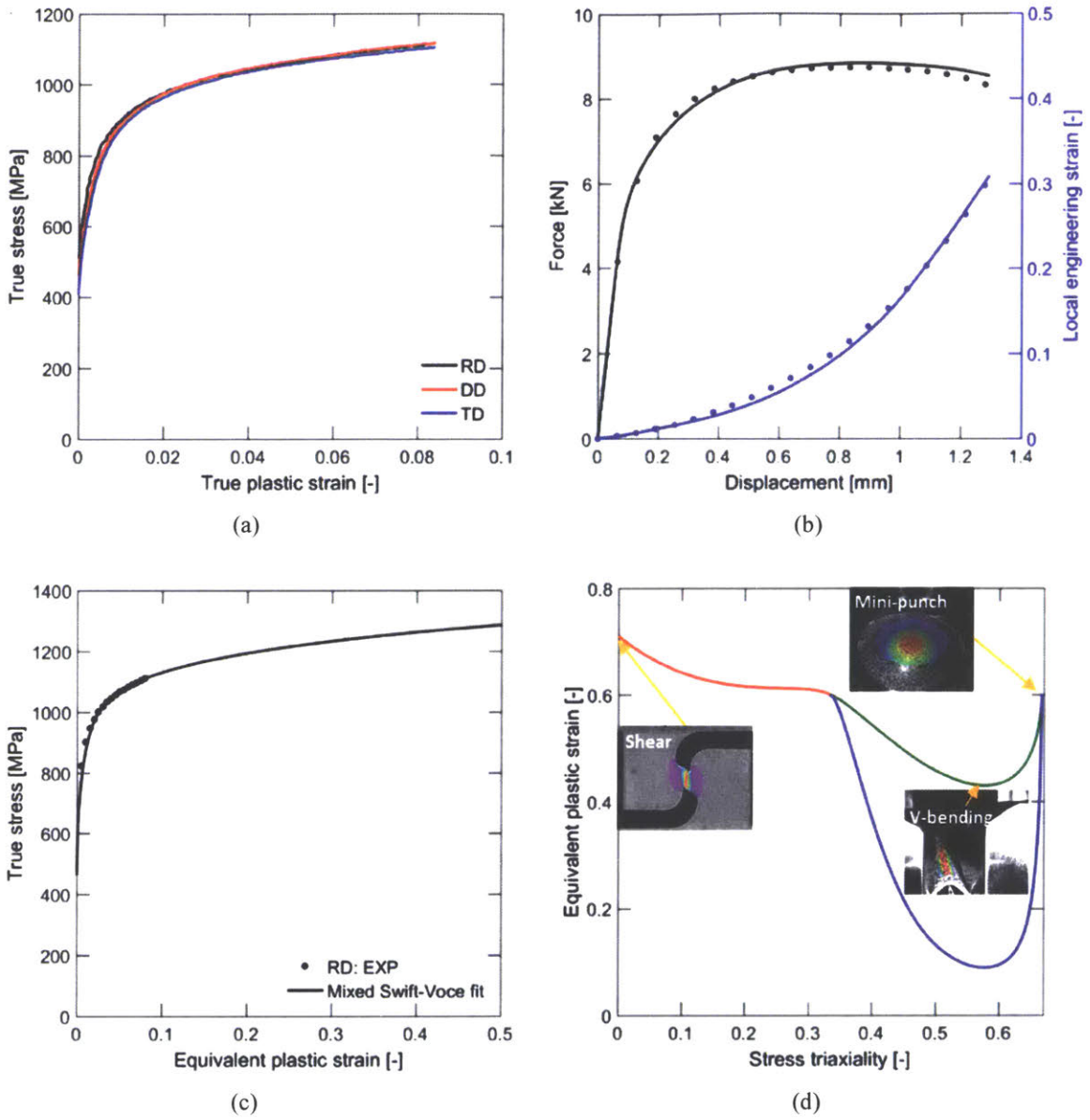

Figure 6-1. Mechanical response of 0.82 *mm* DP980 steel: (a) true stress-strain curves from uniaxial tensile tests on flat dog-bone specimens in three in-plane directions, (b) experimentally-measured (solid dots) and simulated (solid lines) force/strain-displacement curves for the small notched tension experiment (NT20), (c) identified extrapolation of the hardening curve, and (d) fracture and necking envelopes (for proportional loading) in the equivalent plastic strain versus triaxiality plane.

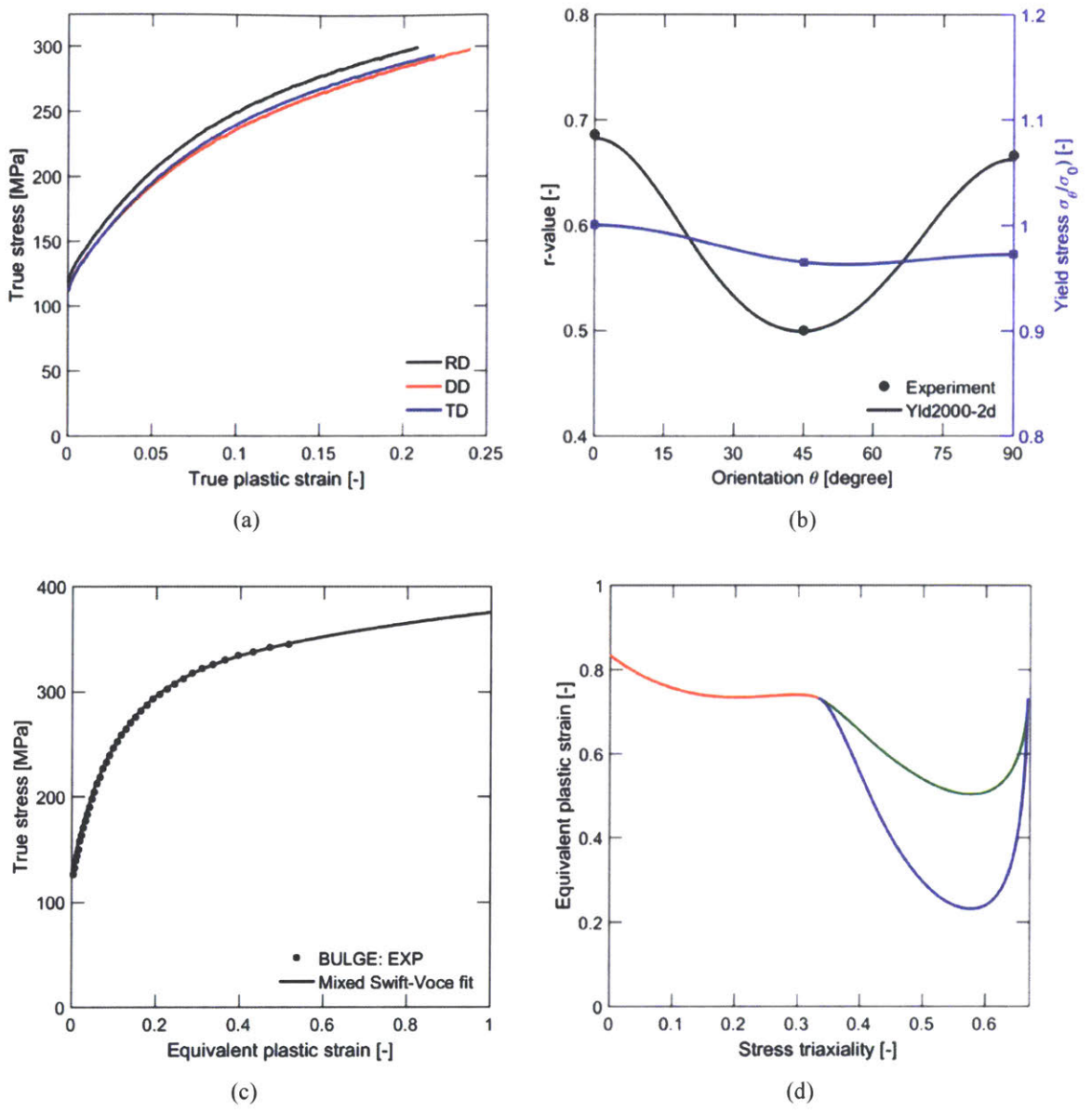

Figure 6-2. Mechanical response of 1.02 *mm* thick aluminum 6016-T4: (a) true stress-strain curves from uniaxial tensile tests in three in-plane directions, (b) direction-dependency of the r-value (black) and yield stress (blue) as observed experimentally (solid dots) and described by the identified Yld2000-2d model (solid lines), (c) extrapolation of the hardening curve after calibration based on the hydraulic bulge test, and (d) representation of the fracture locus and necking envelope in the space of the stress triaxiality and equivalent plastic strain.

fracture response at nearly zero stress triaxiality. The specimen is inserted into our testing machine using a set of high pressure clamps that prevent any relative rotation of the specimen shoulders. In the shear experiments, the relative shoulder displacement is determined from planar DIC (VIC2D, Correlated Solutions) on two points that are positioned at an initial distance of 13 *mm*. Note that the specimen gage section is only a few millimeters long. Consequently, the camera system is used in a macro mode at a resolution of 95 *pixels/mm*. The shear experiments are performed at a constant crosshead velocity of 0.5 *mm/min*.

2. V-bending experiments: V-bending experiments are performed on 20 *mm* wide plate strips (Fig. 6-3c) to characterize the fracture response under plane strain conditions. Closely following the guidelines of Roth and Mohr (2016), the specimens are loaded under three-point bending (Fig. 6-5a). The central roller (punch) is kept stationary, while the two outer rollers move downward at a constant speed of 3 *mm/min*. The stereo DIC system monitored the specimen surface of the severely strained material above the central roller at an average resolution of 86 *pixels/mm*. The displacement field is calculated using the VIC3D software with a subset size of 35 pixels and a step size of 7 pixels. The resulting surface strain field is obtained by a decay filter with a filter size of 15 points. The instant of fracture initiation is detected by the appearance of a surface crack (Fig. 6-5b) and the resulting loss of correlation.

3. Mini-punch experiments: a small disc specimen (Fig. 6-3d) is loaded using a 12.7 *mm* diameter mini-punch along with a circular 25.4 *mm* diameter die (Fig. 6-6a) to characterize the fracture response under equi-biaxial tension conditions. As with the V-bending experiments, we employed the same device as Roth and Mohr (2016) where the punch sits still on the platen and the whole fixture with a specimen moves downward at 2 *mm/s* to maintain the focal distance. The surface strain field is then monitored above the punch with the stereo DIC (same parameters as V-bending are used for VIC3D analysis) at an average resolution of 92 *pixels/mm*.

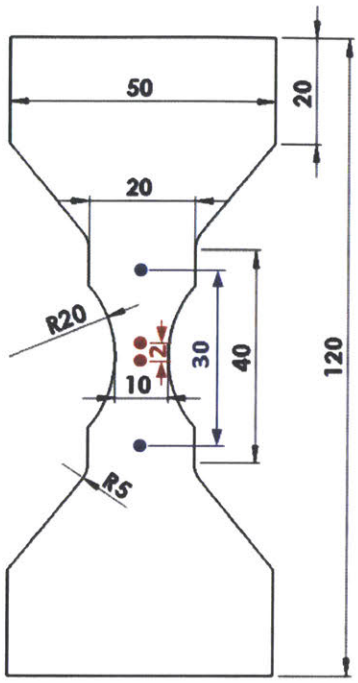

(a) NT20

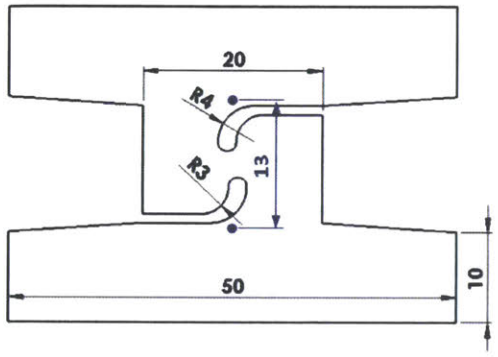

(b) SH

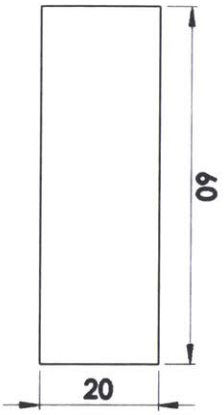

(c) VB

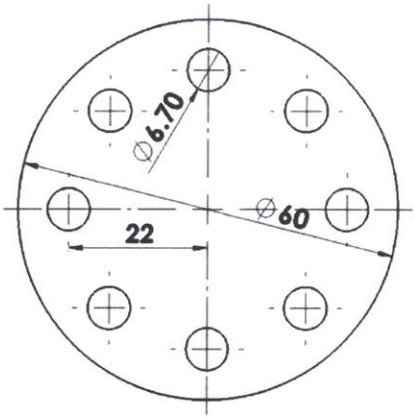

(d) PU

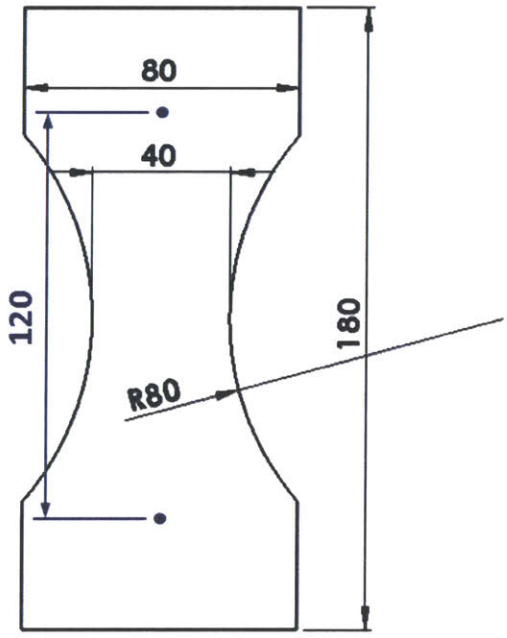

(e) NT80

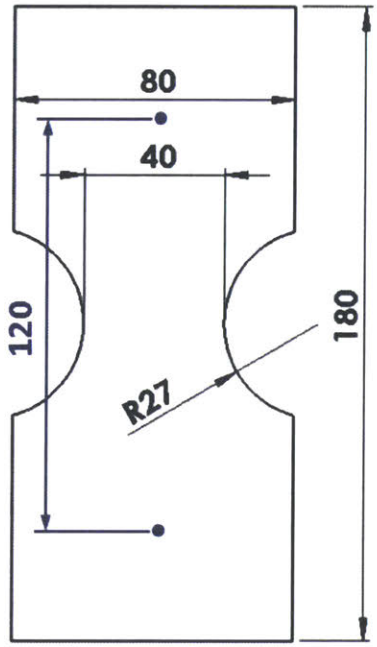

(f) NT27

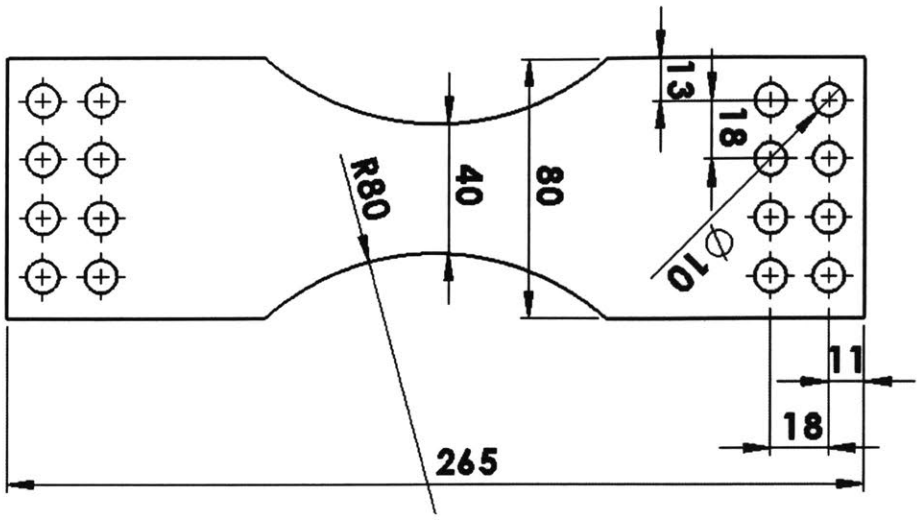

(g) SB80

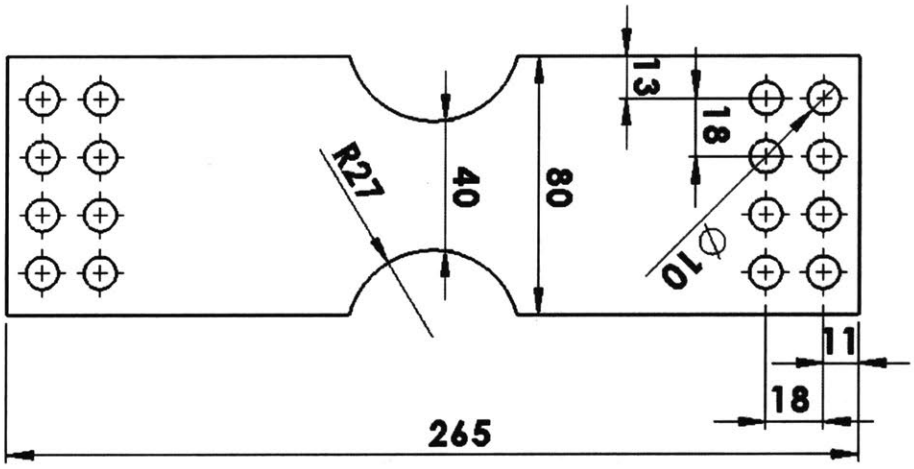

(h) SB27

Figure 6-3. Fracture specimen geometries for DP980 steel.

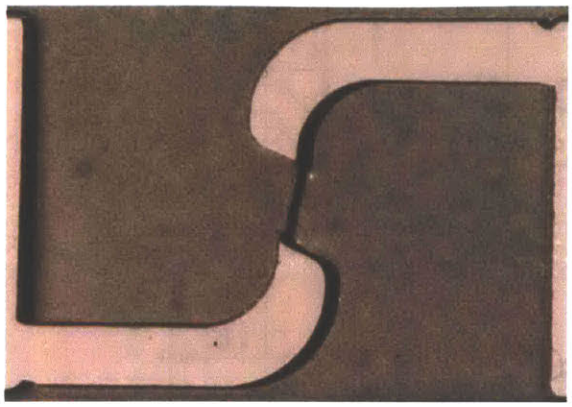

(a)

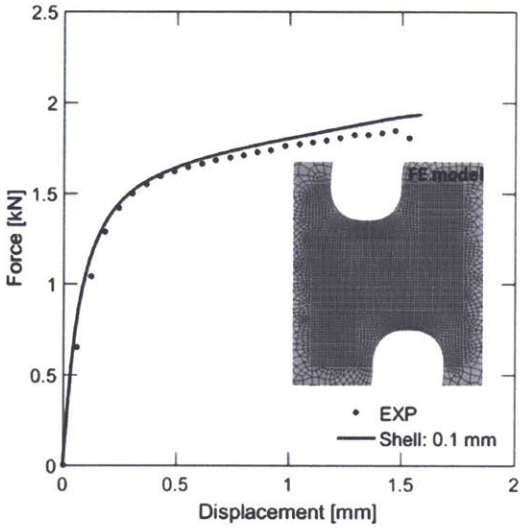

(b)

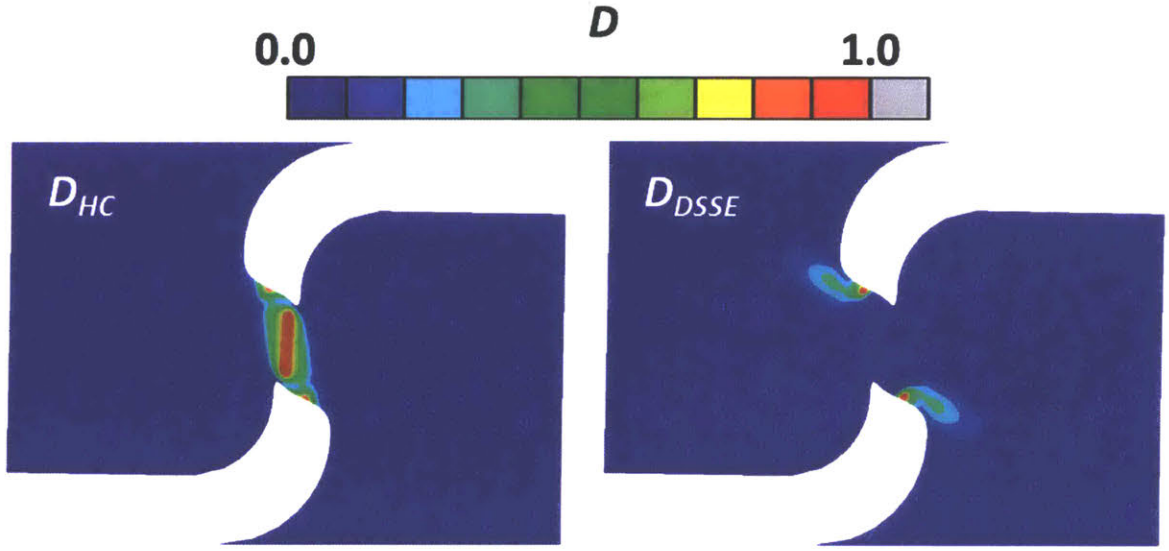

(c)

Figure 6-4. Shear (SH) experiments and simulations for DP980 steel: (a) fractured shear specimen, (b) force-displacement curves obtained from experiment (solid dots) and simulation (solid line), and (c) contour plots of necking and fracture indicators at the instant of fracture initiation.

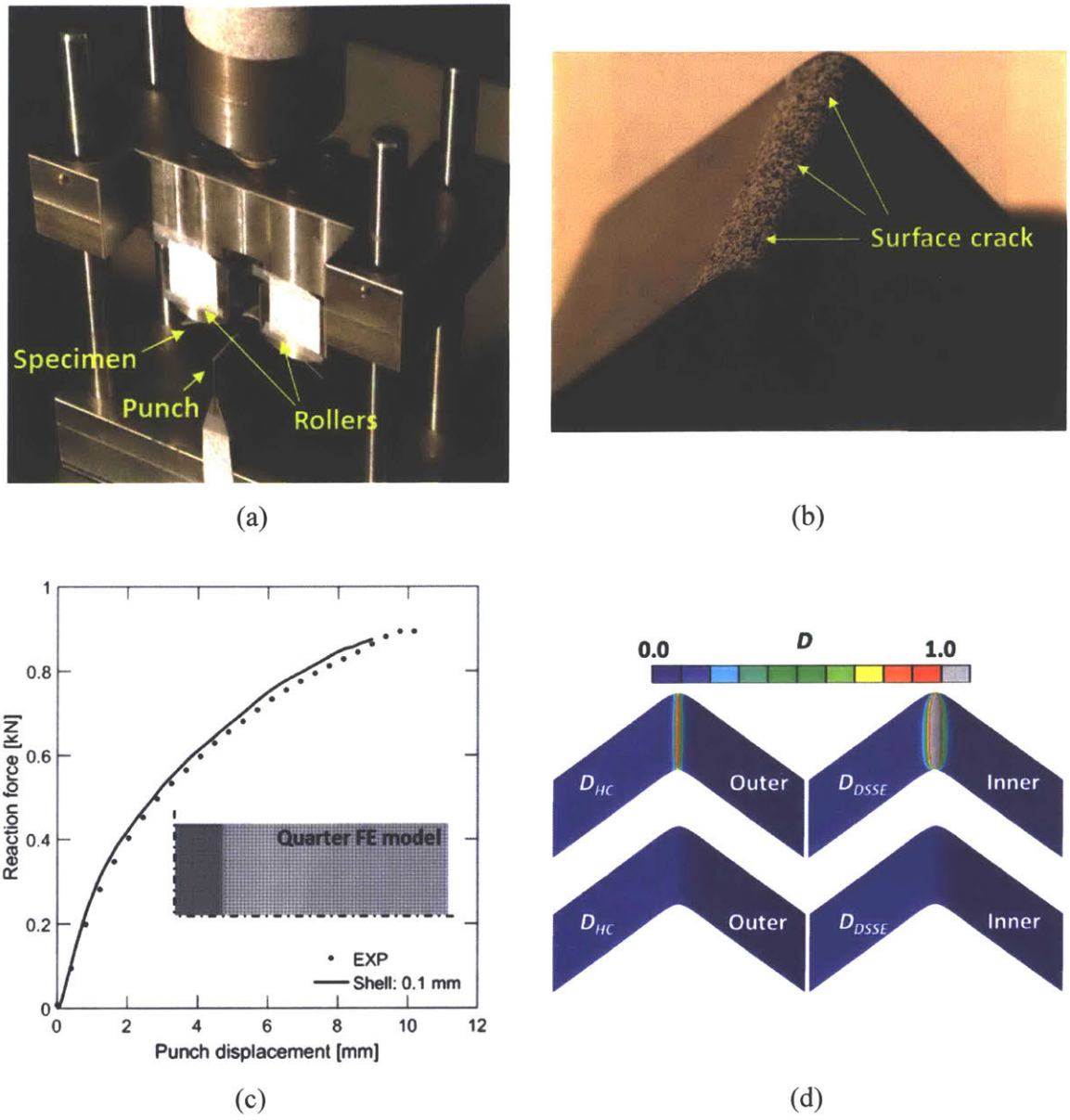

Figure 6-5. V-bending (VB) experiments and simulations for DP980 steel: (a) loading fixture, (b) straight transverse surface crack right after fracture initiation, (c) force-displacement curves from experiment (solid dots) and simulation (solid line), and (d) distribution of necking and fracture indicators on inner and outer sheet surfaces.

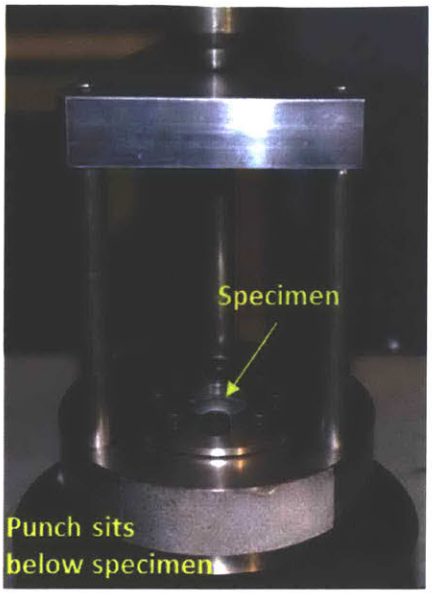

(a)

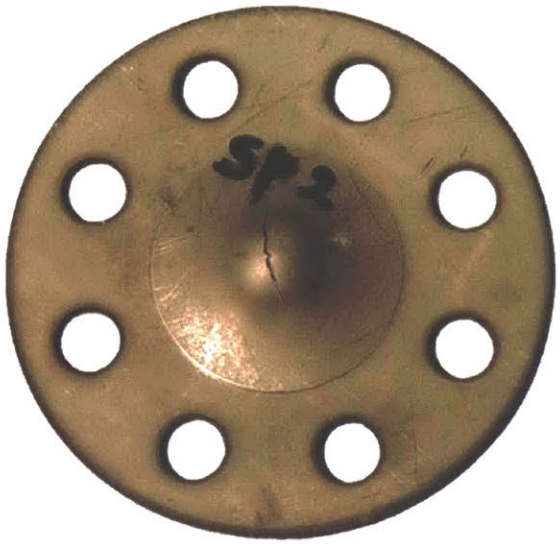

(b)

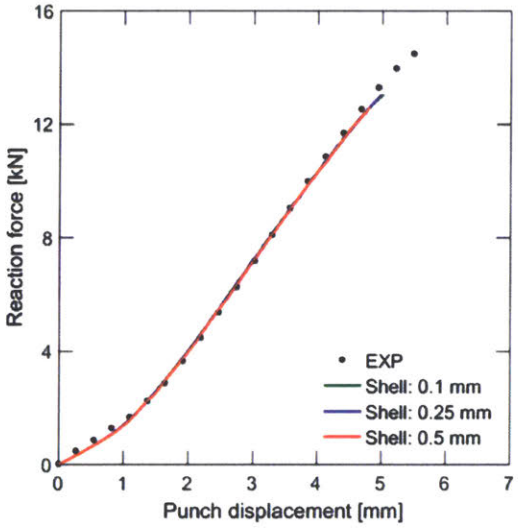

(c)

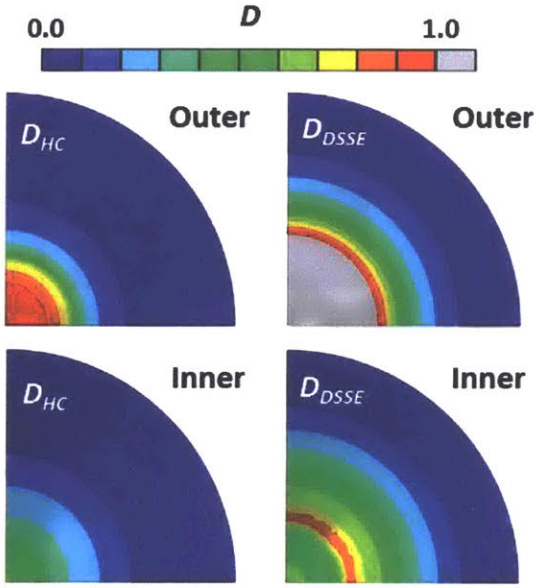

(d)

Figure 6-6. Punch (PU) experiments and simulations for DP980 steel: (a) loading fixture, (b) crack right after fracture initiation, (c) force-displacement curves from experiment (solid dots) and simulations (solid lines), and (d) distribution of necking and fracture indicators on inner and outer sheet surfaces.

6.1.4 FLC identification experiments

The Nakazima experiments are performed as per the standard ISO 12004-2. The testing setup (Figs. 6-7a and 6-7b) features a hemispherical 100 *mm* diameter punch and a 102 *mm* diameter die with a 5.5 *mm* die radius. Seven different specimen configurations are prepared in the transverse direction, following the standard (Fig. 6-7c). Each configuration is tested three times with a blank holding force of 250 kN to fully constrain the flow of flanges. Friction between the punch and specimens is minimized by an alternating sequence of three layers of hot-melt dry lubricant (ANTICORIT PL 39 SX by Fuchs) and two lubricating films (protective film 9516 RB by 3M). Punch displacement is applied at 1 *mm/s*. Strain components are calculated by three-dimensional DIC on images with a resolution of 20 *pixels/mm* at a frequency of 25 Hz.

A limit strain of each configuration at localized necking is determined by the *cross section method*: The axial and width strains along the axial direction of a specimen is approximated with an inverse parabolic function of $\varepsilon[y] = 1/(ay^2 + by + c)$. The peak value of major and minor strains from the curve fit is taken as a limit strain. The results are depicted in the Forming Limit Diagram (FLD), i.e. as a plot of the major strain as a function of the minor strain (Fig. 6-7d).

6.1.5 Tension and stretch bending experiments on large notched specimens

In view of validating our fracture model with shell elements, a second series of notched specimens with a 40 *mm* wide minimum cross-section is tested. The NT80 specimen (Fig. 6-3e) has a large notch radius of R=80 *mm* that produces only a weak notch effect. The radius-to-width ratio of the NT27 specimen (Fig. 6-3f) is only 27/40=0.67, which is the same as that of the NT6 specimen used in previous studies with solid elements (e.g. Dunand and Mohr, 2010). The same experimental procedures as for the NT20 specimen are employed at a crosshead speed of 1 *mm/min*. For both the NT80 and NT27 specimens, the reported axial displacement corresponds to the relative displacement of two points positioned at an initial distance of 120 *mm* on the specimen axis (see blue dots in Figs. 6-3e and 6-3f).

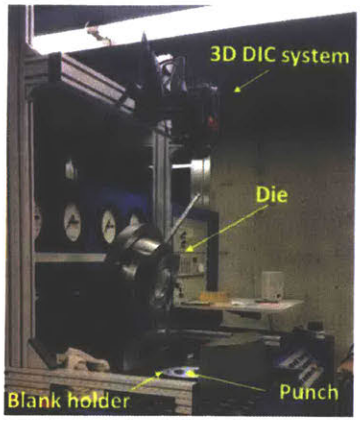

(a)

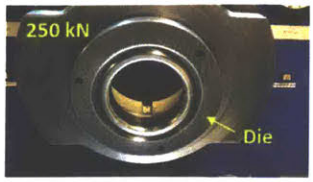

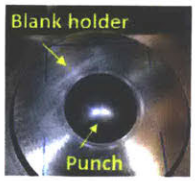

(b)

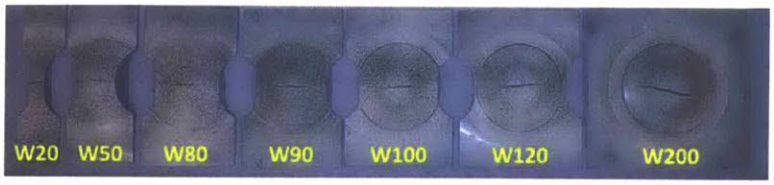

(c)

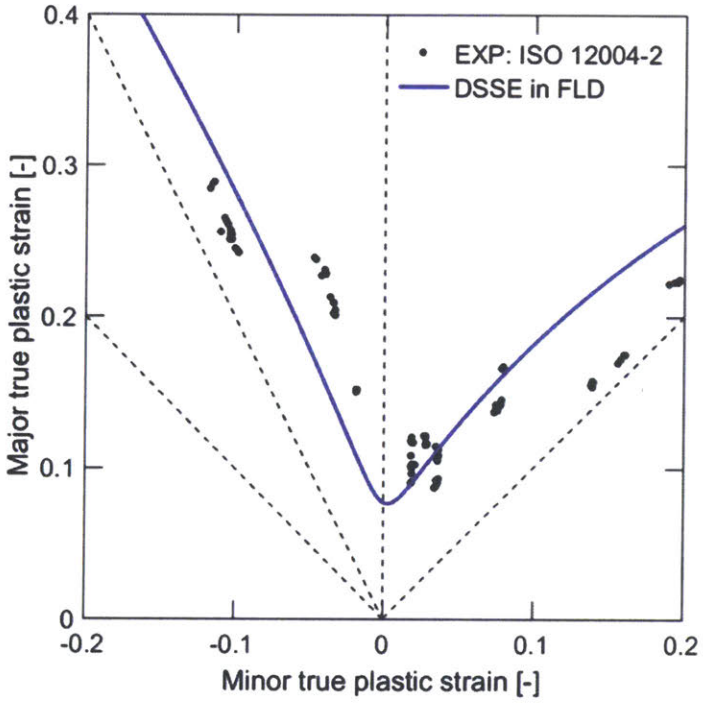

(d)

Figure 6-7. Nakazima experiments on DP980 steel: (a) testing machine with the stereo DIC system, (b) detailed views of the die, blank holder, hemispherical punch, and W50 specimen being installed, (c) failed specimens, and (d) comparison between necking envelope (blue line) and experimental data points (solid dots).

Stretch bending experiments are additionally performed on the SB80 and SB27 specimens (Fig. 6-3g and 6-3h, respectively) using a fixture shown in Fig. 6-8a. Both ends of the specimens are fixed by eight M10 screws. A crosshead velocity is applied downward at 5 *mm/min*, and a 25 mm radius cylindrical punch bends and stretches the specimens at the same time with friction minimized by three layers of Teflon and LOGIX lubricant between layers (Fig. 6-8b). The punch displacement is measured by planar DIC on speckle patterns applied to the front surface of the punch and the supports in order to eliminate the influence of a machine compliance.

6.1.6 Deep-drawing experiments

A usual setup for cup-drawing consists of a punch, a blank holder, and a die. The testing equipment for triangular cup-drawing is shown in Fig. 6-9a. A detailed geometry of the punch is provided in Gorji et al. (2016b) and that of the blank in Fig. 6-9b. The punch features a complex shape of mixed convex-concave contours with three corners of different radii, which produces a variety of non-proportional stress states. The blank holding force of 85 kN was applied, and the die radius of 3 mm with a clearance of sheet thickness was chosen. Due to the absence of a force sensor on the press and the impossibility to monitor the blank surface during loading, three blanks were tested up to three different punch displacements of 35 *mm*, 40 *mm*, and 45 *mm* to identify the instant of fracture initiation. Figure 6-9c demonstrates that the third condition developed a crack on the wall near the die radii, implying a fracture displacement lying between 40 *mm* and 45 *mm*. The surface of each blank before drawing operation was raster laser-printed to create an equidistant dot pattern (1 *mm* diameter dot and 2 *mm* gap) for ex-situ evaluation of the surface strain distribution. A formed triangular cup is photographed at more than 15 different angles with a set of scale bars. Then, the corresponding displacement and strain fields are calculated using the DIC system Argus (GOM GmbH). The obtained major strain distributions are shown in Fig. 6-13 at punch displacements of 35 *mm* and 40 *mm*.

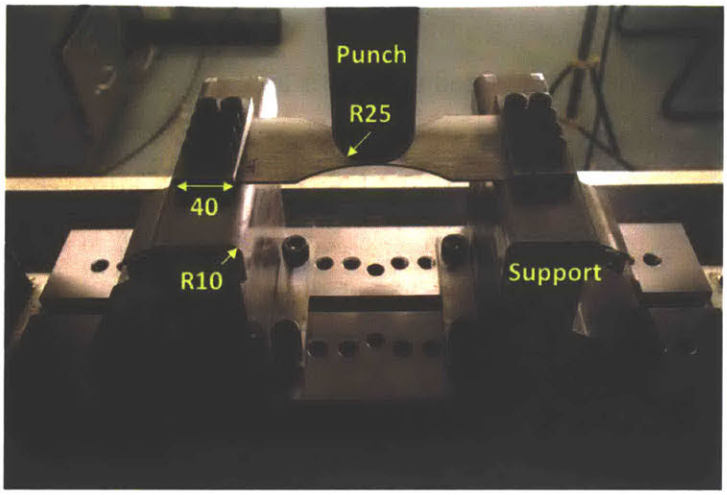

(a)

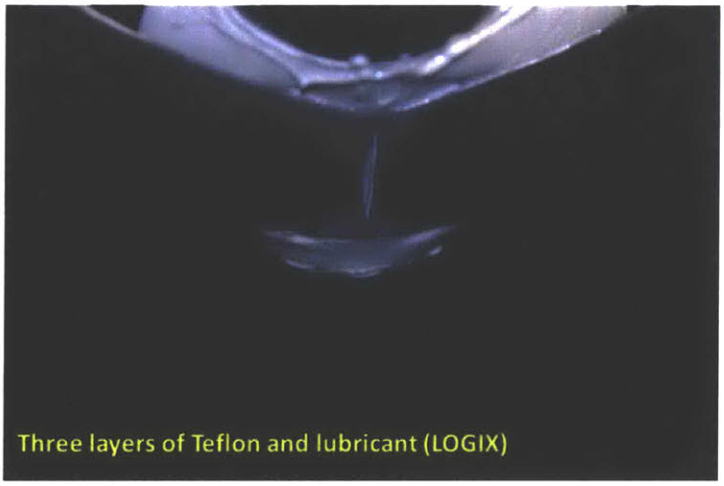

(b)

Figure 6-8. Stretch Bending (SB) experiments on notched specimens, SB27 and SB80: (a) loading fixture, and (b) close-up of a failed SB80 specimen with a straight transverse crack.

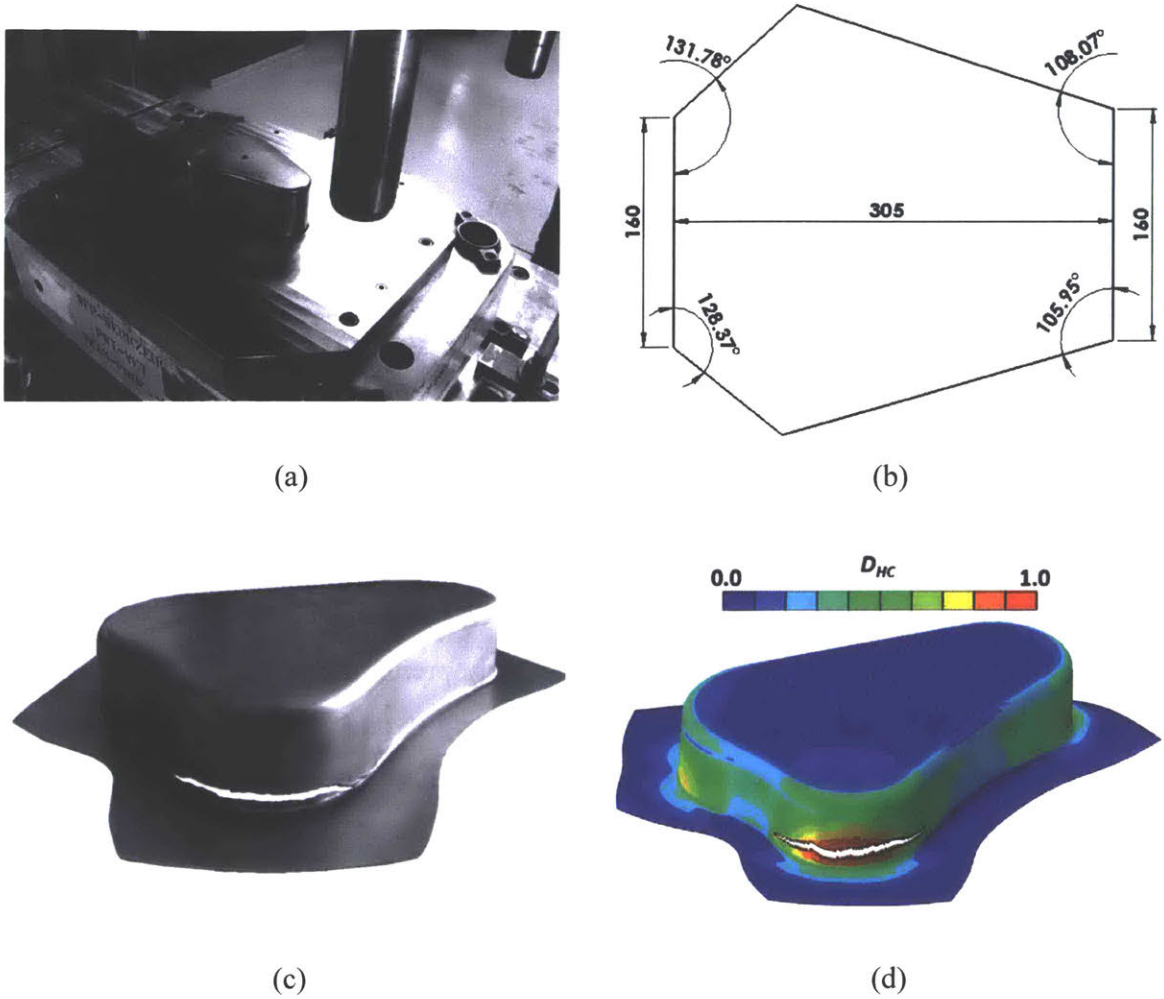

Figure 6-9. Triangular cup drawing experiments: (a) blank holder and triangular punch, (b) initial blank geometry, (c) failed specimen, and (d) crack predicted with shell element simulation (contour of fracture indicator superposed)..

6.2 Model parameter identification

6.2.1 Model parameter identification for DP980 steel

- Step I – shape of the yield surface: given the mild Lankford variations and the fact that the stress-strain curves for three different material orientations lie on top of each other, the von Mises yield function is chosen to describe the DP980 steel.
- Step II - Hardening parameters: the Swift and Voce parameters, $\{A, \varepsilon_0, n\}$ and $\{k_0, Q, \beta\}$, are identified independently from an analytical fit of the true stress versus plastic logarithmic strain curve as measured up to the point of necking ($\bar{\varepsilon}_p \cong 0.08$) in a uniaxial tension experiment. Subsequently, numerical simulations are preformed of the NT20 experiment using a very fine solid element mesh of the specimen (type C3D8R of Abaqus element library and size in the central region of about 0.1 *mm*). Using a simple derivative-free Nelder-Mead scheme (Matlab implementation), the weighting factor $\alpha = 0.58$ is identified (see Fig. 6-1b). A summary of the identified plasticity parameters is provided in Table 6-1. Figure 6-1c shows the identified extrapolation of a hardening curve beyond the necking strain.

A [MPa]	ε_0	n	k_0 [MPa]	Q [MPa]	β	α
1570	2.56E-05	0.129	548	531	92.8	0.58

Table 6-1. Hardening parameters of 0.82 mm thick DP980 steel.

- Step III – HC parameters: the fracture parameters $\{a, b, c\}$ are identified from the simple shear (SH), V-bending (VB), and punch (PU) experiments (Roth and Mohr, 2016). The fracture strains are directly extracted from the measured surface strain fields since (i) the stress state is approximately constant in all these experiments, and (ii) fracture is expected to initiate near the specimen surface. The experimental data points $(\eta, \bar{\varepsilon}_p)$ at the instant of

fracture initiation are: $(0, 0.71)$ for SH, $(0.58, 0.43)$ for VB, and $(0.67, 0.6)$ for PU. The exact (and unique) fit of the HC envelope for proportional plane stress loading yields the dimensionless parameters $a = 1.59$, $b = 0.6$ and $c = 0.046$ (see red and green solid lines in Fig. 6-1d).

Step IV – DSSE parameter: in the parametric form of the DSSE, Eq. 4-12, the exponent d is the only free material model parameter. Knowing the hardening curve (after completing Step II) makes it possible to apply the Considère criterion in Eq. 4-13. Solving the non-linear equation yields $\bar{\varepsilon}_{DSSE}^{PST} = 0.12$. A fit of the DSSE locus with a fixed transformation exponent $p = 0.01$ yields the DSSE exponent $d = 1.69$. The identified DSSE envelope is plotted next to the HC locus as a solid blue line in Fig. 6-1d. For validation purposes, we also transformed the DSSE from the $(\eta, \bar{\varepsilon}_p)-$plane to the FLD. The transformed DSSE (solid line in Fig. 6-7d) using Eqs. 6-1 to 6-3 shows a reasonable agreement with the results from the Nakazima experiments (solid dots), which is seen as a partial validation of the simple DSSE criterion.

6.2.1 Model parameter identification for aluminum 6061-T4

- Step I – shape of yield surface: the yield surface is determined based on the measured yield stresses and Lankford ratios in uniaxial tension experiments along the rolling, diagonal, and transverse directions, as well as on the results from hydraulic bulge and stack compression experiments, i.e. based on the eight measured quantities $\{\sigma_0, \sigma_{45}, \sigma_{90}, \sigma_{EB}, r_0, r_{45}, r_{90}, r_{EB}\}$ at an equivalent plastic strain of 4% (Table 6-2).

r_0	r_{45}	r_{90}	r_{EB}	σ_0 [MPa]	σ_{45} [MPa]	σ_{90} [MPa]	σ_{EB} [MPa]
0.686	0.5	0.666	1.0	189.3	182.6	184.0	186.7

Table 6-2. Lankford ratios and yield stresses of 1.02 mm thick aluminum 6016-T4 measured at 4% equivalent plastic strain.

The identified shape parameters α_i are given in Table 6-3, while the corresponding yield stress and r-value variations are plotted in Fig. 6-2b along with the calibrated Yld2000-2d model as a function of the material orientation.

α_0	α_1	α_2	α_3	α_4	α_5	α_6	α_7	α_8
8	0.947	1.017	0.961	1.032	1.021	1.013	0.967	1.153

Table 6-3. Yld2000-2d shape parameters of 1.02 mm thick aluminum 6016-T4.

- Step II – hardening response: a maximum strain of 0.55 could be reached in the bulge experiments and hence all the hardening parameters (including the weighting factor) are determined from a fit of the measured stress-strain curve in the bulge experiment (Table 6-4, Fig. 6-2c).a c
-

A [MPa]	ε_0	n	k_0 [MPa]	Q [MPa]	β	α
332.6	0.0168	0.2184	100.2	355.7	9.883	0.6613

Table 6-4. Hardening parameters of 1.02 mm thick aluminum 6016-T4.

Step III – HC parameters: the HC parameters are identified from the numerical analysis of Nakazima and circular cup-drawing experiments performed by Gorji et al. (2016a and b). For each experiment, a finite element simulation is performed up to the fracture displacement using a fine solid element mesh (in-plane edge length of 0.5 *mm* and six elements through thickness) with the Yld2000-3d model (Dunand et al., 2012). The history of the stress triaxiality, the Lode angle, and equivalent plastic strain is extracted from the most severely deformed element for each configuration. Due to the non-linear loading path, the HC parameters are then determined in an inverse manner using a Nelder-Mead algorithm (Matlab). The identified parameters are $a = 1.55$, $b = 0.73$, and $c = 0.046$ (red and green

curves in Fig. 6-2d).

- Step IV – DSSE parameter: in close analogy with the identification procedure for steel, Eq. 4-13 is solved to determine the DSSE parameter $d = 1.79$. The corresponding necking envelope for proportional loading (blue curve) is shown next to the fracture locus (red and green curves) in Fig. 6-2d.

6.3 Model validation for DP980 steel

All simulations are performed using a four-node first order shell element with reduced integration (type S4R of Abaqus/Explicit element library). The S4R shell considers finite membrane strains and accounts for thickness changes. The element features one Gauss point for numerical integration in the plane of the shell. It is used with five integration points along the thickness for numerical integration with Simpson's rule. The shortest element edge length is reported to describe the size of the elements used for meshing. In our discussion, the term "failure" is used to refer to either necking or ductile fracture.

6.3.1 In-plane loading of large notched tension specimens

Four shell element models are built using different element sizes: 0.1 *mm*, 1 *mm*, 2 *mm*, and 4 *mm*. Only a quarter of each specimen is modeled due to the symmetry of the mechanical system. The four sizes of shell elements cover a wide range of discretization from very fine to very coarse (a 4 *mm* model consists of only five elements in the width direction). Mass scaling is used to reduce computational time provided that the ratio of kinetic to internal energy remains smaller than 1%. The black solid dots in Figs. 6-10a and 6-10b represent the experimentally-measured force-displacement curves. In the experiments, the specimens fail through the formation of an unstable crack at an axial displacement of 4.4 *mm* (NT80) and 2.9 *mm* (NT27).

For illustration purposes, a first series of simulations is performed with the HC model only, i.e. without activating the DSSE necking criterion on top of the HC fracture model (see Figs. 6-10a and 10b). Irrespective of the mesh density, all numerically-predicted force-displacement curves lie on top of each other and are in good agreement with the experimental result up to the

force maximum. Beyond that point, it can be seen that the finer the mesh, the smaller the predicted displacement to fracture. For the NT80 specimen (Fig. 6-10a), the displacement at fracture is underestimated by 7.6% for the very fine mesh and overestimated by 19%, 40%, and 76%, respectively, for the 1 *mm*, 2 *mm*, and 4 *mm* models. The coarse discretization does not allow the formation of a diagonal band of localization, which leads to a rather gradual increase of strain. The error is dramatically reduced by the DSSE-HC model to 4%, 12%, and 23% for three large shell element models (Fig. 6-10c). The same trend with even more remarkable quantitative improvements (less than 10% error) is observed for the NT27 simulations (compares Figs. 6-10b and 6-10d). Note that this significant error reduction is achieved without any artificial mesh-size regularization on the hardening law or the fracture model. Figures 6-12a and 6-12b show exemplary contour plots of the fracture and necking indicators, D_{HC} and D_{DSSE}, right before the first element is deleted. Due to the absence of bending, all thickness integration points at a given in-plane location undergo exactly the same evolution of model variables. The necking indicator reaches unity in the center earlier than the fracture indicator, thus governing the failure of the specimens.

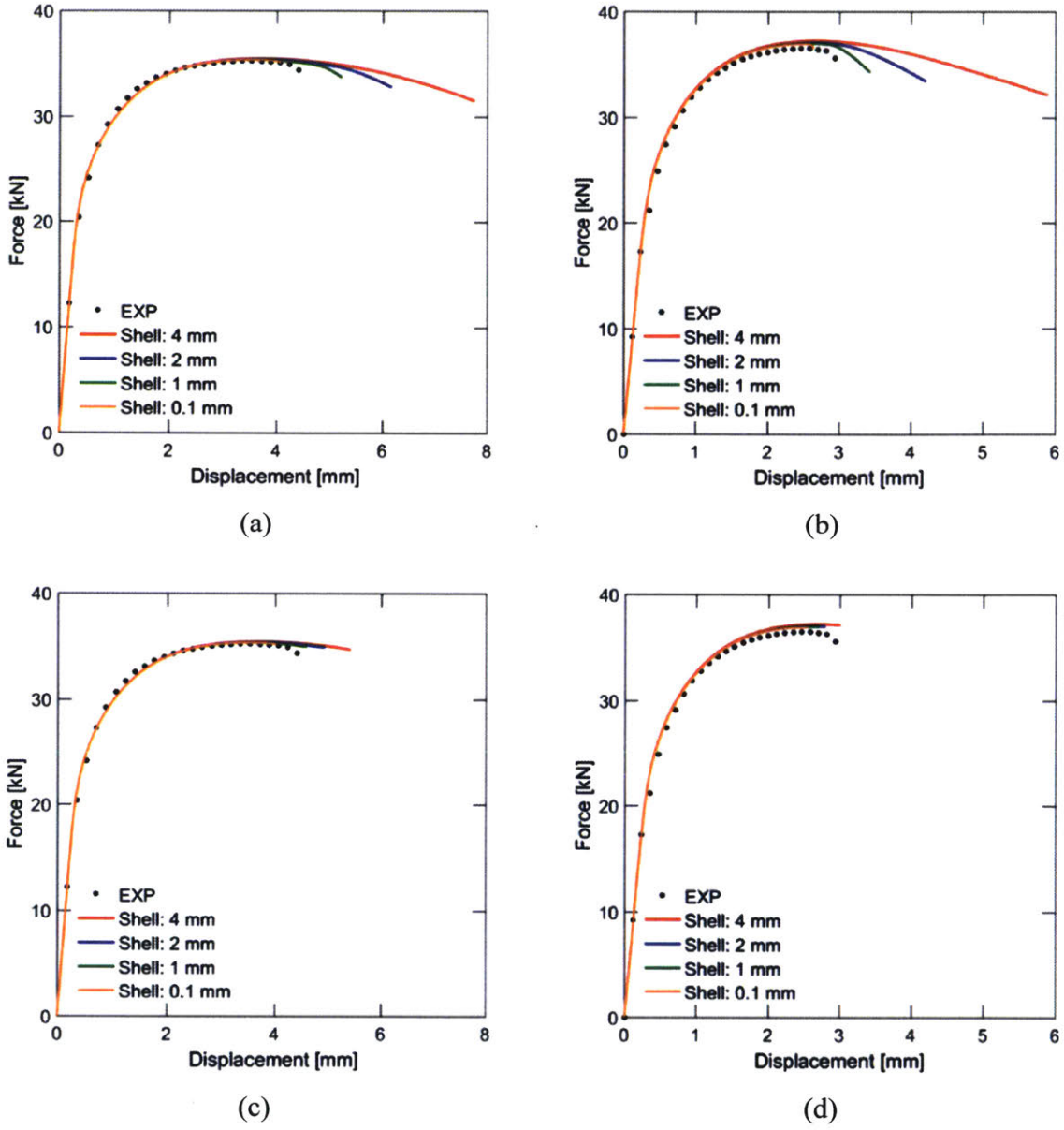

Figure 6-10. Model validation for notched tension (NT80 and NT27). The end of each solid curve corresponds to the predicted instant of failure. The results obtained with the HC model only are shown in the first row (a, b), while the second row (c, d) shows the improved predictions obtained with the combined DSSE-HC model.

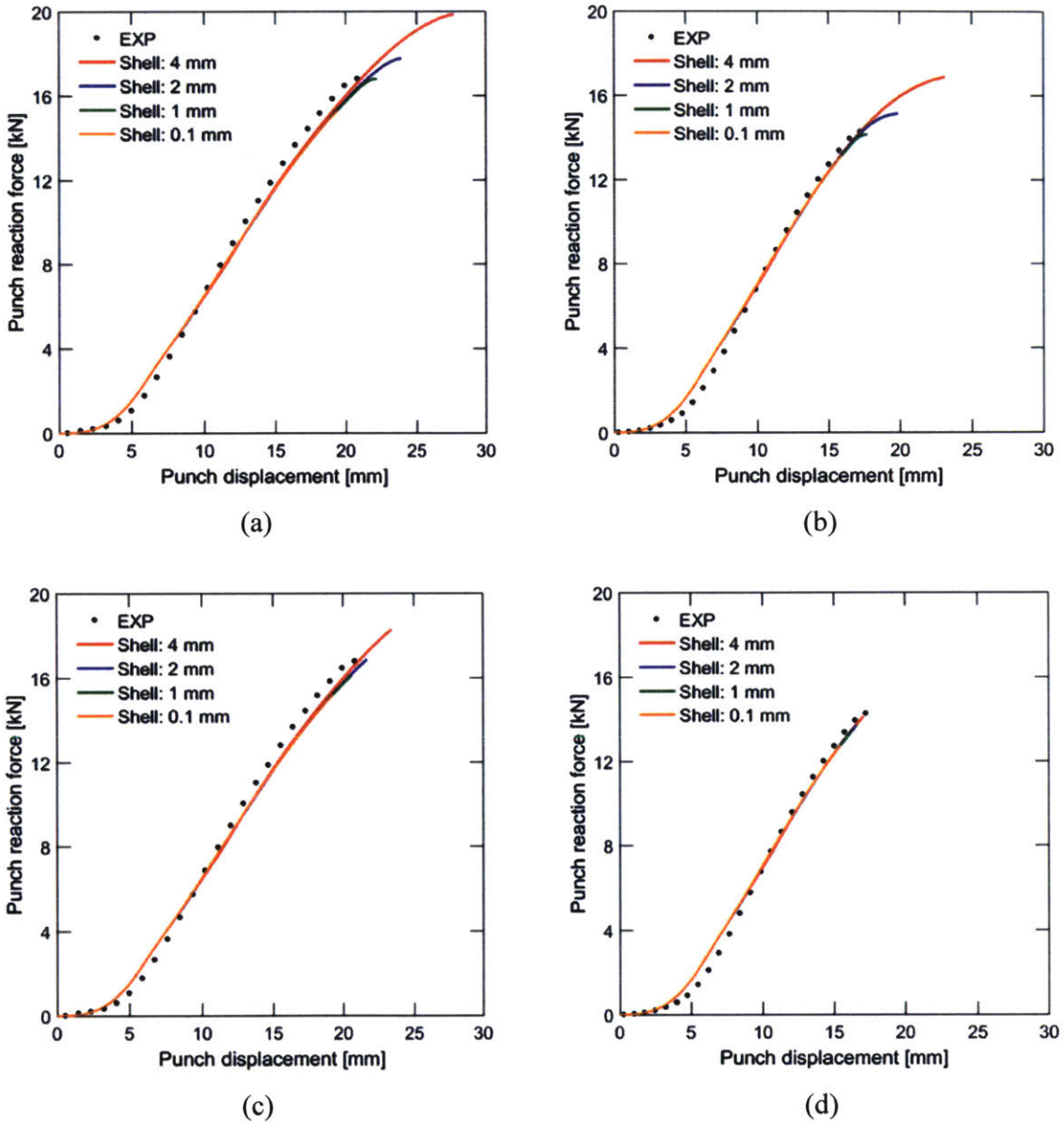

Figure 6-11. Model validation for stretch bending (SB80 and SB27). The end of each solid curve corresponds to the predicted instant of failure. The results obtained with the HC model only are shown in the first row (a, b), while the second row (c, d) shows the improved predictions obtained with the combined DSSE-HC model.

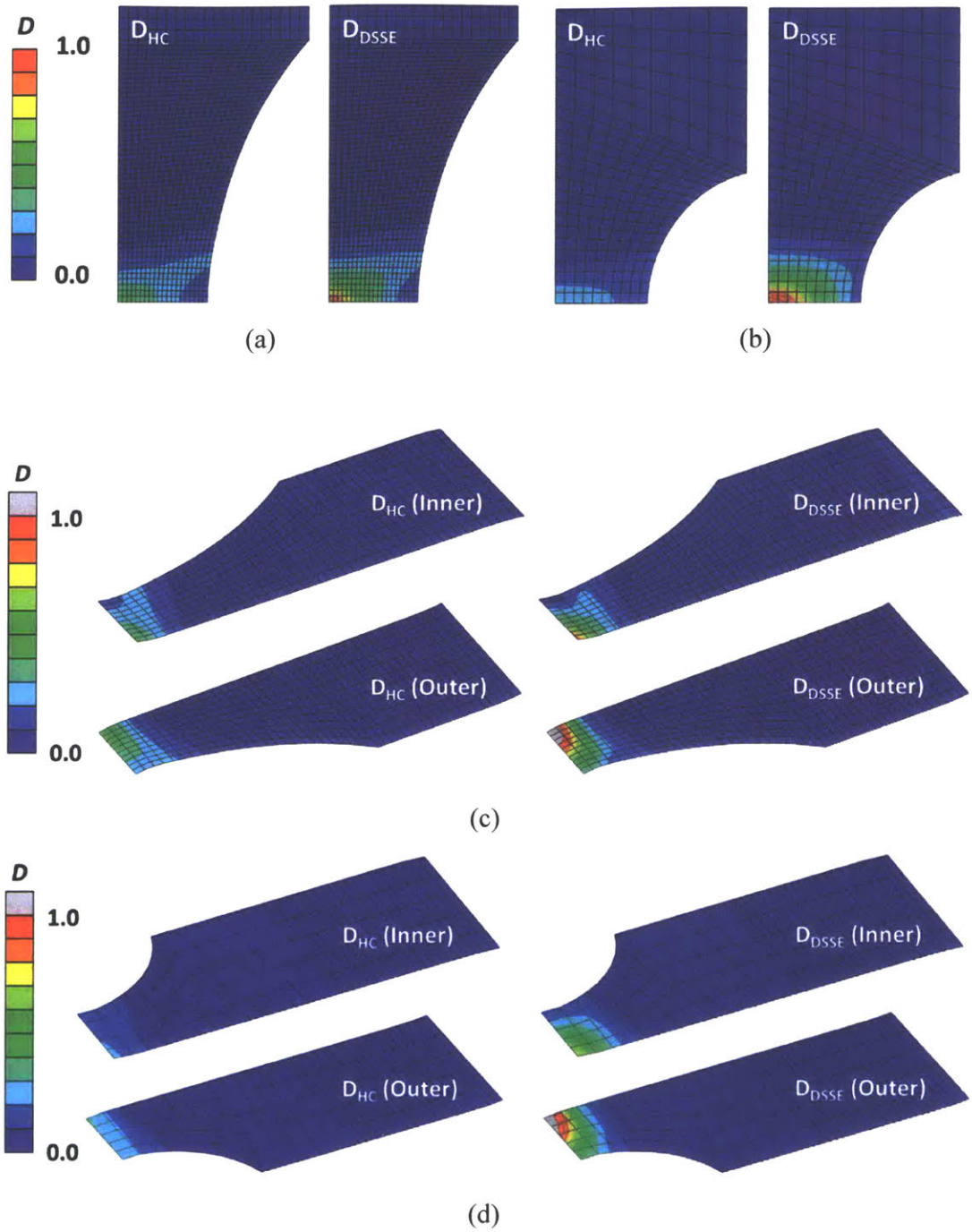

Figure 6-12. Contour plots of fracture and necking indicators at the instant of first element deletion: (a) 1 *mm* shell element model for NT80, (b) 2 *mm* shell model for NT27, (c) 2 *mm* shell model for SB80, and (d) 4 *mm* shell model for SB27.

6.3.2 Combined bending-tension I: stretch bending of large notched tension

The black dotted curves in Figs. 6-11a and 6-11b show the force-displacement curves recorded in the stretch bending experiments. The SB80 and SB27 specimens failed in an abrupt manner with a straight crack right below the punch (Fig. 6-8b). The punch displacements at the instants of specimen failure are 21 *mm* and 17 *mm* for the SB80 and SB27 specimens, respectively. We observed excellent repeatability in the experiments, and hence only one representative curve is shown per experiment type. In close analogy with the notched tension simulations, we considered shell element meshes of four different mesh densities. The end of the specimens is fixed, and the frictionless surface-to-surface penalty contact is defined between the specimen surfaces and the punch/die. The latter is modeled as an analytical rigid body.

The solid curves in Figs. 6-11a and 6-11b show the spread in the fracture displacement estimates when the DSSE is turned off. Similar to the NT simulations, we observe a decrease in fracture displacement as a function of the mesh density. The use of the HC model without DSSE overestimates the fracture displacement of SB80 and SB27 by more than 30% for the 4 *mm* shell model. When the DSSE is turned on, the maximum error is reduced to 10% (Figs. 6-11c and 6-11d). Figures 6-12c and 6-12d depict the distribution of the fracture and necking indicators right before the element in the center is deleted on both inner and outer surfaces of the SB80 and SB27 specimens, respectively. For biaxial tension (i.e. any stress-state between uniaxial and equi-biaxial tension), the necking indicator D_{DSSE} increases faster than the fracture indicator D_{HC}. This is due to the fact that the necking locus lies below the fracture locus (compare blue and green curves in Fig. 6-1d). The outer surface follows a larger radius of curvature; it is therefore subject to a higher tensile strain than the inner surface. As a consequence, the necking indicator reaches unity there first. However, it is not until the inner surface also attains $D_{DSSE} = 1$ that localized necking is said to occur (recall Eq. 20). In the case of the 4 *mm* shell model for SB27, it takes approximately 1 *mm* displacement after the outer surface satisfies $D_{DSSE} = 1$ until the inner surface also reaches $D_{DSSE} = 1$.

6.3.3 Combined bending-tension II: modeling of the mini punch experiments

A quarter of the disc specimen is discretized with shell elements. Given the small dimensions of the punch, we considered only three element sizes: 0.1 *mm*, 0.25 *mm*, and 0.5 *mm*. A larger element size would not be appropriate in view of the curvature imposed by the 12.7 *mm* diameter hemispherical punch. The outer edge is fully constrained, and the frictionless surface-to-surface penalty contact is defined between the disc and the punch that is regarded as a rigid body. As far as the elasto-plastic response before fracture is concerned, the simulated force-displacement curves agree well with the experimental result (Fig. 6-6c). For all mesh densities, we observe that the condition for localized necking is not met on the inner surface (Fig. 6-6d). Instead, the fracture indicator reaches unity on the apex of the outer surface, i.e. the model predicts correctly that there is no necking before fracture in a punch experiment. In the experiments, fracture also occurred on the top (Fig. 6-6b) at a punch displacement of 5.5 *mm*, while the numerical simulations predict failure displacements of 4.8 *mm*, 5.0 *mm*, and 5.0 *mm* for the 0.5 *mm*, 0.25 *mm*, and 0.1 *mm* meshes, respectively.

6.3.4 Pure bending: V-bending on rectangular plate

Due to the extremely small tip radius of the punch, only one simulation is performed on the V-bending specimen where we discretized the critical region with 0.1 *mm* shell elements. The surface-to-surface penalty contact with a constant friction coefficient of 0.05 is defined for the entire contact area. Figure 6-5c shows a good agreement of the predicted and measured force-displacement curves up to the point of specimen failure.

The contour plots of the necking indicator (Fig. 6-5d) demonstrate the model's ability to recognize the suppression of localized necking in a V-bending experiment. Instead of localized necking, specimen failure initiates when the fracture indicator reaches unity on the outer surface. The numerical model underestimates the displacement to fracture by 12%. In part, this error is attributed to shortcomings of the plane stress assumption, which is clearly inadequate in situations, where the local out-of-plane stress is of the same order as the in-plane stresses.

6.3.5 Simple shear experiments

The in-plane shear specimen is also of interest for model validation since it includes tensile zones near the free specimen boundaries in addition to pure shear at the specimen center. The full specimen is discretized with 0.1 *mm* shell elements. Figure 6-4b shows that the predicted force-displacement curve correlates well with the experiment with an error of 3.6% in the predicted displacement to fracture. The D_{DSSE} field (Fig. 6-4c) shows that the tensile regions are prone to necking failure. However, before reaching $D_{DSSE}=1$ at the free gage section boundaries, the HC model predicts fracture initiation under pure shear at the specimen center.

6.4 Model validation for aluminum 6016-T4

The flat blank is discretized with 1 *mm* shell elements (~80,000 elements total). The punch, the blank holder, and the die are modeled by rigid elements (R3D4 from the Abaqus element library). In the simulations, the blank holder force of 85 kN is first applied as a linear time ramp, before applying the punch displacement with a smooth time ramp to minimize noise in the initial contact development. The loading velocity is chosen such that about 20,000 time steps are performed for each millimeter of punch displacement. The surface-to-surface penalty contact is defined between the tools and the blank with a friction coefficient of 0.11. The latter is identified inversely such that the amount of the blank flow into the die cavity and the major strain distribution are captured by the simulation with good accuracy. Figure 6-13 shows the comparison of the surface strain fields as identified experimentally and numerically for punch displacements of 35 *mm* and 40 *mm*.

Fracture initiation is observed in the experiment at a punch displacement between 40 *mm* (no fracture) and 45 *mm* (fractured). The numerical simulation predicted the first element deletion at a punch displacement of 42 *mm*, which agrees well with the experimental result. We also obtain a good agreement of simulation and experiment as far as the location and path of the final crack is concerned (Figs. 6-9c and 6-9d). The element that fails first undergoes a complicated loading history. It initially travels between the blank holder and the die, where it is subjected to

compression in the hoop direction and tension in the radial direction until it passes over the die radius, which is equivalent to a pure shear stress state. Once the element enters into the die, it is continuously drawn into the die cavity while the rate of deformation in the hoop direction is close to zero. The stress state is thus close to plane strain tension.

Figure 6-14 shows the distribution of the fracture and necking indicators on the inner and outer surfaces of the formed part for the last time step before first element removal. In region A, the necking indicator of the critical element is already larger than unity on the outer surface, while the inside remains below unity; note that $D_{DSSE} \neq 0$ indicates that an element has been subject to biaxial tension. The fracture indicator exceeds unity first, thereby predicting ductile fracture before localized necking. It is worth noting that there exists another highly strained region in the part (encircled region B in Fig. 6-14). This region is still safe as far as fracture initiation is concerned $(D_{HC} = 0.5)$. However, on the outer surface of the blank, it shows a narrow red contour of the necking indicator (i.e. $D_{DSSE} \geq 0.95$) in the hoop direction around the punch radius. The necking indicator is lower on the inner surface, $D_{DSSE} \cong 0.75$, but necking is expected to be imminent in region B if the punch traveled a bit further. The current example elucidates that the successful prediction of both the instant and location of crack initiation not only requires a shear fracture model, but also a necking criterion that can differentiate between bending- and membrane-dominated loading.

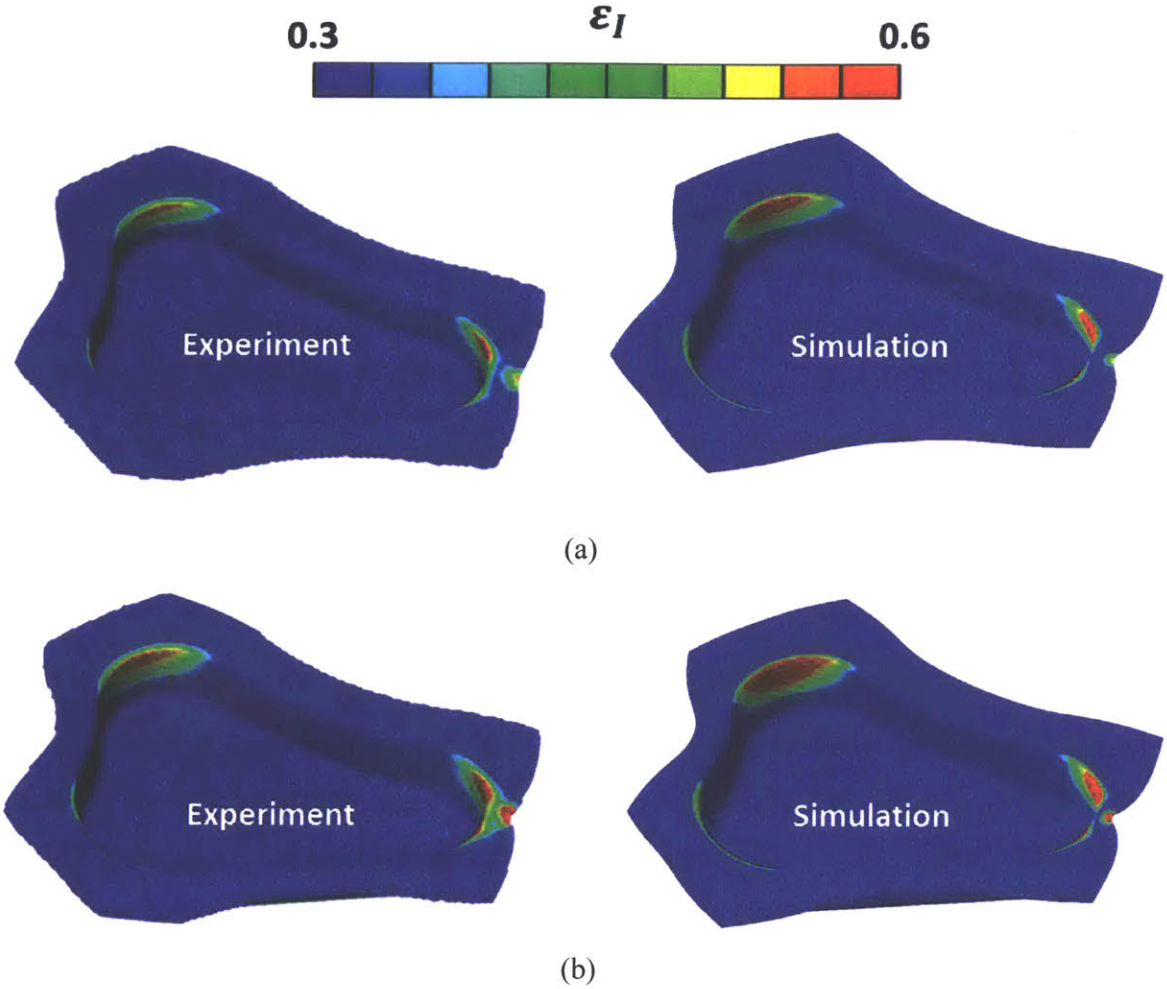

Figure 6-13. Comparison of the draw-in of a blank and the distribution of major principal strain between experiments and finite element simulations at punch displacements of (a) 35 *mm* and (b) 40 *mm*.

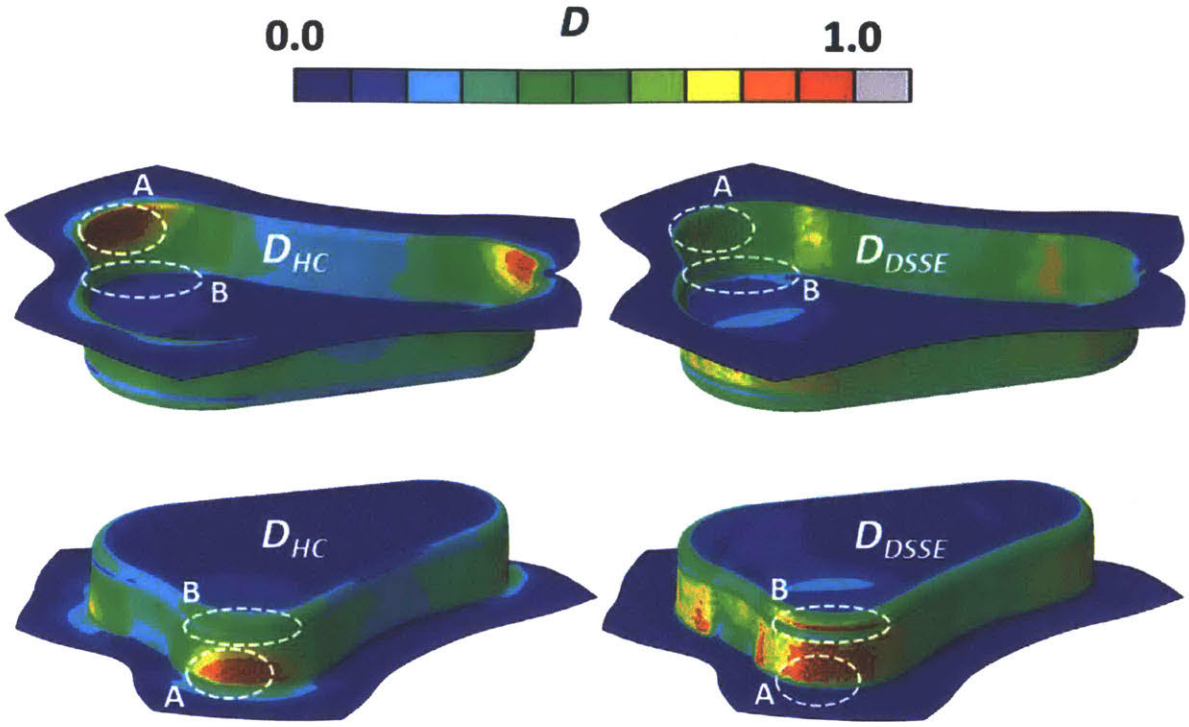

Figure 6-14. Contour plots of fracture and necking indicators on inner and outer surfaces of a deep-drawn triangular cup right before a crack appears.

6.5 Conclusions

Two metallic alloy sheets (DP980 steel and aluminum 6016-T4) that are widely used in automotive industry are chosen, and the detailed calibration of plasticity and fracture models is performed. The calibrated failure model (DSSE-HC model) is applied to shell element simulations of nine ductile fracture experiments (from coupon to deep-drawing) that cover a wide range of stress states and bending-membrane loading combinations in order to evaluate the accuracy of the DSSE-HC model. The comparison of the experimental and computational results clearly demonstrates the value of combining the DSSE and HC models to predict ductile failure with shell elements. In all validation examples, the error in the predicted displacements to failure is smaller than 10% (except few cases with very coarse discretization). It is re-emphasized that the proposed modeling approach reduces the mesh size sensitivity of the failure predictions without introducing mesh-size dependent material model parameters.

Chapter 7

Summary and conclusions

7.1 Summary and conclusions

In many engineering applications, ductile fracture occurs in thin-walled structures that are typically modeled with shell finite elements due to many practical reasons (e.g. easy meshing, computational efficiency, robust contact formulation, etc.). Although shell elements can predict the elasto-plastic response of a structure prior to fracture with great accuracy, they fail to predict the instant of ductile fracture with a wide spread of reported values. This is referred to as mesh-size sensitivity. The substantial efforts were made to eliminate the unfavorable mesh-size sensitivity and estimate a reasonable displacement to fracture at the structural level by improving the material model, limiting the attention to first-order general-purpose shell elements with a reduced integration. The emphasis was put on the consistency between solid and shell element modeling, i.e. attempts were made to maintain the material model parameters between shell and solid element models.

Non-porous plasticity with a fracture indicator framework was chosen due to its simplicity and accuracy for thin metal sheets. The exhaustive comparative study was first performed between shell and solid elements for two structural examples, large notched tension that fails by localized necking and hemispherical punching with necking delayed until fracture initiation. The detailed analysis revealed that the presence of localized necking sets the limit of the validity for shell element solutions. Furthermore, shell elements of a different size produced identical results in absence of localized necking. The constitutive assumption of the plane stress condition prevents shell elements from redistributing through-thickness strains upon localized necking, thus

underestimating the in-plane load carrying capacity. Coarse discretization hinders the formation of the in-plane localization band, which leads to the unrealistically slow rate of plastic deformation.

It was recognized as the primary task to develop a localized necking criterion for arbitrary combined tension-bending loading and define the trustworthiness of shell element solutions. It was named the Domain of Shell-to-Solid Equivalence (DSSE). The Marciniak-Kuczynski type of localization analysis was performed on a square unit-cell with the periodic boundary condition in order to identify the shape of the localization locus under proportional membrane loading conditions. The calculated curve in the space of the stress triaxiality and equivalent plastic strain showed the almost identical attribute to the Forming Limit Curve (FLC). It was further confirmed that the equation of the Hosford-Coulomb (HC) fracture model with the triaxiality sensitivity turned off fits the necking locus with great accuracy, thus suggested as a parametric form to define the DSSE. Subsequently, the forming severity concept of Bai and Wierzbicki (2008b) was borrowed to predict the onset of localized necking for non-proportional loading conditions with varying stress triaxialities. The findings of Tharrett and Stoughton (2003) and Stoughton and Yoon (2011) were integrated to account for a possible retardation or even suppression of localized necking due to bending. Localized necking is said to occur only when all material points (equivalently all through-thickness integration points of a shell element) indicate the value of the necking indicator larger than unity. In another words, the DSSE model evaluates the status of a shell element as a whole, being a non-local criterion.

Shell element solutions are valid as long as the element resides in the DSSE. Thus, the HC criterion can be simply applied and used to predict ductile fracture that is *not* accompanied by localized necking. Once a shell element gets out of the DSSE, its prediction of strain and stress fields becomes no longer valid by not being able to consider non-zero through-thickness stresses in the constitutive law, so the element is eliminated from the rest of a finite element model. It is well known that the width of localized necking in metal sheets extends at most up to their thickness. Therefore, in most engineering applications (sheet metal forming, crashworthiness, etc.) where the displacement to fracture is of interest at a length scale much larger than the thickness of a shell structure, the displacement of fracture can be well approximated to that of localized necking. This combination of the DSSE and the HC criterion is named the DSSE-HC model and proposed as a ductile failure model for shell finite elements. It predicts three types of ductile failure observed in

sheet metals: (1) in-plane shear localization, (2) biaxial fracture not preceded by localized necking (aka surface cracking) and (3) biaxial fracture in consequence of localized necking. The model was implemented to Abaqus/Explicit through a user material subroutine VUMAT.

The accuracy of the DSSE-HC failure model was first evaluated purely numerically in comparison to very fine solid element models as a baseline. The model was calibrated for a 1 *mm* thick DP780 steel and successfully applied to estimate the displacement to fracture in five different structural examples: large notched tension with two different notch radii, hemispherical punch loading on a circular disk, bending followed by tension on a notched strip, and V-bending of a rectangular plate. In addition, a series of experimental validation was performed on two materials widely used in automotive industry. These are 0.82 *mm* thick DP980 steel and 1.02 *mm* thick aluminum 6016-T4. The experimental program for calibration and validation includes more than ten different specimen geometries (from coupon to deep drawing experiments), covering a wide range of stress states and bending-membrane loading combinations. The necking envelope identified from the Considère criterion (suggested as a simple calibration method) showed a great agreement with the experimentally measured FLC. The comparison of the experimental and computational results clearly demonstrates the value of combining the DSSE and HC models to predict ductile failure with shell elements. In all validation examples, the error in the predicted displacements to failure was smaller than 10% (except few cases with very coarse discretization). It is emphasized that the proposed modeling approach reduces the mesh size sensitivity of the failure predictions without introducing mesh-size dependent material model parameters.

The simple and straightforward calibration of the DSSE-HC model, developed in this thesis, is the key feature to contribute to the industry with limited resources for testing, calibration, and model developments. It is emphasized that the present DSSE-HC model for shell elements contains *only one additional model parameter* for the DSSE, as compared to solid element modeling. It is even more encouraging that no additional experiments are required to determine the parameter. It is readily identified through Eqs 4-13 and 4-14 by knowing the hardening law of a material. Table 7-1 summarizes an experimental program with associated model parameters recommended to calibrate the hardening law and the DSSE-HC model for shell element simulation. Note that Table 7-1 does not include experiments required to identify the parameters of a yield function because a different yield function for a different type of alloys may require a different set of experiments.

Purpose	Experiment	Associated parameters	Related equations
Hardening law	Uniaxial tension in sheet rolling direction on a dog-bone shaped specimen	A, ε_0, n, k_0, Q, β	Eq. 2-2
	Small notched tension (Fig. 6-3a)	α	
Hosford-Coulomb fracture model	Simple shear (Fig. 6-3b)	a, c	Eq. 2-18
	V-bending (Fig. 6-3c)		
	Mini-punch (Fig. 6-3d)	b	
DSSE	No experiment required	d	Eq. 4-12 Eq. 4-13 Eq. 4-14

Table 7-1. Experimental program to identify the parameters of the mixed Swift-Voce hardening law and the DSSE-HC ductile failure model for shell element simulation. Note that the fixed transformation coefficients of $n_f = 0.1$ and $p = 0.01$ are recommended in Eqs. 2-18 and 4-12, respectively.

The detailed procedure is explained in Chapter 6.2.

In a broader perspective, this thesis presents the advantage of combining a localized necking criterion (accounting for the effect of bending) and a ductile fracture initiation model to predict the onset of ductile failure using shell finite elements. Both localized necking and fracture are predicted by integrating scalar indicators. Therefore, different functional forms of localization and fracture loci can be conveniently used in place of the equation for the HC model if prove to be more accurate, with the proposed approach seen as a general modular framework. The present formulation is the game changer to the existing approaches to necking and ductile fracture. By combining those two separate physical phenomena into a single model, the number of tests required for calibration remains unchanged while improving the accuracy of prediction dramatically, as demonstrated in the two previous chapters of the present thesis.

7.2 Outlook

7.2.1 Experimental investigation on localized necking under stretch bending

It was the incorporation of the effect of bending into the DSSE that enabled a reliable prediction of the onset of ductile failure together with a substantial reduction of the mesh-size sensitivity in experiments where localized necking precedes fracture. Such a retardation or suppression of localized necking under bending dominated loading rests on the early experimental findings of Tharrett and Stoughton (2003). However, they conducted those stretch bending experiments on relatively mild steels in 1980s. Major and minor strains on the specimen surfaces were measured by 0.5 *mm* square grids, and a local radius of curvature at the location of the neck was simply approximated as the radius of a punch. More experimental evidence has yet to be found to support some of their arguments about very small and large punch radii that produced outstanding cases. Stereo DIC can improve the accuracy of measured strain fields. A high speed camera system may allow us to detect the exact instant and location of localized necking. Some novel experimental technique that allows the access of DIC on the inner surface in contact with the punch will be of great help. More experiments need to be performed, especially on advanced high strength steel and other lightweight metallic alloys. A purely numerical study using very fine solid element models may replace physical experiments, with an assumption that a material exactly follows a pre-defined constitutive law.

7.2.2 Non-linear accumulation of necking indicator

Bai and Wierzbicki (2008b) originally employed a *non-linear* accumulation for the necking indicator and successfully reproduced the experimental results of Graf and Hosford (1994). Therefore, the validity of a linear accumulation in Eq. 4-15 needs to be checked further in detail. As alternatives, a path-independent stress-based FLC (Stoughton, 2000) or a polar effective plastic strain-based FLC (Stoughton and Yoon, 2012) may be used.

7.2.3 Effect of dynamic loading

The present shell element failure model is aimed at quasi-static loading with isothermal conditions. However, actual forming operations or car crashes occur under much more severe loading conditions. The strain-rate can achieve the order of 100/s (e.g. Mahadevan et al., 2000; Huh et al., 2005), and a large deformation under high speed loading induces a significant increase in temperature at local material points by plastic work, which in turn leads to softening. Therefore, the effect of strain-rate and temperature should be further investigated to improve the accuracy of the DSSE-HC model. Here is presented one feasible solution. Roth and Mohr (2014) proposed the extended HC fracture initiation model for dynamic loading at ambient temperature along with a Johnson and Cook (1983) type of hardening

$$k[\bar{\varepsilon}_p, \dot{\bar{\varepsilon}}_p, T] = k_\varepsilon[\bar{\varepsilon}_p] \cdot k_{\dot{\varepsilon}}[\dot{\bar{\varepsilon}}_p] \cdot k_T[T] \tag{7-1}$$

with strain hardening k_ε (Eq. 2-2), strain-rate hardening $k_{\dot{\varepsilon}}$, and temperature softening function k_T.

$$k_{\dot{\varepsilon}}[\dot{\bar{\varepsilon}}_p] = 1 + C \ln\left[\frac{\dot{\bar{\varepsilon}}_p}{\dot{\varepsilon}_0}\right] \tag{7-2}$$

$$k_T[T] = 1 - \left(\frac{T - T_r}{T_m - T_r}\right)^m \tag{7-3}$$

Temperature was considered as an internal variable whose evolution is governed by

$$\rho C_p dT = \omega[\dot{\bar{\varepsilon}}_p] \eta_k \bar{\sigma}\, d\bar{\varepsilon}_p \tag{7-4}$$

Detailed explanations about the above equations and coefficients are referred to Roth and Mohr (2014). The limit strain under plane strain condition $\bar{\varepsilon}_{DSSE}^{PST}$ at different strain rates may be obtained by applying Eq. 7-1 to the Considère criterion (Eq. 4-13). Therein, the term $dk / d\bar{\varepsilon}_p$ may be calculated as follows.

$$\frac{dk}{d\bar{\varepsilon}_p} = \frac{\partial k_\varepsilon}{\partial \bar{\varepsilon}_p} \cdot k_{\dot{\varepsilon}} \cdot k_T + k_\varepsilon \cdot \frac{\partial k_{\dot{\varepsilon}}}{\partial \dot{\bar{\varepsilon}}_p} \cdot \frac{d\dot{\bar{\varepsilon}}_p}{d\bar{\varepsilon}_p} k_T + k_\varepsilon \cdot k_{\dot{\varepsilon}} \cdot \frac{\partial k_T}{\partial T} \frac{dT}{d\bar{\varepsilon}_p} \tag{7-5}$$

By removing the second term due to the fact that $\bar{\varepsilon}_p$ and $\dot{\bar{\varepsilon}}_p$ are independent, the final expression is obtained as

$$\frac{dk}{d\bar{\varepsilon}_p} = \frac{dk_\varepsilon}{d\bar{\varepsilon}_p} \cdot k_{\dot{\varepsilon}} \cdot k_T + k_\varepsilon \cdot k_{\dot{\varepsilon}} \cdot \frac{dk_T}{dT} \frac{\omega \eta_k \bar{\sigma}}{\rho C_p} \tag{7-5}$$

Substituting Eq. 7-5 to Eq. 4-13 yields

$$k = \frac{2}{\sqrt{3}} \left[\frac{dk_\varepsilon}{d\bar{\varepsilon}_p} \cdot k_{\dot{\varepsilon}} \cdot k_T + k_\varepsilon \cdot k_{\dot{\varepsilon}} \cdot \frac{dk_T}{dT} \frac{\omega \cdot \eta_k \cdot \bar{\sigma}}{\rho C_p} \right]. \tag{7-6}$$

The resulting values of $\bar{\varepsilon}_{DSSE}^{PST}$ at different strain rates may be used to solve Eq. 4-14 along with the fracture parameter b for a specific strain rate to identify the corresponding DSSE parameter d.

7.2.4 More aspects

The effect of anisotropy (yield function) can be further investigated. The effect of complex loading conditions such as loading reversal from compression to tension or orthogonal loading can also be studied.

Lastly but not least, it is important to maintain a proper geometrical discretization (high quality mesh) of the domain for finite element analysis (e.g. Wierzbicki et al., 1988). A region with coarse shell elements may require finer meshes as it deforms. This is beyond the scope of a material model, but it is a very crucial and essential condition for reliable finite element simulations.

Appendix A

Publications & presentations

A.1 Journal publications

[1] K.Pack, M.Luo, and T.Wierzbicki. Sandia Fracture Challenge: blind prediction and full calibration to enhance fracture predictability", International Journal of Fracture 186 (1-2): 155- 175, 2014.

[2] K.Pack and C.C.Roth. The second Sandia Fracture Challenge: blind prediction of dynamic shear localization and full characterization, International Journal of Fracture 198 (1-2): 197-220, 2016.

[3] K.Pack and S.J.Marcadet. Numerical failure analysis of three-point bending on martensitic hat assembly using advanced plasticity and fracture models for complex loading, International Journal of Solids and Structures 85: 144-159, 2016.

[4] K.Pack and D.Mohr. Domain of Shell-to-Solid Equivalence to predict ductile failure with shell finite elements, Engineering Fracture Mechanics, *under review*.

[5] K.Pack, T.Tancogne-Dejean, M. Gorji, and D.Mohr. Hosford-Coulomb ductile failure model for shell elements: experimental identification and validation for DP980 steel and aluminum 6016-T4, *submitted* to International Journal of Solids and Structures.

A.2 Conference presentations

[1] K.Pack, M.Luo, and T.Wierzbicki, Sandia fracture challenge, ASME 2012 International Mechanical Engineering Congress & Exposition, Houston, USA, 2012.

[2] S.Marcadet, K.Wang, C.Roth, K.Pack, M.Luo, T.Wierzbicki, and D.Mohr, Recent advances on predicting ductile fracture of AHSS in automotive applications, Great Designs in Steel, Livonia, USA, 2014.

[3] K.Pack, C.C. Roth, and T. Wierzbicki, Blind prediction of dynamic ductile tearing based on a limited number of material properties, ASME 2015 International Mechanical Engineering Congress & Exposition, Houston, USA, 2015.

[4] C.C.Roth, B. Erice, K.Pack, and D. Mohr, Effect of strain rate, temperature, and stress state on ductile fracture initiation: experiments and localization analysis, International Symposium on Plasticity, Kailua-Kona, USA, 2016.

[5] K.Pack and D. Mohr, Domain of Shell-Solid Equivalence to predict ductile fracture with shell elements, International Symposium on Plasticity, Kailua-Kona, USA, 2016.

[6] K.Pack and D. Mohr, A new approach towards prediction of ductile fracture initiation for shell finite elements and its validation against experiments, International Symposium on Plasticity, Puerto Vallarta, Mexico, 2017.

Bibliography

Abaqus, 2016. Reference Manuals.

Anand, L., Aslan, O., Chester, S.A., 2012. A large-deformation gradient theory for elastic–plastic materials: Strain softening and regularization of shear bands. Int. J. Plast. 30–31, 116–143.

Andrade, F.X.C., Feucht, M., Haufe, A., Neukamm, F., 2016. An incremental stress state dependent damage model for ductile failure prediction. Int. J. Fract. 200, 127–150.

Bai, Y., Wierzbicki, T., 2010. Application of extended Mohr-Coulomb criterion to ductile fracture. Int. J. Fract. 161, 1–20.

Bai, Y., Wierzbicki, T., 2008a. A new model of metal plasticity and fracture with pressure and Lode dependence. Int. J. Plast. 24, 1071–1096.

Bai, Y., Wierzbicki, T., 2008b. Forming severity concept for predicting sheet necking under complex loading histories. Int. J. Mech. Sci. 50, 1012–1022.

Bao, Y., Wierzbicki, T., 2004a. On fracture locus in the equivalent strain and stress triaxiality space. Int. J. Mech. Sci. 46, 81–98.

Bao, Y., Wierzbicki, T., 2004b. A Comparative Study on Various Ductile Crack Formation Criteria. J. Eng. Mater. Technol. 126, 314.

Barlat, F., Brem, J.C., Yoon, J.W., Chung, K., Dick, R.E., Lege, D.J., Pourboghrat, F., Choi, S.H., Chu, E., 2003. Plane stress yield function for aluminum alloy sheets—part 1: theory. Int. J. Plast. 19, 1297–1319.

Bathe, K.-J., 2006. Finite element procedures. Bathe, Klaus-Jurgen.

Beese, A.M., Luo, M., Li, Y., Bai, Y., Wierzbicki, T., 2010. Partially coupled anisotropic fracture model for aluminum sheets. Eng. Fract. Mech. 77, 1128–1152.

Benzerga, A.A., Besson, J., 2001. Plastic potentials for anisotropic porous solids. Eur. J. Mech. A/Solids 20, 397–434.

Benzerga, A.A., Besson, J., Pineau, A., 2004. Anisotropic ductile fracture: Part II: Theory. Acta Mater. 52, 4639–4650.

Benzerga, A.A., Leblond, J.B., Needleman, A., Tvergaard, V., 2016. Ductile failure modeling. Int. J. Fract. 201, 29–80.

Boyce, B.L., Kramer, S.L.B., Bosiljevac, T.R., Corona, E., Moore, J.A., Elkhodary, K., Simha, C.H.M., Williams, B.W., Cerrone, A.R., Nonn, A., Hochhalter, J.D., Bomarito, G.F., Warner, J.E., Carter, B.J., Warner, D.H., Ingraffea, A.R., Zhang, T., Fang, X., Lua, J., Chiaruttini, V.,

Mazière, M., Feld-Payet, S., Yastrebov, V.A., Besson, J., Chaboche, J.L., Lian, J., Di, Y., Wu, B., Novokshanov, D., Vajragupta, N., Kucharczyk, P., Brinnel, V., Döbereiner, B., Münstermann, S., Neilsen, M.K., Dion, K., Karlson, K.N., Foulk, J.W., Brown, A.A., Veilleux, M.G., Bignell, J.L., Sanborn, S.E., Jones, C.A., Mattie, P.D., Pack, K., Wierzbicki, T., Chi, S.W., Lin, S.P., Mahdavi, A., Predan, J., Zadravec, J., Gross, A.J., Ravi-Chandar, K., Xue, L., 2016. The second Sandia Fracture Challenge: predictions of ductile failure under quasi-static and moderate-rate dynamic loading. Int. J. Fract. 198, 5–100.

Brozzo, P., Deluca, B., Rendina, R., 1972. No Title, in: A New Method for the Prediction of Formability in Metal Sheet, Sheet Metal Forming and Formability. Proceedings of the 7th Biennual Conference of the IDDRG.

Chaboche, J.L., 1988a. Continuum Damage Mechanics: Part I—General Concepts. J. Appl. Mech. 55, 59.

Chaboche, J.L., 1988b. Continuum Damage Mechanics: Part II—Damage Growth, Crack Initiation, and Crack Growth. J. Appl. Mech.

Chow, C.L., Wang, J., 1987. An anisotropic theory of continuum damage mechanics for ductile fracture. Eng. Fract. Mech. 27, 547–558.

Chu, C.C., Needleman, A., 1980. Void nucleation effects in biaxially stretched sheets. J. Eng. Mater. Technol. 102, 249.

Clift, S.E., Hartley, P., Sturgess, C.E.N., Rowe, G.W., 1990. Fracture prediction in plastic deformation processes. Int. J. Mech. Sci. 32, 1–17.

Cockcroft, M.G., Latham, D.J., 1968. Ductility and the workability of Metals. J. Inst. Met. 96, 33–39.

Cvitanić, V., Vlak, F., Lozina, Ž., 2008. A finite element formulation based on non-associated plasticity for sheet metal forming. Int. J. Plast. 24, 646–687.

Dunand, M., Maertens, A.P., Luo, M., Mohr, D., 2012. Experiments and modeling of anisotropic aluminum extrusions under multi-axial loading - Part I: Plasticity. Int. J. Plast. 36, 34–49.

Dunand, M., Mohr, D., 2010. Hybrid experimental-numerical analysis of basic ductile fracture experiments for sheet metals. Int. J. Solids Struct. 47, 1130–1143.

Gologanu, M., Leblond, J.B., Devaux, J., 1993. Approximate models for ductile metals containing non-spherical voids-Case of axisymmetric prolate ellipsoidal cavities. J. Mech. Phys. Solids 41, 1723–1754.

Goodwin, G.M., 1968. Application of Strain Analysis to Sheet Metal Forming Problems in the Press Shop. Soc. Automot. Eng. 380–387.

Gorji, M., Berisha, B., Hora, P., Barlat, F., 2016a. Modeling of localization and fracture phenomena in strain and stress space for sheet metal forming. Int. J. Mater. Form. 9, 573–584.

Gorji, M., Berisha, B., Manopulo, N., Hora, P., 2016b. Effect of through thickness strain distribution on shear fracture hazard and its mitigation by using multilayer aluminum sheets. J. Mater. Process. Technol. 232, 19–33.

Graf, A., Hosford, W., 1994. The influence of strain-path changes on forming limit diagrams of Al 6111 T4. Int. J. Mech. Sci. 36, 897–910.

Gurson, A.L., 1977. Continuum Theory of Ductile Rupture by Void Nucleation and Growth: Part I—Yield Criteria and Flow Rules for Porous Ductile Media. J. Eng. Mater. Technol. 99, 2.

Hill, R., 1952. On discontinuous plastic states, with special reference to localized necking in thin sheets. J. Mech. Phys. Solids 1, 19–30.

Hosford, W.F., 2010. Solid mechanics. Cambridge University Press.

Hosford, W.F., 1972. A Generalized Isotropic Yield Criterion. J. Appl. Mech.

Huh, H., Song, J.H., Kim, K.P., Kim, H.S., 2005. Crashworthiness assessment of auto-body members considering the fabrication histories, in: AIP Conference Proceedings. pp. 167–172.

Hutchinson, J.W., Neale, K.W., 1978. Sheet Necking-II. Time-Independent Behavior. Mech. Sheet Met. Form.

Johnson, G.R., Cook, W.H., 1983. A constitutive model and data for metals subjected to large strains, high strain rates and high temperatures. 7th Int. Symp. Ballist.

Keeler, S., Backhofen, W., 1964. Plastic instability and fracture in sheet stretched over rigid punches. ASM Trans. Q. 56, 25–48.

Koistinen, D., 2012. Mechanics of Sheet Metal Forming: Material Behavior and Deformation Analysis. Springer Science & Business Media.

Kõrgesaar, M., Remes, H., Romanoff, J., 2014. Size dependent response of large shell elements under in-plane tensile loading. Int. J. Solids Struct. 51, 3752–3761.

Kõrgesaar, M., Romanoff, J., 2013. Influence of softening on fracture propagation in large-scale shell structures. Int. J. Solids Struct. 50, 3911–3921.

Le Roy, G., Embury, J.D., Edwards, G., Ashby, M.F., 1981. A model of ductile fracture based on the nucleation and growth of voids. Acta Metall. 29, 1509–1522.

LEBLOND, J.-B., PERRIN, G., DEVAUX, J., 1995. An improved Gurson-type model for hardenable ductile metals. Eur. J. Mech. A. Solids 14, 499–527.

Lee, Y.-W., 2005. Fracture prediction in metal sheets. Massachusetts Institute of Technology.

Lemaitre, J., 1985. A Continuous Damage Mechanics Model for Ductile Fracture. J. Eng. Mater. Technol.(Trans. ASME) 107, 83–89.

Li, Y., Luo, M., Gerlach, J., Wierzbicki, T., 2010. Prediction of shear-induced fracture in sheet metal forming. J. Mater. Process. Technol. 210, 1858–1869.

Lou, Y., Huh, H., Lim, S., Pack, K., 2012. New ductile fracture criterion for prediction of fracture forming limit diagrams of sheet metals. Int. J. Solids Struct. 49, 3605–3615.

Luo, M., Dunand, M., Mohr, D., 2012. Experiments and modeling of anisotropic aluminum extrusions under multi-axial loading - Part II: Ductile fracture. Int. J. Plast. 32–33, 36–58.

Luo, M., Wierzbicki, T., 2010. Numerical failure analysis of a stretch bending test on dual-phase steel sheets using a phenomenological fracture model. Int. J. Solids Struct. 47, 3084–3102.

Mahadevan, K., Liang, P., Fekete, J., 2000. Effect of Strain Rate in Full Vehicle Frontal Crash Analysis, in: SAE Technical Paper.

Marcadet, S.J., Mohr, D., 2015. Effect of compression-tension loading reversal on the strain to fracture of dual phase steel sheets. Int. J. Plast. 72, 21–43.

Marciniak, Z., Kuczyński, K., 1967. Limit strains in the processes of stretch-forming sheet metal. Int. J. Mech. Sci. 9, 609–620.

McClintock, F.A., 1968. A criterion for ductile fracture by the growth of holes. J. Appl. Mech. 35, 363–371.

Mindlin, R.D., 1951. Influence of Rotatory Inertia and Shear on Flexural Motions of Isotropic, Elastic Plates. J. Appl. Mech. Asme 18, 31–38.

Mohr, D., Dunand, M., Kim, K.H., 2010. Evaluation of associated and non-associated quadratic plasticity models for advanced high strength steel sheets under multi-axial loading. Int. J. Plast. 26, 939–956.

Mohr, D., Marcadet, S.J., 2015. Micromechanically-motivated phenomenological Hosford-Coulomb model for predicting ductile fracture initiation at low stress triaxialities. Int. J. Solids Struct. 67–68, 40–55.

Nahshon, K., Hutchinson, J.W., 2008. Modification of the Gurson Model for shear failure. Eur. J. Mech. A/Solids 27, 1–17.

Pack, K., Ahn, K., Huh, H., Lou, Y., 2012. Fracture modeling of DP780 sheets using a hybrid experimental – numerical method and two dimensional digital image correlation. Int. J. Mater. Prod. Technol. 15, 34–46.

Pack, K., Marcadet, S.J., 2015. Numerical failure analysis of three-point bending on martensitic hat assembly using advanced plasticity and fracture models for complex loading. Int. J. Solids Struct.

Pack, K., Roth, C.C., 2016. The second Sandia Fracture Challenge: blind prediction of dynamic shear localization and full fracture characterization. Int. J. Fract. 198, 197–220.

Pardoen, T., Hutchinson, J.W., 2000. Extended model for void growth and coalescence. J. Mech. Phys. Solids 48, 2467–2512.

Pearce, R., 1991. Sheet Metal Forming. Springer Science & Business Media.

Reissner, E., 1945. The Effect of Transverse Shear Deformation on the Bending of Elastic Plates. J. Appl. Mech. 12, 69–77.

Rice, J.R., Tracey, D.M., 1969. On the ductile enlargement of voids in triaxial stress fields. J. Mech. Phys. Solids 17, 201–217.

Roth, C.C., Mohr, D., 2016. Ductile fracture experiments with locally proportional loading histories. Int. J. Plast. 79, 328–354.

Roth, C.C., Mohr, D., 2014. Effect of strain rate on ductile fracture initiation in advanced high strength steel sheets: Experiments and modeling. Int. J. Plast. 56, 19–44.

Schaeffler, D., 2016. Getting to know more about the metal you are forming [WWW Document]. URL http://www.thefabricator.com/article/metalsmaterials/getting-to-know-more-about-the-metal-you-are-forming

Stoughton, T.B., 2002. A non-associated flow rule for sheet metal forming, in: International Journal of Plasticity. pp. 687–714.

Stoughton, T.B., 2000. General forming limit criterion for sheet metal forming. Int. J. Mech. Sci. 42, 1–17.

Stoughton, T.B., Yoon, J.W., 2012. Path independent forming limits in strain and stress spaces, in: International Journal of Solids and Structures. pp. 3616–3625.

Stoughton, T.B., Yoon, J.W., 2011. A new approach for failure criterion for sheet metals. Int. J. Plast. 27, 440–459.

Stoughton, T.B., Zhu, X., 2004. Review of theoretical models of the strain-based FLD and their relevance to the stress-based FLD. Int. J. Plast. 20, 1463–1486.

Sung, J.-H., 2010. The Causes of "Shear Fracture" of Dual-Phase Steels.

Sutton, M.A., Orteu, J.J., Schreier, H.W., 2009. Image Correlation for Shape, Motion and Deformation Measurements- Basic Concepts, Theory and Applications. Image Rochester NY 341.

Swift, H.W., 1952. Plastic instability under plane stress. J. Mech. Phys. Solids 1, 1–18.

Tancogne-Dejean, T., Roth, C.C., Woy, U., Mohr, D., 2016. Probabilistic fracture of Ti-6Al-4V made through additive layer manufacturing. Int. J. Plast. 78, 145–172.

Tharrett, M.R., Stoughton, T.B., 2003. Stretch-Bend Forming Limits of 1008 AK Steel. Soc. Automot. Eng. 123–129.

Tvergaard, V., Needleman, A., 1984. Analysis of the cup-cone fracture in a round tensile bar. Acta Metall. 32, 157–169.

Voce, E., 1948. The relationship between stress and strain for homogeneous deformations. J. Inst. Met. 74, 537–562.

Walters, C.L., 2014. Framework for adjusting for both stress triaxiality and mesh size effect for failure of metals in shell structures. Int. J. Crashworthiness 19, 1–12.

Wierzbicki, T., Abramowicz, W., Stolarski, H., 1988. On global locking in crushed shells. Comput. Mech. 88, 151–156.

Xue, L., 2008. Constitutive modeling of void shearing effect in ductile fracture of porous materials. Eng. Fract. Mech. 75, 3343–3366.

Xue, L., 2007. Damage accumulation and fracture initiation in uncracked ductile solids subject to triaxial loading. Int. J. Solids Struct. 44, 5163–5181.